2016

NONLINEAR INVERSION STRATEGIES APPLIED TO SOURCE CHARACTERIZATION AND 3D EARTHQUAKE TOMOGRAPHY IN VOLCANIC ENVIRONMENTS: A CASE STUDY AT PACAYA VOLCANO, GUATEMALA

Federica Lanza
Michigan Technological University, flanza@mtu.edu

NONLINEAR INVERSION STRATEGIES APPLIED TO SOURCE CHARACTERIZATION AND 3D EARTHQUAKE TOMOGRAPHY IN VOLCANIC ENVIRONMENTS: A CASE STUDY AT PACAYA VOLCANO, GUATEMALA

By

Federica Lanza

A DISSERTATION

Submitted in partial fulfillment of the requirements for the degree of

DOCTOR OF PHILOSOPHY

In Geophysics

MICHIGAN TECHNOLOGICAL UNIVERSITY

2016

This dissertation has been approved in partial fulfillment of the requirements for the Degree of DOCTOR OF PHILOSOPHY in Geophysics.

Department of Geological and Mining Engineering and Sciences

Dissertation Advisor:	*Gregory P. Waite*
Committee Member:	*Wayne D. Pennington*
Committee Member:	*Simon Carn*
Committee Member:	*Diana C. Roman*
Department Chair:	*John S. Gierke*

Table of Contents

Preface

Portions of this document contain material that has already been published and material currently under review for publication.

Chapter 1 entitled, “Near-surface velocity structure of Pacaya volcano, Guatemala, derived from small-aperture array analysis of seismic tremor”, has been published in the Bulletin of Seismological Society of America, with the following citation: “Lanza, F., L.M. Kenyon, and G.P. Waite (2016). Near-surface velocity structure of Pacaya volcano, Guatemala, derived from small-aperture array analysis of seismic tremor, *Bull. Seism. Soc. Am.,* **106** (4), doi: 10.1785/0120150275”. This work was compiled with suggestions from the coauthors listed above, assistance from reviewers, and the editorial staff of the journal. Coauthor Lindsay M. Kenyon assisted with portions of the analysis of the data and coauthor Gregory P. Waite reviewed figures, text, and analysis methods. I processed the data, which were previously collected by coauthor Gregory P. Waite and compiled the manuscript.

Chapter 2 and Chapter 3 entitled “A nonlinear approach to moment tensor sensitivity in volcanic settings” and “Nonlinear moment tensor inversion at Pacaya volcano, Guatemala: a data application” respectively, have been submitted for publication to the Geophysical Journal International. As of this writing, both have been re-submitted for the second round of reviews. Coauthor Gregory P. Waite assisted in the data processing and reviewed data analysis methods, figures, and text for these manuscripts. I planned the field campaign, collected data, processed the data, and compiled the submitted manuscript.

Chapter 4 entitled “Nonlinear inversion for 3D local earthquake tomography at Pacaya volcano, Guatemala” is in preparation to be submitted to the Journal of Volcanology and Geothermal Research. Coauthor Gregory P. Waite assisted in the planning and collection of the data, reviewed data analysis methods, figures, and text for this manuscript. I planned the field campaign, collected data, processed the data, and compiled the manuscript.

Acknowledgments

Many people made this work possible and I am extremely grateful to all of you. I was fully supported financially through the National Science Foundation Award No. 1053794 and I received instrument support from IRIS PASSCAL Instrument Center.

The GMES department at Michigan Tech has been an outstanding place to work and study. Dr. Greg Waite has taught me much about geophysics, seismology and computer programming and I am deeply grateful to have had the opportunity to have him as my teacher and advisor. Greg has had an extraordinary patience, often taking hours of his time to sit with me to debug codes or listen and answer to my many questions. Greg has been incredible to work with in the field, and his personal and professional guidance throughout my graduate career helped me to be a better person, a better scientist. Dr. Wayne Pennington, Dr. Diana Roman and Dr. Simon Carn have also been supportive committee members and I thank them for serving as mentors and role models.

My Michigan family and friends have been extremely supportive and patient with me and I thank you all for your kindness, support and, most of all, profound friendship. Thanks to Dr. Bill Rose and his wife Nano for introducing me to this wonderful and unique place that is the Keweenaw peninsula, and for sharing the beauty of Silver Island, which I will miss dearly.

This work could not have been completed without the support of my Italian family, thanks for always being there for me, even if from thousands miles away.

Abstract

Full-waveform moment tensor inversion of volcanic seismic signals and travel-time 3D tomography of local earthquakes have been widely used to explore source processes related to magma transport as well as to image the location and size of magma storage systems. However, the inversion solutions and the associated reliability estimates are non-unique and bear intrinsic uncertainties due to simplifying assumptions about the source, inaccuracies in the velocity models, dependence on network configuration, and other a priori constraints imposed by the modeler.

This work addresses the non-uniqueness and uncertainties of the model results by introducing non-linear inversion techniques that allow sampling the model space more effectively. We developed a nonlinear inversion approach for source type that uses a grid search over all possible moment tensor types and orientations to obtain a quantitative measure of the source mechanism reliability. For the tomography inverse problem, the solution space is fully explored using a 'guided' Monte-Carlo method in which starting velocity models are randomly selected and, through simulating annealing, only a subset of models that satisfies acceptability criteria is retained. Extensive synthetic tests are employed to test and validate the nonlinear inversion methods. The inversion procedures are then put into practice at Pacaya volcano, Guatemala. First, nonlinear moment tensor inversion is applied to explosion-related, long-period events that were recorded during a temporary installation of four broadband seismic stations in October-November 2013. The derived source reflects a shallow crack-like mechanism that is likely related to bubble-bursting events at the summit. Secondly, nonlinear travel-time local 3D tomography is employed to invert hundreds of local events that were detected during another temporary seismic network installation in January 2015. Re-location of the events using a 3D velocity model reveals the presence of a straight conduit possibly connecting a shallow magma reservoir to the surface.

The inversion approaches proposed in this study allow a comprehensive assessment of the model solution space. This is revealed to be of crucial aid in the

determination of the confidence level of model interpretations, especially in cases like Pacaya, where availability of resources and observational data is limited.

Introduction

The physical processes behind volcanic eruptions involve a complex interaction of liquid, gas, and solid along magma pathways. Pressure oscillations and movement of fluids through conduits, such as the ascent of gas slugs, as well as brittle failure mechanisms, reflecting the response of the rock to stress changes induced by magma movement, can produce seismic signals (e.g., Chouet, 1996). Source modeling of seismic events beneath volcanoes has therefore the potential to provide models that correspond to fluid pathways, processes, and geometries, leading to a better understanding of the underlying causes connected to eruption activity. Great promise for modeling conduit dynamics is the analysis of low-frequency events, which include tremor, long-period (LP) and very-long-period (VLP) signals. Full-waveform moment tensor inversion of these signals has been used successfully to derive source mechanisms of both LP and VLP signals at a number of active volcanoes around the world (see Chouet and Matoza, 2013 for a review).

To obtain a more comprehensive picture of the magmatic plumbing systems, source mechanism studies can be complemented with high-resolution 3D tomographic models based on iterative inversions of seismic travel-time data (P-wave, S-wave or V_P/V_S ratios). Provided high quality, well-distributed local earthquake data, volcano tomographic inversion can produce three-dimensional images of the structure beneath the volcanic edifice, i.e. the shape of geometry of magma accumulations (Lees, 2007). Tomographic analysis usually begins by locating earthquakes with one-dimensional model, then a 3D velocity model that explains the travel-time data better than the one-dimensional velocity model is sought. Local earthquake tomography (or LET) has been applied widely and many different approaches have been developed to simultaneously solve for velocity structure and earthquake hypocenter location (Kissling, 1988; Thurber, 1993; Rawlinson *et al.,* 2010). Examples of tomography on magmatic systems include Mount St Helens, Washington (Waite and Moran, 2009; Kiser *et al.,* 2016), Mammoth Mountain, California (Dawson *et al.,* 2016), and Yellowstone (Waite *et al.,* 2006) to name a few.

However, both full-waveform moment tensor inversions and the inverse problem of 3D local earthquake tomography are non-unique and bear intrinsic uncertainties. In moment tensor inversions, as shown by other studies, uncertainties on the estimates of the source mechanisms can be introduced by near-surface low-velocity structure and topography, especially for LP signals, which are characterized by shorter wavelengths (Chouet, 1996; Bean *et al.,* 2008). An accurate interpretation of seismic sources also depends on the capability of seismic networks to resolve source mechanisms and locations (Dawson *et al.,* 2011). The effect of volcano seismic network configurations on source time function solutions has not been thoroughly investigated to date, but is especially important in volcanic environments where accessibility and equipment are often limited. As for LET inversions, these are inherently nonlinear as the earthquake locations depend on the velocities that are being sought. Generally, solutions are achieved by iterations of linearized steps. Therefore, the linearized inversion results and the reliability of the estimates of the model parameters (hypocenters and structure), highly depend on the initial reference velocity (Kissling *et al.,* 1994) and other important a priori constraints (i.e. damping values), often selected empirically.

Due to these simplifying assumptions and the non-linearity of the problems, there is a necessity to explore the solution space more systematically, and to better quantify the uncertainties related to the inversion solutions. This body of work focuses on the implementation of nonlinear inversion strategies to full-waveform moment tensor inversion and 3D travel-time seismic tomography in order to improve the quantification of the uncertainty related to model solutions. A better understanding of both near-surface velocity structure and mechanisms responsible for low-frequency seismicity at volcanoes is indeed achieved by increasing the confidence level in the accuracy of our geophysical models.

These newly developed nonlinear inversion techniques are tested with synthetic modeling to evaluate, in first place, the effectiveness of the methodology. The nonlinear inversion for source type and travel-time tomography are then applied to real data recorded at Pacaya volcano, in Guatemala, where temporary seismic

networks were deployed almost yearly since 2011 with the objective to monitor its seismic activity. Pacaya volcano is a basaltic stratovolcano located about 30 km SSW of Guatemala City, in the Central American Volcanic Arc. The current eruptive phase began in 1961, and both effusive and explosive eruptions have built a young cone on the west side of the older volcanic complex and over an ancestral collapse scarp on the western flanks (Rose *et al*., 2013). Over the last four years, Pacaya has experienced increased volcanic activity, including energetic strombolian eruptions, lava flows and continuous passive degassing. Pacaya shares characteristics common to many active volcanoes, such as steep topography, strombolian-style eruptions, and repetitive LP seismicity; hence the results presented in this work should be widely transferrable.

The first chapter presents results from a small-aperture array study of seismic tremor from Pacaya volcano. Previous studies have demonstrated that the near-surface heterogeneous layering and compositional variety characteristic of young volcanic cones strongly affects phase velocities. An unknown velocity model is often cited as a major source of error in computing source mechanisms for shallow volcanic events, as well as a potential source of spurious results. The goal of this study is to generate a shallow velocity model for Pacaya volcano by inverting dispersion curves calculated using the well-established spatial autocorrelation method (SPAC) of Aki (1959). The result of the inversions is a shear-wave velocity model for the upper 500 m that contains multiple thin, low velocities layers in the upper 200 m of the volcano.

The second chapter provides a comprehensive assessment of volcanic network configurations to optimize the resolution of moment tensor inversion and introduces a nonlinear inversion approach for source type. Synthetic tests on 16 different network configurations are performed to investigate the effects of seismic network configurations on the recovering source mechanisms by waveform inversion. The source time function resolution and uncertainty are quantitatively measured using the nonlinear inversion approach. In doing so, we calculate the misfits between the source time functions obtained from the inversion of each subnet configuration at a fixed location and the possible moment tensors in a discretized lune space as defined by

Tape and Tape (2012). We find that complete azimuthal coverage, with stations located at different distance ranges from the source allows for a higher resolution recovery of the source time function. In general, a similar degree of uncertainties characterizes configurations with as many as 40 stations and as low as 8 stations. The level of accuracy of configurations with less than 8 stations is dependent on the source input model with more acceptable performances for volumetric sources.

The third chapter presents a data application of the nonlinear moment tensor inversion described in Chapter 2 for LP volcanic sources at Pacaya volcano, where weak volcanic seismic signals accompanied by similar infrasound signals were recorded in the fall of 2013. The study employs the near-surface structure obtained in Chapter 1 for the full waveform moment tensor inversion of the recorded LP events. With a network of only 4 stations, quantitative description of moment tensor uncertainty is necessary before any interpretation can be attempted. Results show that LP events reflect a shallow crack-like mechanism most likely related to bubble-bursting events at the summit. A certain degree of ambiguity in the source location cannot be ignored due to uncertainties in the velocity model and the small number of stations employed in the inversion. Despite this, the moment tensor solution clearly demonstrates that the LP events involve volume change in the source process.

The fourth chapter focuses on the reconstruction of a 3D tomographic model using the dataset that was acquired from the most recent (January 2015) network installation at Pacaya, consisting of 19 three-component, short-period sensors. This constitutes the first attempt of producing a more complete image of the velocity structure of the volcano. In order to increase the sampling of the model space, this study employs a nonlinear inversion technique based on a ‘guided’ Monte-Carlo method in which starting velocity models are randomly selected and, through simulating annealing, only a subset of models that satisfies acceptability criteria is retained. The method is tested through synthetic checkerboard tests that show a fairy good level of recovery of the synthetic velocity anomalies. Due to the quality and clustered distribution of the dataset recorded at Pacaya, the interpretation of the inversion solutions for both the linearized and the nonlinear case is limited. However,

similar features are recovered across the two models. On the other hand, the 3D velocity model allows for a proper re-location of the events, highlighting the presence of a straight conduit below the summit vent.

Together, these chapters highlight the importance of quantitatively measuring the uncertainty of model solutions for a correct, geologically-sound interpretation of both source mechanisms of low-frequency volcano-seismic signals and seismic velocity models beneath volcanoes. With the development of new nonlinear inversion approaches, I think that positive strides have been taken in this direction. Moreover, this work provides substantial advancement of our scientific knowledge about Pacaya volcano. Insights into the velocity structure and source processes of Pacaya's seismicity are obtained, setting the stage for further seismic studies of the volcano. The methods outlined in this work can be also easily extended to investigations at other volcanoes.

CHAPTER 1

Near-surface velocity structure of Pacaya volcano, Guatemala, derived from small-aperture array analysis of seismic tremor[1]

[1]The material contained in this chapter was previously published in:

Lanza, F., L. M. Kenyon, and G.P. Waite (2016), Near-surface velocity structure of Pacaya volcano, Guatemala, derived from small-aperture array analysis of seismic tremor, *Bull. Seism. Soc. Am.,* **106** (4), doi: 10.1785/0120150275.

THE SEISMOLOGICAL SOCIETY OF AMERICA
400 Evelyn Ave., Suite 201
Albany, CA 94706-1375
(510) 525-5474; FAX (510) 525-7204
www.seismosoc.org

Abstract

Knowledge of the typically complicated near-surface structure on volcanoes is critical for determining accurate seismic-event locations and seismic source mechanisms associated with precursory and eruptive activity. To generate a near-surface velocity model for the active cone of Pacaya volcano, Guatemala, we recorded seismic tremor and ambient noise with a small-aperture array of 11 short-period seismometers in January 2011. The diffuse wavefield was investigated using the spatial autocorrelation (SPAC) method, and we computed Rayleigh and Love dispersion curves at the array location. The phase velocities for Rayleigh waves range from 1000 m/s at 2 Hz to 230 m/s at 10 Hz; those for Love waves range from 600 to 250 m/s over the same frequency band. Such low velocities are consistent with the presence of unconsolidated tephra on the surface of the volcano interspersed with lava flows. Assuming they represent the fundamental modes of Rayleigh and Love waves, we inverted the dispersion curves to produce a shear-wave velocity model of the upper 500 m beneath the array.

1.1. Introduction

An accurate velocity model serves as a baseline for many seismic analyses. By establishing a reliable velocity structure, we increase the level of confidence for any further seismic studies. Active volcanoes are challenging to study seismically, in part due to the complex near-surface velocity structure associated with complexly interbedded lava flows, pyroclastic flows, and airfall deposits. Active source studies have been used in some cases (e.g., Zucca and Evans, 1992; Paulatto *et al.*, 2010; Beachley *et al.*, 2012; Jolly *et al.*, 2012) but are typically not possible because volcanoes are in protected areas or simply too dangerous. Although there are many examples of passive tomography studies of volcanoes (see Lees, 2007, for a review), these typically require large deployments with many stations to obtain a well-distributed dataset. In addition to ballistic seismic studies, ambient noise-based structural studies (e.g., Shapiro *et al.*, 2005) are now routinely conducted on volcanoes (e.g., Brenguier *et al.*, 2007). The commonly employed time-domain noise correlation approach is equivalent to spatial autocorrelation (SPAC), which has been in use for many decades (Tsai and Moschetti, 2010). Ambient noise approaches are especially valuable where traditional methods of earthquake seismology that rely on distinct *P* and *S* arrivals cannot be used (e.g., Goldstein and Archuleta, 1987, 1991a,b; Wagner and Owens, 1996; Xu *et al.*, 1996; Chouet *et al.*, 1998; Bonnefoy-Claudet *et al.*, 2006). In particular, processing of data from small-aperture arrays has been efficiently employed to separate source, path, and site effects in tremor wavefields (Capon, 1969; Ferrazzini *et al.*, 1991; Goldstein and Chouet, 1994; Chouet *et al.*, 1997; Métaxian *et al.*, 1997; Saccorotti, Maresca, et al., 2001; Rost and Thomas, 2002; Okada, 2003; Mora *et al.*, 2006; Chávez-García et al., 2007; Nardone and Maresca, 2011). One approach to separate the wavefield components using small-aperture arrays is the correlation method of Aki (1957, 1959, 1965). Assuming that the wavefield is stationary and stochastic in time and space, the SPAC method of Aki has been used for decades to determine the phase velocities of Rayleigh and Love waves and to quantify their relative contributions to the tremor wavefield. For example, Ferrazzini *et al.* (1991) used this correlation technique to study the average

characteristics of the wavefield generated by tremor and gas-piston events at Puu Oo, Kilauea volcano, Hawaii; Chouet *et al.* (1998) applied Aki's method to analyze tremor at Stromboli volcano, Italy, and to derive a shallow velocity model beneath the arrays; and Mora *et al.* (2006) used the SPAC method to estimate Love and Rayleigh dispersion curves at Arenal volcano, Costa Rica (see also Snieder and Larose, 2013, for a recent review).

In this study, we apply the SPAC method (Aki, 1957, 1959, 1965) to derive the dispersive properties of the surface-wave components in the tremor wavefield at Pacaya volcano, Guatemala. We use data collected during a two-week seismic survey in January 2011 from a dense small-aperture array of short-period seismometers deployed on the west flank of the volcano (Figure 1.1). The dispersion data are then used to model the shallow shear-wave velocity structure beneath the array. We first introduce Pacaya volcano followed by a description of the array design and data recorded. We then review Aki's correlation method and describe and discuss the results from the inversions of the correlation data for the dispersion characteristics of Rayleigh and Love waves and for the S -wave velocity structure beneath the array.

1.2. Pacaya Volcano

Pacaya volcano (14.381° N, 90.601° W) is an active 2552-m-high composite stratovolcano located about 30 km south of Guatemala City, Guatemala. The volcano is part of a volcanic complex on the southern rim of the Pleistocene Amatitlan caldera near the intersection of the Guatemala City graben and the Jalpatagua right-lateral fault zone (Wunderman and Rose, 1984; Bardintzeff and Deniel, 1992; Conway *et al.*, 1992). Along with the active MacKenney cone, Pacaya is a volcanic complex consisting of Old Pacaya, an ancestral andesitic stratovolcano, and a cluster of andesitic– dacitic lava cones (Cerro Chino, Cerro Grande, and Cerro Chiquito), which occupy the southern caldera floor (Bardintzeff and Deniel, 1992; Conway *et al.*, 1992; Schaefer *et al.*, 2013) (Figure 1.1). The basaltic MacKenney cone is composed of interbedded lavas and tephra and has been almost constantly erupting since the

current active phase began in 1961 (Rose *et al.*, 2013). Eruptive activity is characterized by persistent degassing (Andres and Kasgnoc, 1998) and frequent strombolian events from the summit, alternating with lava flows extruding from the flanks of the MacKenney cone (Rodriguez *et al.*, 2004; Dalton *et al.*, 2010; Matias Gomez, 2010).

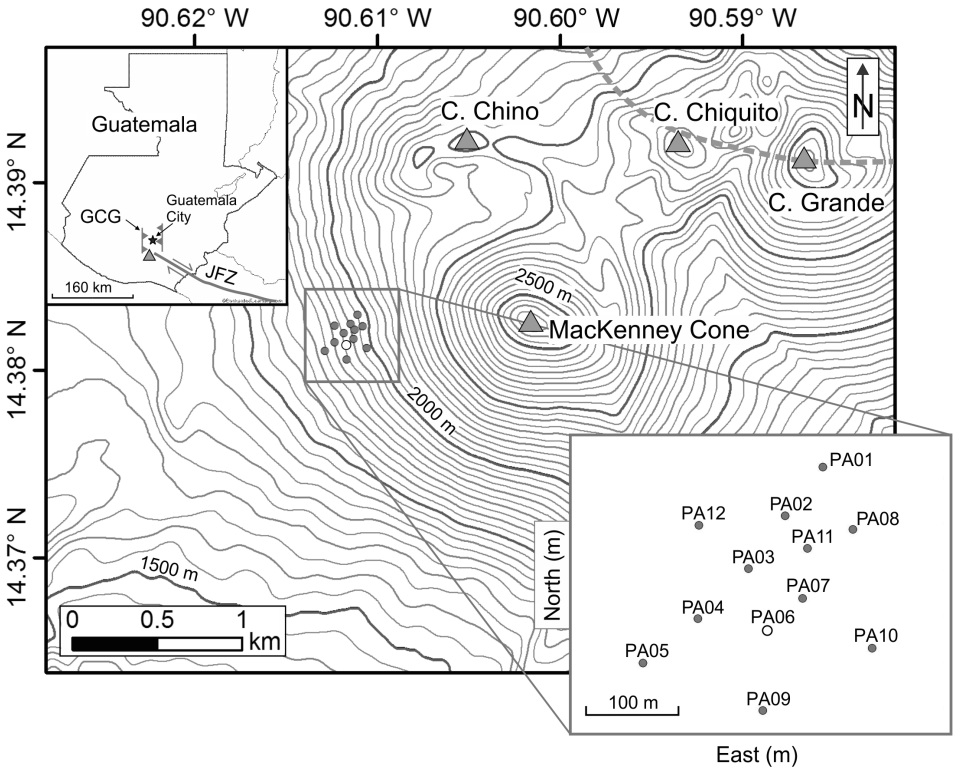

Figure 1.1. The Pacaya complex showing the active MacKenney cone and the ancestral cones as triangles; the array position on the west flank is shown as solid circles. The contour interval is 25 m. The top inset box shows the position of Pacaya in Guatemala and the main structural features near the volcano: the Guatemala City graben (GCG) and the Jalpatagua fault zone (JFZ) (Wunderman and Rose, 1984). The Amatitlan caldera rim is indicated by the dashed line on the main map. The expanded view of the rectangle centered on the array shows the configuration of the semicircular array in detail. The open circle indicates the station that was not used in the frequency–slowness analysis due to a malfunction. Station PA03 was used as the reference station.

Occasionally, larger explosive eruptions have interrupted these smaller events, at times causing partial destruction of the summit cone (Siebert and Simkin, 2002)

and evacuation of the nearby settlements. A moderately large eruption (lower VEI 3) occurred on 27 May 2010. This eruption was explosive and violent in character, with ballistic projectiles up to 50 cm long, and a tephra accumulation over an area greater than 1000 km^2 (Rose *et al.*, 2013). It resulted in significant morphological changes in the MacKenney cone: a new fissure-like structure formed on the north-northwest flank, and a new vent formed on the south-southeast flank that produced a lava flow of ~5 km long (Rose *et al.*, 2013).

In 2011, Pacaya volcano showed typical background activity, mainly consisting of passive degassing. Coincident with the time of operation of the array, on 20 January 2011 Instituto Nacional de Sismologìa, Vulcanologìa, Meterologìa and Hidrologìa reported seismic activity consistent with observations of steam and gas emitted from the base of the northwest flank of Pacaya's MacKenney cone. During 21– 24 January 2011, fumarole activity in the crater continued with variable intensity.

1.3. Instrumentation and Data

During the January 2011 field campaign, a semicircular small-aperture array of 12 short-period seismometers was deployed on the west flank of Pacaya at a distance of ~1.5 km from the summit crater and a mean elevation of 1943 m above sea level (Figure 1.1). We used Mark Products/Sercel three-component L-22 sensors with a natural frequency of 2 Hz and a sensitivity of 88 V/m/s. Data were recorded on 12 Reftek 130 digitizers operating in continuous mode at 125 samples/s and equipped with Global Positioning System (GPS) timing. Station locations were determined independently with real-time differential GPS to an accuracy of 2– 4 m. The array was designed to allow for directional analysis of the recorded wavefield. A fundamental assumption of plane-wave decomposition methods is that the incoming waves across the array are planar. Therefore, the distance between the array and the source should be two or three times the aperture of the array (Almendros *et al.*, 1999). Furthermore, the array must be wide enough to resolve arrival-time differences.

In the case of Pacaya, to safely assume that the ray paths are parallel across

the array and to guarantee a good resolution of the signal azimuths associated with individual wave components, the array was designed to have an aperture of ~200 m with spacing between receivers of ~50 m. We were able to use horizontal- and vertical-component channels from 11 of the 12 short-period stations, because one station did not function properly. The period investigated spans the 16– 28 January 2011 time interval, during which sustained tremor was the most persistent source of seismic activity. Spectrograms obtained for the entire period of the array operation reveal the presence of nearly continuous, narrow frequency bands of energy radiation spanning the 1– 6 Hz frequency range.

For our SPAC analysis, we selected 16 300-s-long segments of tremor recorded on 23 and 24 January 2011. These time windows were carefully chosen based on the lack of the narrowband, sustained energy radiation as well as the lack of earthquake signals. Typical vertical-component seismograms and spectra for the first 30 s of one of the selected records are shown in Figure 1.2 for all the receivers of the array.

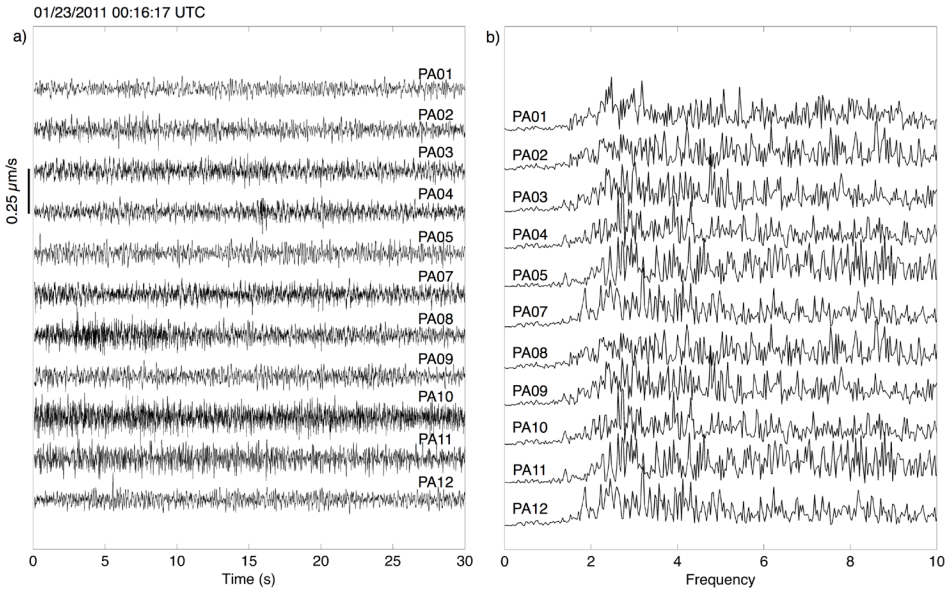

Figure 1.2. (a) Example of 30 s seismograms of tremor recorded on vertical-component receivers of the array for one selected time window. Date and time at the start of the record are shown at the upper left side of the panel. (b) Amplitude spectra of the seismograms shown in (a).

1.4. Correlation Method

The SPAC technique uses cross-correlated ambient noise between station pairs at fixed distances to determine phase velocities. Following the assumption that the wavefield is stochastic and stationary in time and space, Aki (1957) showed that, for vertical components of motion, the azimuthally averaged correlation coefficient is a function of the angular frequency and the station spacing, and it is equal to

$$\overline{\rho_z}(r,\omega_0) = J_0\left[\frac{\omega_0}{c_R(\omega_0)}r\right] \qquad (1.1)$$

in which J0 is the zero-order Bessel function, $c_R(\omega_0)$ is the phase velocity of Rayleigh waves at the frequency ω_0 , and the bar indicates an average over azimuths spanning the 0–2π range. Thus, equation (1) shows that phase velocities can be estimated from measurements of correlation functions for vertical motion from receivers set in a circular pattern located at the same distance *r* from a central reference station. Equation (1), because it is valid for the vertical component of motion, is used to derive Rayleigh-wave phase velocities. A similar procedure is followed for the horizontal components of motion (e.g., Chouet, 1996; Chouet *et al.*, 1998):

$$\bar{\rho}_r^{\parallel}(r,\omega_0) + \bar{\rho}_r^{\perp}(r,\omega_0) = 2\varepsilon\left\{J_0\left[\frac{\omega_0}{c_R(\omega_0)}r\right] - \frac{c_R(\omega_0)}{\omega_0 r}J_1\left[\frac{\omega_0}{c_R(\omega_0)}r\right]\right\}$$

$$+2(1-\varepsilon)\frac{c_L(\omega_0)}{\omega_0 r}J_1\left[\frac{\omega_0}{c_L(\omega_0)}r\right]$$

$$\bar{\rho}_\varphi^{\parallel}(r,\omega_0) + \bar{\rho}_\varphi^{\perp}(r,\omega_0) = 2\varepsilon\frac{c_R(\omega_0)}{\omega_0 r}J_1\left[\frac{\omega_0}{c_R(\omega_0)}r\right]$$

$$+2(1-\varepsilon)\left\{J_0\left[\frac{\omega_0}{c_L(\omega_0)}r\right] - \frac{c_L(\omega_0)}{\omega_0 r}J_1\left[\frac{\omega_0}{c_R(\omega_0)}r\right]\right\} \qquad (1.2)$$

in which J_1 is the first-order Bessel function. The radial (ρ_r) and the azimuthal (ρ_φ) components are here defined as parallel and normal to the radii extending from the central reference station to each individual receiver. The summation implies the presence of mixed-mode vector waves (Rayleigh and Love waves). The phase velocity of Rayleigh waves $c_R(\omega_0)$ is known from independent fits of equation (1.1),

whereas the phase velocity of Love waves $c_L(\omega_0)$, together with the fraction of power carried by both types of waves ε, is determined by fitting equations (1.2) to the azimuthal averages of the correlation coefficients ρ_r and ρ_φ. To determine the phase velocities of the waves constituting the wavefield, we calculated the azimuthal averages of the correlation coefficients of the filtered signal for all pairs of receivers belonging to the same spacing interval and fit these data to the curves defined by equations (1.1) and (1.2).

1.5. Data Analysis

We first estimated the phase velocity of Rayleigh waves using the vertical components. We applied a 0.5-Hz-wide, four-pole, zero-phase, band-pass filter to the vertical component data, normalized it, removed the mean, and cross-correlated it between station pairs. The correlation coefficients obtained for individual station pairs were then averaged for all the station pairs with common spacings (±2 m) over the chosen 16 300-s-long time intervals to derive an estimate of the azimuthally averaged signal correlation as a function of distance and frequency. The correlation and summing procedure was conducted for all frequencies from 0.25 to 10.15 Hz with 0.1 Hz steps. The whole process was then repeated for all the station spacings.

Figure 1.3 shows the azimuthally averaged correlation coefficients calculated with averaged station spacings of 73, 82, 100, 132, 145, 153, and 212 m. We obtained the phase velocities by reading zero crossings, maxima, and minima of the correlation functions obtained for the different distance ranges following Ferrazzini *et al.* (1991) and Chouet *et al.* (1998). The derived measurements were used to find the Rayleigh wave dispersion curve, which is expressed through a simple analytical expression (Chouet *et al.*, 1998):

$$c_R(f) = Af^{-b}e^{-df} \qquad (1.3)$$

in which f is the frequency and A, b, and d are constants. The constants A = 1816, b = 1.43, and d = −0.12 were estimated using a least-squares error grid search.

Figure 1.3h summarizes the phase velocity data for the seven distinct radii and shows the best-fitting phase velocity curve.

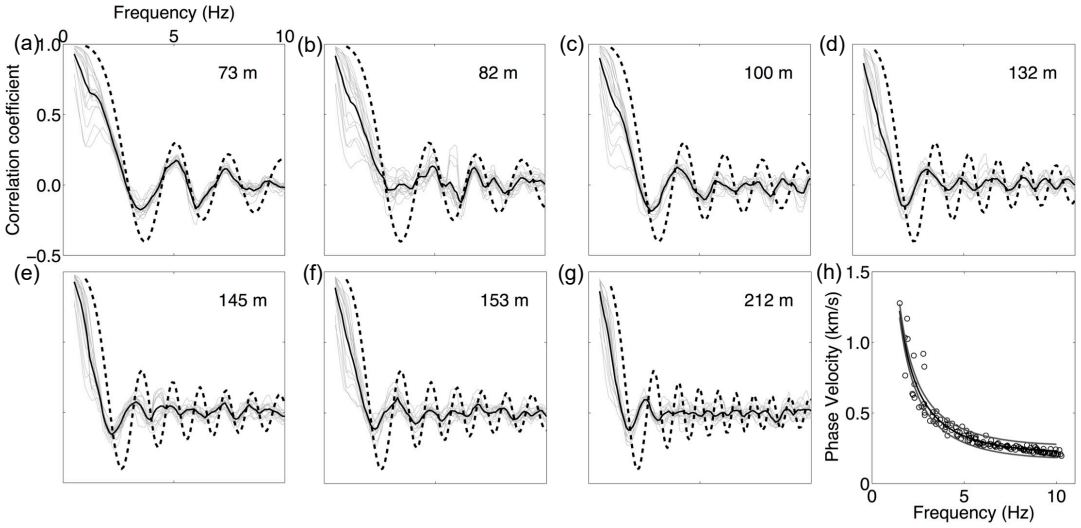

Figure 1.3. Azimuthal averages of the correlation coefficients obtained as a function of frequency for vertical components for the seven receiver spacings reported in the upper right corner of each plot. The black line shows the total average of all stations over all 16 300 s time intervals; the dashed line shows the Bessel function as defined by the model fit to the dispersion curve. The open circles in (h) are the phase velocities derived from zero crossings, maxima, and minima of the correlation data for vertical components. The thin gray lines in (h) are the extreme dispersion curves representing the 95% confidence limits on the dispersion function defined through the minimum misfit coefficients *A*, *b*, and *d* (described in text).

The same process was used for the horizontal components of motion, with the radial direction parallel to the azimuth between the stations of interest and the tangential direction measured clockwise from the radial in the perpendicular direction. Following the procedure outlined in Chouet *et al.* (1998) to estimate c_L, we assumed a value for ε ($0 \leq \varepsilon \leq 1$) and subtracted the Rayleigh contributions from the left sides of equation (1.2). Once the azimuthally averaged correlation coefficients were obtained for both radial and tangential components, we found the frequency values at the zero crossings, maxima, and minima as before. We then computed the dispersion characteristics using equation (1.3) but this time solving for Love waves (c_L). The correlations with the tangential components were poor, and we opted not to

consider them further. The best-fitting phase velocity curve was obtained by least squares as before, but with constants $A = 1398$, $b = 1.02$, and $d = -0.04$ and using $\varepsilon = 0.6$ to weigh the relative contributions of Rayleigh and Love waves (Figure 1.4).

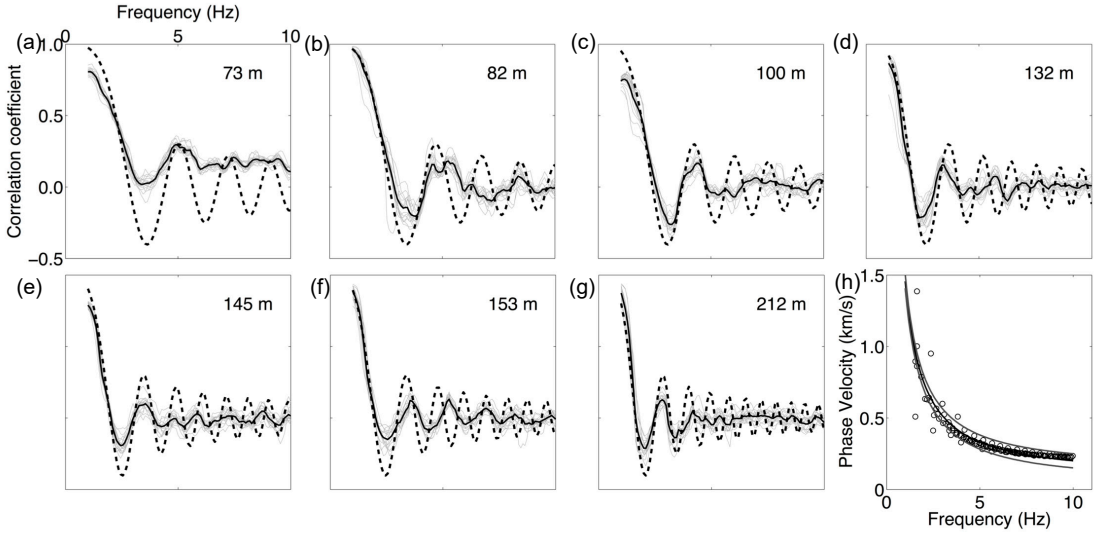

Figure 1.4. Azimuthal averages of the correlation coefficients as in Figure 1.3 but for radial components.

We tested the validity of the random-wavefield assumption in several ways. As shown in Figures 1.3 and 1.4, the correlation data derived from distinct time windows (light gray lines) share strong similarities, validating the assumption of a wavefield that is stationary in time. Contour maps of the correlation coefficients versus azimuth and frequency obtained for each receiver spacing do not show any predominant direction of wave propagation in the vertical component of motion nor in the radial or transverse components (Figure 1.5). Thus, the tremor wavefield can be regarded as composed of equal contributions from waves scattered by a source distributed over the whole azimuthal range. This supports the stationarity of the wavefield in space.

To further investigate the spatial characteristics of the wavefield, we performed directional analysis using deterministic plane-wave decomposition of the array. We performed frequency-slowness analysis over the selected 16 time windows

used in the SPAC analysis. We used a grid-search approach to find the best ray parameter and azimuth, based on evaluation of the semblance coefficient (Neidell and Taner, 1971) of band-pass-filtered data. There was little evidence for a dominant tremor direction. For example, with central frequency of 2.5 Hz, 2-Hz-wide, four-pole Butterworth filters and time windows of 3 s, semblance values were typically less than 0.2 and rarely above 0.4. No preferential azimuth directions of the wavefield were found in any of the investigated frequency bands. Overall, the fit of the theoretical functions to the experimental data supports the assumption of a stochastic wavefield dominated by dispersive surface waves. Therefore, while much of the tremor signal may be volcanic in origin, the absence of any dominant directionality pointing to the main volcanic source is due to the strongly scattering medium.

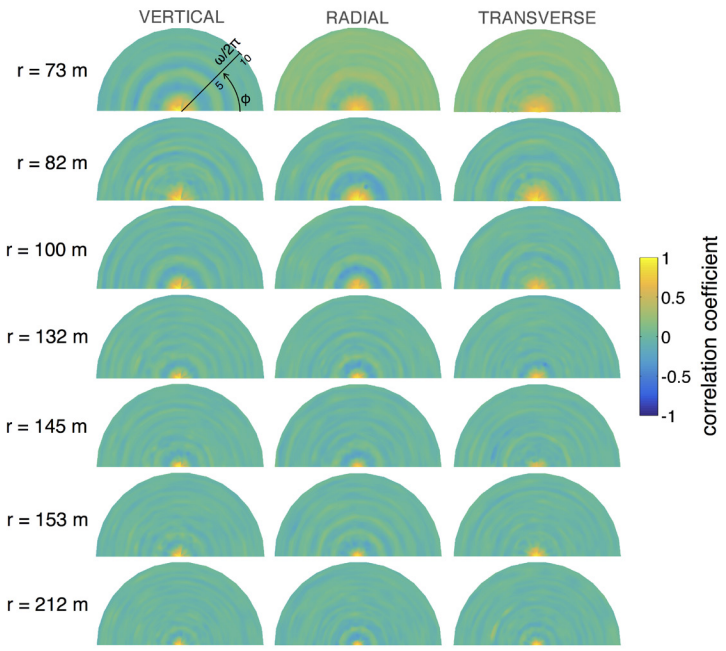

Figure 1.5. Correlation coefficients ρ (r; φ; ω_0), obtained as functions of frequency and azimuth for all receiver spacings. Vertical, radial, and transverse components of ground velocity are shown for each receiver spacing. All the maps are represented in polar coordinates in which the angle is the azimuth (φ) and the radius of the circular map is the frequency. The outermost circle corresponds to 10 Hz. Because of symmetry; we show only the top half of each map. The color version of this figure is available only in the electronic edition.

1.6. Dispersion Curves and Shallow Velocity Structure

We evaluated the uncertainties in our estimate of the phase velocities following the procedure outlined in Saccorotti *et al.* (2003). To derive error bounds to the best-fit model of the dispersion characteristics of Rayleigh and Love waves, we estimate the 95% confidence limits for the A , b , and d coefficients in equation (1.3) by calculating the inverse cumulative F -distribution for the appropriate number of independent data samples and model parameters (Menke, 1989, p. 96). For the vertical-component data and Rayleigh-wave dispersion, we have 2064 independent data samples (equal to 129 correlation coefficients for seven interreceiver distances, multiplied by 16 data windows) and three model parameters (A , b , and d). This yields 2061 degrees of freedom in our problem. The inverse cumulative F -distribution of the ratio of two random variables, each having 2061 degrees of freedom, yields a value of 1.075.

We then select those models for which the ratios of the variances of individual models to the variance of the model showing the minimum misfit are lower than or equal to 1.075. Models within this region are considered to give equivalent fits to the data with a probability of 95%. We use this set of models to retrieve the lower and higher values of phase velocity corresponding to the extreme dispersion curves that represent the 95% error limits. The same procedure is applied to the horizontal-component data, for which we have 2285 degrees of freedom (equal to 143 correlation coefficients for seven interreceiver distances, multiplied by 16 data windows, minus the three model parameters) and a value of 1.071.

Figures 1.3h and 1.4h show the dispersion characteristics of Rayleigh and Love waves, together with their error bounds, respectively. Very low velocities are observed in the dispersion curves. The phase velocities for Rayleigh waves range from 1000 m/s at 2 Hz to 230 m/s at 10 Hz; those for Love waves range from 600 to 250 m/s over the same frequency band. This is consistent with the presence of unconsolidated tephra deposits interspersed with lava flows in the shallow subsurface of the volcano.

Under the assumption that the dispersion curves represent the fundamental modes of Love and Rayleigh waves, we performed an iterative 1D inversion of the dispersion curves (Herrmann, 2013; see Data and Resources) to derive a shallow shear-wave velocity model beneath the array. To minimize the error between theoretical and observed data and to obtain the best fit to the dispersion curves, we perturbed our starting model by changing the layer velocities while keeping the layer thicknesses and Poisson ratio fixed. Because Rayleigh-wave velocities are more dependent on the shear-wave velocity rather than on density and Poisson ratio (Saccorotti *et al.*, 2003, and reference therein), we deem adequate for each inversion to consider a constant Poisson ratio and its corresponding V_P/V_S ratio. We iteratively inverted for the *S* -wave velocity alone and then updated the *P* velocity using the V_P/V_S ratio of the initial model; the new density is then computed from the new V_P using the Nafe– Drake relation (Ludwig *et al.*, 1970).

We followed a trial-and-error procedure in our search of phase velocities compatible with the experimental data and used different starting models in which we varied the initial starting V_S, the number of the layers, the thickness of the layers, and the initial V_P/V_S ratio. Layers are considered to be planar over the short aperture of the array so lateral heterogeneity is not investigated in the inversion of the velocity structure. Initial experiments conducted with different starting velocities and numbers of layers showed that the structural model for both Rayleigh and Love waves is best constrained in the upper 150 m, whereas the sensitivity decreases for greater depths. Below 500 m, the dispersion data provide little control on the modeled shear-wave velocities (Figure A1, available in the Appendix A to this thesis).

We then tested different initial V_P/V_S ratios, using Poisson ratios between 0.25 and 0.33. The fit to the dispersion data and its corresponding velocity structure is not affected by the initial V_P/V_S ratio. When different initial V_P/V_S ratios are used, the models have comparable fits to the dispersion data, with a strong control on the first few layers where the velocity structure is consistent.

The best-fit model to the dispersion curves that is associated with the

minimum misfit value was obtained with a Poisson ratio of 0.25 (see Figure A2, available in the Appendix A to this thesis). Our final structural model is composed of eight layers underlain by a homogeneous half-space. The model depth extends to 530 m below the surface of the volcano. Our data have little control on the velocity at greater depths. Figure 1.6 shows the velocity model and the associated best estimate of dispersion curves superimposed on the observed data. The model parameters are summarized in Table 1.1 Confidence limits in the dispersion curves and in the velocity structure are also shown. The error bounds in the velocity model were calculated from the inversions of the high- and low-confidence limits of the dispersion bounds.

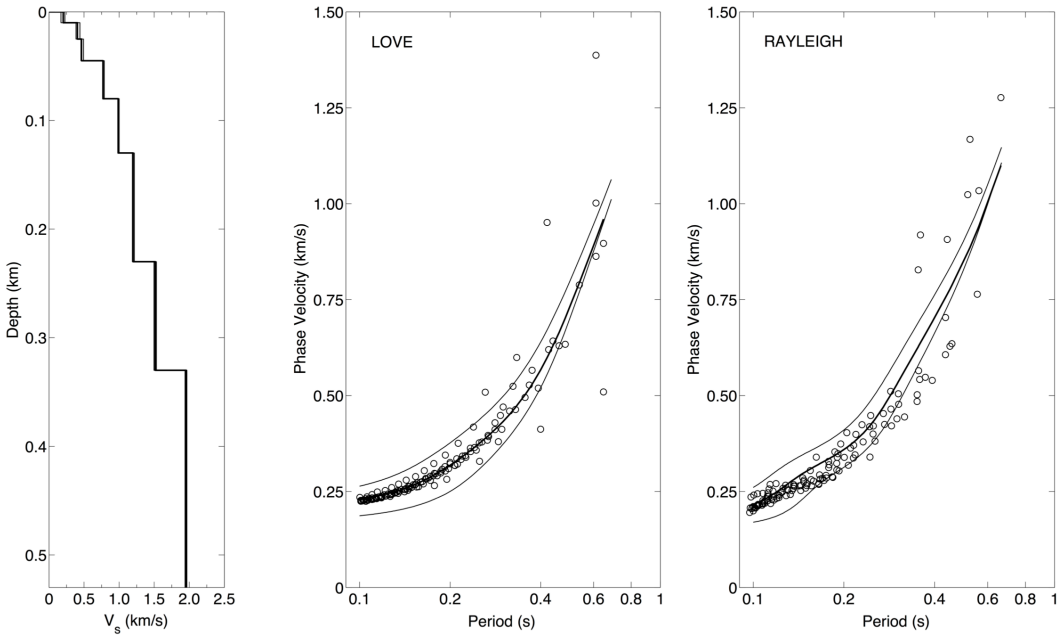

Figure 1.6. Best estimate of the shear-wave velocity model obtained from inversions for Rayleigh- and Love-wave dispersion curves from vertical and radial autocorrelations. Thin lines indicate error bounds in the velocity structure and in the dispersion curves, respectively.

Table 1.1 Velocity structure beneath the array

Layer	S Velocity (km/s)	Thickness (m)	Density (g/cm^3)
1	0.20	10	1.75
2	0.41	15	1.99
3	0.46	20	2.03
4	0.77	35	2.21
5	0.99	50	2.30
6	1.20	100	2.36
7	1.52	100	2.08
8	1.96	200	2.21
9	3.05	∞	2.56

1.7. Discussion and Conclusion

We investigated the properties of the background tremor at Pacaya volcano by deriving the dispersion characteristics for Rayleigh and Love waves using Aki's correlation method (Aki, 1957, 1965). The phase velocities were then inverted to obtain a model of the shallow shear-wave velocity structure beneath the array based on the assumption that the observed dispersions are representative of fundamental-mode surface waves. Although we have taken care to assure that most of our assumptions, such as the stochastic nature of the observed wavefield, are valid and conducted analyses of model and data uncertainties to confirm the robustness of our results, we acknowledge some limitations in our procedure. For example, the velocity model inversion is non-unique, because different models can fit the data equally well. In addition, the assumption of higher-mode Rayleigh and Love waves may contribute to the observed wavefield significantly enough to make our fundamental mode assumption invalid. However, determination of the dispersive properties of surface waves for higher modes is computationally expensive (Saccorotti *et al.*, 2003) and likely not possible with our current set of data and beyond the scope of the study.

The derived phase velocities point at a wavefield mostly composed of surface waves. The shear-wave velocity range (0.2–0.7 km/s at the surface and 1.3–2.3 km/s at depths greater than 200– 400 m) observed at Pacaya is comparable with the results

obtained at Stromboli by Chouet *et al.* (1998) and with other volcanoes around the world, including Puu Oo crater (Ferrazzini *et al.*, 1991), Masaya (Métaxian *et al.*, 1997), Somma–Vesuvius (De Luca *et al.*, 1997; Saccorotti, Maresca, *et al.*, 2001), and Deception Island (Saccorotti, Almendros, *et al.*, 2001). Chouet *et al.* (1998) inferred that a high density of cracks of the shallow lava flows underlying the surficial soil could explain the low-velocity values they derived. In light of these studies and the recent history of Pacaya, we interpret the structural model at Pacaya in terms of poorly unconsolidated airfall tephra materials interspersed with densely cracked lava flows.

Uncertainties in the shallow velocity structure of a volcanic edifice are a major source of error when computing source locations and source mechanisms for shallow volcanic events. We showed how the simple method used in the present study provides a 1D model of the shallow velocity structure that can guide the choice of a velocity model for seismic monitoring and further seismic studies at Pacaya.

1.8. Data and Resources

The instruments used in the field were provided by the Program for the Array Seismic Studies of the Continental Lithosphere (PASSCAL) facility of the Incorporated Research Institutions for Seismology (IRIS) through the PASSCAL Instrument Center at New Mexico Tech. Data collected during this experiment will be available through the IRIS Data Management Center. The facilities of the IRIS Consortium are supported by the National Science Foundation under Cooperative Agreement Number EAR-0552316 and by the Department of Energy-National Nuclear Security Administration. The velocity model beneath the array was obtained using the computer code surf96 v.3.30 (http://www.eas.slu.edu/eqc/eqccps.html, last accessed February 2016; Herrmann, 2013)

Acknowledgments

We thank J. Richardson, K. Brill, J. Wellik, J. Olson, L. Schaefer, and P. Manzoni for deploying the array in January 2011.We are grateful to Parque Nacional Volcán de Pacaya for allowing access and permission to install seismometers and the cooperation of the Instituto Nacional de Sismologìa, Vulcanologìa, Meterologìa and Hidrologìa (INSIVUMEH). We thank an anonymous reviewer and Gilberto Saccorotti for their valuable and insightful comments, which led to a substantial improvement of the article. Financial support was provided by National Science Foundation Grant Numbers EAR-1053794 and PIRE-0530109.

CHAPTER 2

A nonlinear approach to moment tensor sensitivity in volcanic settings[2]

[2] The material contained in this chapter has been submitted to the *Geophysical Journal International* and it is currently undergoing the second round of reviews.

Abstract

The characterization of seismic-source mechanisms and geometries is of critical importance for understanding the underlying causes and physical processes of low-frequency seismicity at volcanoes. Because observational data is often limited in volcanic environments by logistical constraints, in this study we use synthetic modeling to investigate the capability of seismic networks to properly resolve source mechanisms. For 16 synthetic networks with as many as 40 stations, and variable azimuthal distribution, we perform nonlinear moment-tensor inversion for six input source models. We use a grid search for source type and constrained inversions, which provides a quantitative measure of source mechanism reliability. If the source location is assumed to be correct, results suggest that complete azimuthal coverage, with stations located at different distance ranges from the source will allow for a higher resolution recovery of the source time function. In general, a similar degree of uncertainty characterizes configurations with as many as 40 stations and as few as 8 stations. Although the level of uncertainty in the source time function increases when fewer than 8 stations are used in the inversions, sources are still recoverable with as few as 4 stations are used. Deviations from this general trend are present across the different input source models, with performances of configurations with fewer than 8 stations showing a strong dependence on the source type.

2.1. Introduction

Volcanic eruptions involve a complex interaction of multiphase fluids with solid conduit walls. Seismology has shown great promise for modeling conduit dynamics (e.g., Chouet, 1996), as seismic signals can carry information related to fluid transport phenomena, such as coalescence of bubbles, ascent of gas slugs, or sealing and pressurization phenomena. Source modeling of seismic events beneath volcanoes can therefore produce models that correspond to fluid pathway processes and geometries, leading to a better understanding of the underlying causes and physical processes connected to eruption activity. A clearer picture of the dynamics of magmatic systems is achieved by the analysis of low-frequency events, which include tremor, long-period (LP) and very-long-period (VLP) events. Full-waveform moment-tensor inversion of seismic data has been a principal technique used to successfully derive seismic source mechanisms at a number of active volcanoes for both VLP and LP events. We refer to Chouet and Matoza (2013) for a recent review.

However, moment-tensor inversions are non-unique and bear intrinsic uncertainties due to simplifying assumptions about the source and structure; inaccuracies in the velocity models; and the dependence on network configuration. In order to advance source modeling, it is important to quantify the sensitivity of model results to these controlling variables. Various studies have focused on the influence of near-surface volcanic structure on moment-tensor inversions and demonstrated that simple velocity structure can have a detrimental effect on source inversions (e.g., Bean *et al.,* 2008). When the effects of near-surface structures are not taken into account, they can lead to the emergence of incorrectly oriented source geometries, spurious single forces and incorrect source time functions. Incorrect solutions are also related to volcano topography. Topographical scattering can produce path effects, which, in turn, can leak into the source solutions (O'Brien and Bean, 2009). A priori structural information and topography are therefore essential for modeling the nature of shallow short-duration volcano-seismic signals, such as LPs. In addition to near-surface low-velocity structure and topography, network configuration has a great influence on the nature of recorded LP seismic signals and moment tensor inversions.

The capability of seismic networks to accurately resolve source mechanisms and locations is one of the primary factors we need to consider in order to develop an accurate interpretation of seismic sources including whether they are related to fluids (hydrothermal, gas, or magma) moving into conduits and cracks (Dawson *et al.,* 2011) or if they originate by slow, brittle failure mechanisms (Eyre *et al.,* 2015). The effect of volcano seismic network configurations on source time function solutions has not been thoroughly investigated to date, but is especially important in volcanic environments where accessibility and equipment are often limited.

In this study, we focus on the sensitivity of source model results to network configuration through a nonlinear inversion for seismic source types using a variety of idealized networks, a known velocity model, and the topography of Pacaya volcano, Guatemala. Pacaya volcano is the subject of a companion study in which the nonlinear procedure described in this paper is applied to the source inversion of explosion-related long-period events (see Chapter 3). This nonlinear approach allows for quantification of the importance of Double-Couple (DC), or Compensated Linear Vector Dipole (CLVD) versus volumetric components and provides a quantitative description of moment tensor uncertainty. We use synthetic modeling to quantitatively explore the network configuration effects on moment tensor solutions. We test six different synthetic input source models and as many as 40 stations at variable azimuths to assess the influence of the network parameters (i.e., number of stations and azimuth coverage) that can contribute to an increase/decrease in the accuracy of the source type solution. We perform, for each network configuration, constrained inversions and search over all possible moment tensor types and orientations at the source model input location to compare model fits for all possible source types for different station configurations.

2.2. Inversion methodology

2.2.1. Full-waveform inversion procedure

We followed an inversion approach that is similar to other studies (see e.g., Auger *et al.,* 2006; Waite *et al.,* 2008; Dawson *et al.*, 2011; Richardson and Waite, 2013) where the inversion is performed in the frequency domain to reduce the computation time and permit a grid search over a large volume. The representation theorem to describe the displacement field generated by a point source in the frequency domain is:

$$u_n(\vec{r},\omega) = F_p(\omega) \cdot G_{np}(\vec{r},\omega) + M_{pq}(\omega) \cdot G_{np,q}(\vec{r},\omega) \quad (2.1)$$

where $u_n(\vec{r},\omega)$ is the Fourier transform of the *n* component of the seismogram, *p* and *q* are direction indices *x*, *y*, and *z*, $M_{pq}(\omega)$ is the Fourier transform of the time history of the *pq*-component of the moment tensor, and $G_{np}(\vec{r},\omega)$ is the tensor of the Green's functions that relates the *n*-component of displacement at the receiver position, $\vec{r}$, with the moment at the source position, and ω is angular frequency. The notation $,q$ indicates spatial differentiation with respect to the *q*-coordinate.

In matrix form equation (2.1) becomes:

$$\boldsymbol{U}(\omega) = \boldsymbol{G}(\omega)\boldsymbol{s}(\omega) \quad (2.2)$$

where $\boldsymbol{U}$ is the N_t x 1 vector of Fourier-transformed ground displacement components, $\boldsymbol{G}$ is the N_t x 9 (or 6) matrix of Fourier transforms of the Green's functions, $\boldsymbol{s}$ is the 9 (or 6) x 1 vector of Fourier transformed force and moment-tensor components (or moment-tensor components only), and N_t is the number of observed seismic traces.

We solved for the full spectra of the bandpass filtered seismograms and invert at each frequency separately by minimizing the least squares problem:

$$\boldsymbol{s}(\omega) = [\boldsymbol{G}(\omega)^T\boldsymbol{G}(\omega)]^{-1}\boldsymbol{G}^T(\omega)\boldsymbol{U}(\omega) \quad (2.3)$$

We then applied the inverse Fourier transforms to obtain the time estimates of both the source components and synthetic seismograms. In this paper, we refer to "unconstrained" or "free" inversion when we invert, using equation (2.3), for different combinations of the 9 free parameters (six moment-tensor components and three single forces). The term "constrained" inversion is used instead to describe inversion in which the moment tensor for the whole source time function is fixed. Constrained inversions are performed as part of the nonlinear inversion procedure which involves a grid search over all possible moment tensor types and orientations. Details of the constrained inversion are given in the next section.

For both free and constrained inversions, synthetic Green's functions were computed with the 3-D finite-difference method of Ohminato and Chouet (1997). We used a cosine smoothing function to synthetize the Green's functions and assure stability. This wavelet has a time –constant period of one second to approximate the peak frequency of the LP events recorded at Pacaya volcano. The Green's functions convolved with the cosine function represent the elementary source time functions used in the inversion. We used a model that includes the 3-D topography of Pacaya, derived from a digital elevation map (DEM) from 2006 with a resolution of 10 m. The model domain is centered on the active summit crater of the volcano, and it has lateral dimensions of 4 km by 4 km and a vertical extend of 3.5 km. This yields a model with 401 x 401 x 351 nodes spaced 10 m apart. All station locations were rounded to the nearest node, and topography was resampled to match the correct node grid. The node spacing does not violate the criterion of minimum number of grids per wavelength of 25 established by Ohminato and Chouet (1997). The model is also wide enough to minimize edge reflections of the boundaries while including all the stations. We considered a homogeneous velocity model with P-wave velocity of 978 m/s, S-wave velocity of 565 m/s and density of 1750 kg/m^3. These values represent the mean of the first 5 layers (first 130 m in depth) of the shear-wave velocity structure derived from Love and Rayleigh dispersion curves as in Lanza *et al.* (2016). While a homogeneous model is obviously not correct, it is appropriate for this study that is concerned primarily with source model sensitivity to station configuration.

To find the best location for each of the point sources, we conducted a grid search over a volume of 740 m x 740 m x 500 m centered on the summit vent at a spacing of 20 m. As the result of the 20 m grid spacing, the number of possible point source locations becomes quite large, 22,088, so 198,792 Green's functions are required for the inversion, as for each source location 9 Green's functions, correspondent to the 9 parameters (six moment-tensor components and three single forces), are calculated. Following Chouet *et al.* (2005), we used the reciprocal relation (Aki and Richards, 2002) between source and receiver, which greatly reduces the number of calculations required to derive the Green's functions. We treated each station as a point source and each potential source as a receiver. We calculated the spatial derivative between adjacent nodes in the potential source volume to generate the appropriate moment and single force components as if each source volume node were a point source instead of a receiver. We validated the Green's functions calculated this way by running forward models for selected nodes at the corners (bottom and up) of our point-source volume and comparing the results to those obtained by the reciprocal method. We found that the results from the two methods were indistinguishable for the eight nodes that we tested.

2.2.2. Nonlinear inversion procedure

The unconstrained moment-tensor inversion at hundreds of points within a three-dimensional (3D) model provides a spatial estimate of the location and its corresponding uncertainty. Moment tensor orientation and mechanism type can be obtained at the best-fitting source location using point-by-point eigenvector decomposition of the source time function (e.g., Chouet *et al.,* 2003). The moment-tensor can then be interpreted in terms of one or more physical components of the source model, such as cracks, pipes, or spherical sources. While this method has been very successful, it does not provide a means to assess the range of acceptable source types. We sought to expand on this approach by exploring the uncertainty in the source type through a grid search over all possible moment tensor types and

orientations (see also Waite and Lanza, 2016). In this nonlinear inversion, we do not attempt to include single-force contributions.

The search over source types is determined using the fundamental lune source-type definition of Tape and Tape (2012). Similar to a Hudson type plot (Hudson *et al.,* 1989), the lune maps the distribution of all possible moment tensor source types onto a surface. Source types are defined by two parameters, the spherical coordinates γ and δ, which are defined by the ratios of the moment tensor eigenvalues. The longitude parameter, γ, ranges from –30º to 30º, and it is defined as:

$$\gamma = arctan\left(\frac{-L_1 + 2L_2 - L_3}{\sqrt{3}\,(L_1 - L_3)}\right) \tag{2.4}$$

where L_1, L_2, and L_3 are the eigenvalues of each point of the source-time function.

The latitude parameter, δ, ranges from –90º to 90º, and it is derived from the co-latitude parameter, β, for which:

$$\beta = arccos\left(\frac{L_1 + L_2 + L_3}{\sqrt{3}\,||\mathbf{\Lambda}||}\right) \quad \text{with} \quad ||\mathbf{\Lambda}|| = \sqrt{L_1^2 + L_2^2 + L_3^2} \tag{2.5}$$

$$\delta = 90^o - \beta \tag{2.6}$$

where L_1, L_2, and L_3 are the eigenvalues of each point of the source time function. The latitude δ is zero for deviatoric patterns, and both δ and γ are zero for double couple mechanisms.

The search over the γ and δ uses the surface spline method described in Tape and Tape (2012), which effectively reduces the number of points required to evenly sample the distribution over an evenly spaced grid. We evaluate the full range of γ, but because the lower half of the lune is simply the opposite sign of the upper half (e.g., volume decrease versus volume increase), and we do not consider first motion polarity, we evaluate δ from 0 to 90º.

In addition to exploring the full source type space, the range of possible orientations for each source is also examined. To do this, we rotate the moment tensor

at 10º intervals using a sequence of three rotations about the initial coordinate system of the moment tensor. Complete sampling of the symmetric tensor orientations requires exploring three rotations: a full 360º range about one axis, for example, the z axis; a range from 0 to 180º of dip of z to z'; and finally, 90º of rotation about the new, rotated z' axis (Goldstein *et al.,* 2002; Waite and Lanza*,* 2016). The 10º interval was chosen for computational reasons and after having assessed, through multiple tests with finer intervals that although there are small changes in the misfit values there were no significant changes in the pattern of misfits. This involves 5832 combinations of rotation angles combined with 223 γ - δ pairs, for a total of 1,300,536 trial moment tensor solutions.

For each solution, the six moment tensor components of the trial tensor are used to constrain the inversion through a system of equations that fix the ratio of the moment tensor components (Menke, 1989). For a given trial tensor *n*, **H** is a matrix that contains the ratios of matrix components to arbitrarily selected component $\mathbf{M}_{11}^{(n)}$:

$$\mathbf{H}=\begin{bmatrix} 1 & -\mathbf{M}_{11}^{(n)}/\mathbf{M}_{22}^{(n)} & 0 & 0 & 0 & 0 \\ 1 & 0 & -\mathbf{M}_{11}^{(n)}/\mathbf{M}_{33}^{(n)} & 0 & 0 & 0 \\ 1 & 0 & 0 & -\mathbf{M}_{11}^{(n)}/\mathbf{M}_{12}^{(n)} & 0 & 0 \\ 1 & 0 & 0 & 0 & -\mathbf{M}_{11}^{(n)}/\mathbf{M}_{23}^{(n)} & 0 \\ 1 & 0 & 0 & 0 & 0 & -\mathbf{M}_{11}^{(n)}/\mathbf{M}_{13}^{(n)} \end{bmatrix} \quad (2.7)$$

where the notation $\mathbf{M}_{11}^{(n)}$ stands for the component (1,1) of trial moment tensor *n*, the vector **h** is a 5 x 1 column of zeros. A least-squares approach is used to solve simultaneously the constraint equations:

$$\begin{bmatrix} \mathbf{G}^{\mathbf{T}}\mathbf{G} & \mathbf{H}^{\mathbf{T}} \\ \mathbf{H} & \mathbf{Z} \end{bmatrix} \begin{bmatrix} \mathbf{s} \\ \mathbf{l} \end{bmatrix} = \begin{bmatrix} \mathbf{G}^{\mathbf{T}}\mathbf{u} \\ \mathbf{h} \end{bmatrix} \quad (2.8)$$

where **Z** is a 5 x 5 matrix of zeros, **h** is a 5 x 1 vector of zeros, **u** is the R x 1 vector of Fourier-transformed ground displacement components, **s** is the 6 x 1 vector of Fourier

transformed moment-tensor components to be determined, and R is the number of observed seismic traces. The vector **l** contains the Lagrange multipliers.

2.2.3. Evaluation of the results

In many applications of moment-tensor inversion at volcanoes, the overall selection of the best solution is based on a weighted squared error between the observed (or, in our case, synthetic) and reconstructed data, that is either normalized by station or channel (Chouet *et al.,* 2003; Ohminato *et al.,* 1998). In this study we adopted the squared error measure described as E_2:

$$E_2 = \frac{1}{N_r}\sum_{n=1}^{N_r}\left[\frac{\sum_{1}^{3}\sum_{p=1}^{N_s}\left(u_n^0(p\Delta t)-u_n^s(p\Delta t)\right)^2}{\sum_{1}^{3}\sum_{p=1}^{N_s}\left(u_n^0(p\Delta t)\right)^2}\right] \tag{2.9}$$

where $u_n^0(p\Delta t)$ is the pth sample of the nth data trace, $u_n^s(p\Delta t)$ is the pth sample of the nth synthetic trace, N_s is the number of samples in each trace, and N_r is the number of three-component receivers. Here the squared error is normalized by station, so that stations with varying amplitude contribute equally to the error. We use this measure for all of the free inversions and nonlinear inversions.

2.3. Synthetic Modeling

Small networks of temporary or permanent stations are common on active volcanoes, but it is not clear what the ideal network geometry or the recommended number of stations is for this type of study. Thus, we conducted an evaluation of the ability of 'synthetic' networks with as many as 40 stations to resolve key components of the moment tensor. This approach is similar to the work by Dawson *et al.* (2011) at Augustine volcano, Alaska, but in our case, we conducted a more exhaustive exploration of possible moment tensor source types. Importantly, this study does not

consider unknowns in the velocity model which can have important effects on waveforms in the LP band, especially at distances greater than a few km (e.g., Richardson and Waite, 2013). For longer period (VLP) sources, the velocity errors are less important given the much longer wavelengths.

We computed synthetic seismograms for six input source models: (1) a horizontal crack with dipole magnitude ratios of [1, 1, 2]; (2) a vertical crack with dipole magnitude ratios of [1, 3, 1]; (3) an isotropic source [1, 1, 1]; (4) a pure Compensated Linear Vector Dipole (CLVD) [2, -1, -1]; (5) a Linear Vector Dipole (LVD) [1, 1, 0], and (6) a DC [1, 0, -1] (in an east-north-up coordinate system). To synthesize a realistic set of seismograms, the Green's functions calculated for each input source model were convolved with a portion of the M_{xx} component of the source time function obtained from the free inversion of data collected at Pacaya (see Chapter 3). White noise was added to the final synthetic waveforms to give a signal-to-noise ratio of 2 to simulate noisy traces in real data. Synthetics were computed for an input location situated 260 m directly beneath the summit vent of Pacaya volcano, at 2330 m a. s. l. We explored the effect of network parameters for sixteen subsets of the synthetic network, each of them consisting of three to forty stations with variable azimuthal distribution, and whose geometries are shown in Figure 2.1. Configuration C8 was chosen to be identical to the actual local network deployed at Pacaya volcano in 2013 (see Chapter 3). Although we inverted for 16 different subnets for each source input model for a total of 96 configurations, we show here the analysis and results only of the most representative ones for clarity. Results from the configurations not discussed here can be found in Appendix B (Figures B1 through B6).

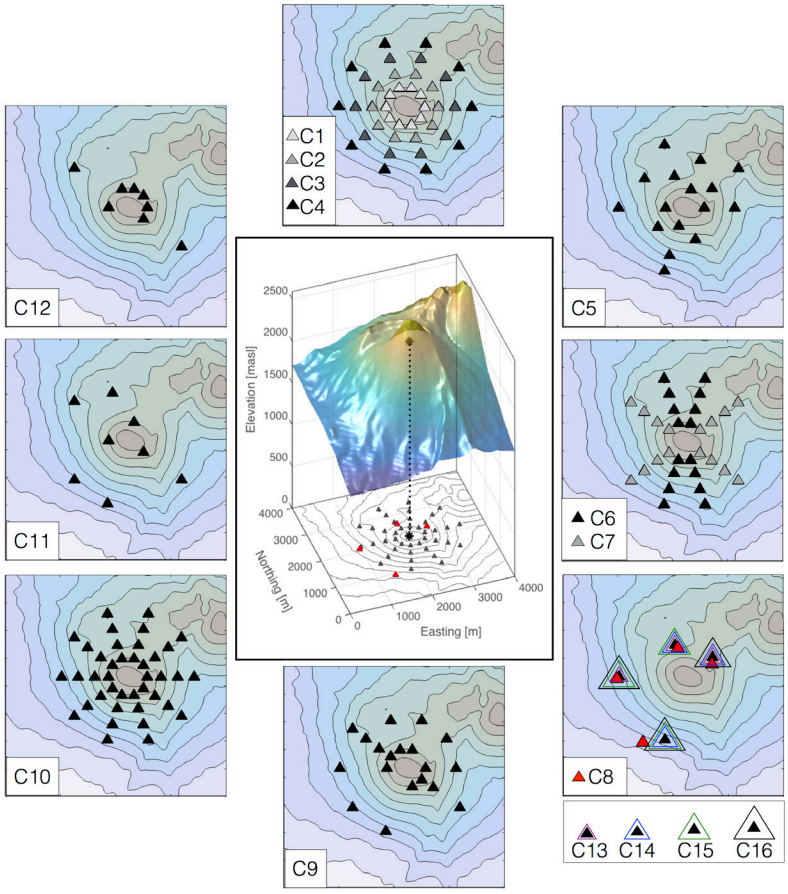

Figure 2.1. Subnet geometries of the 16 station configurations considered for the synthetic modeling. Input source model location is represented by the black star (central inset). Red triangles indicate the position of C8 which is identical to the network deployed at Pacaya during the October-November 2013 field campaign.

We chose to focus on subnets labeled in Figure 2.1 as C5, C6, C8 and C10 as they represent end-members of complete/poor azimuthal coverage, spanning the complete range of number of stations employed. Subnet C5 has16 stations at varying distance from the source with a complete azimuthal coverage; subnet C6 has16 stations clustered north and south the input source model; subnet C8 has only 4 stations with fairly good azimuth coverage; and subnet C10 includes all 40 stations. Subnet C8 reflects the location of the temporary seismic network deployed at Pacaya.

2.3.1. Free inversion results

All 96 configurations are freely inverted both with and without single forces in the solution. In general, inversion results show that single forces have very small contributions to the source time function. This is consistent with the fact that the synthetics were generated without single forces. Moreover, it has been demonstrated that the single forces term tends to absorb model errors while providing a numerically stable solution (Bean *et al.,* 2008; De Barros *et al.,* 2013). Because of the small magnitudes of the single force terms and the known synthetic model velocity, we do not consider the single forces further.

For each of the selected subnets of stations, the residual errors and locations of the best-fitting 6-component unconstrained inversions (E_{2min} solutions) are reported in Table 2.1. Table 2.1 shows that the best-fitting locations of all trials cluster to a small area around the original input model location, approximately within 20 m of the synthetic source location in both north-south and east-west directions. Larger variations, up to 120 m, are observed for depth and for those configurations that have fewer stations. A comprehensive table with the results from all 96 configurations is available in Appendix B, Table B1.

For comparison purposes and given the similarities in the best-fit centroid location to the input source location for all source models and subsets, we evaluated the consistency of the source time function at the input source location instead of the best-fit centroid obtained from the unconstrained inversion.

Table 2.1 Summary of the synthetic inversion results for 6-component unconstrained inversion

Subnet	# of stations	Input source	E_2	E_{2min} solutions			
				E-W position relative to input source [m]	N-S position relative to input source [m]	Depth position relative to input source [m] †	Eigenvalue ratios *
5	16	Isotropic (1, 1, 1)	0.265	0	0	0	1, 0.99, 0.96
							1, 1, 1
		Crack (1, 1, 2)	0.230	0	0	-20	1.07, 1.04, 2
							1.14, 1.01, 2
		Crack (1, 3, 1)	0.284	0	0	0	0.81, 3, 0.72
							0.84, 3, 0.76
		LVD (1, 1, 0)	0.279	0	0	0	1, 0.97, -0.03
							1, 0.96, 0.03
		CLVD (2, -1, -1)	0.259	0	0	0	2, -0.38, -0.45
							2, -1.16, -1.12
		DC (1, 0, -1)	0.319	0	0	-20	1, 0.17, -0.71
							1, 0, -1
6	16	Isotropic (1, 1, 1)	0.265	0	0	0	1, 0.95, 0.92
							1, 1, 1
		Crack (1, 1, 2)	0.242	0	0	-20	1.08, 1.01, 2
							1.06, 0.91, 2
		Crack (1, 3, 1)	0.295	0	0	0	1,.18, 3, 0.86
							1.2, 3, 1.05
		LVD (1, 1, 0)	0.280	0	0	0	1, 0.97, -0.04
							1, 0.96, 0.03
		CLVD (2, -1, -1)	0.252	0	0	0	2, -0.22, -0.37
							2, -1.10, -0.91
		DC (1, 0, -1)	0.273	0	0	-20	1, 0.25, -0.65
							1, 0, -1
8	4	Isotropic (1, 1, 1)	0.167	20 W	0	20	1, 0.97, 0.91
							1, 1, 1
		Crack (1, 1, 2)	0.254	0	0	-20	1.12, 1.07, 2
							1.14, 1.1, 2
		Crack (1, 3, 1)	0.140	0	0	20	0.88, 3, 0.66
							0.84, 3, 0.76
		LVD (1, 1, 0)	0.157	20 E	20 N	-60	1, 0.87, -0.2
							1, 0.99, -0.16
		CLVD (2, -1, -1)	0.150	40 W	20 S	40	2, -0.35, -0.42
							2, -1.1,- 0.91
		DC (1, 0, -1)	0.192	0	20 N	-40	1, 0.22, -0.43
							1, 0.09, -0.95
10	40	Isotropic (1, 1, 1)	0.277	0	0	0	1, 0.97, 0.96
							1, 1, 1
		Crack (1, 1, 2)	0.252	0	0	-20	1.03, 1, 2
							1.14, 1.1, 2
		Crack (1, 3, 1)	0.282	0	0	0	0.98, 3, 0.87
							0.84, 3, 0.76
		LVD (1, 1, 0)	0.282	0	0	0	1, 0.97, -0.04
							1, 0.96, 0.03
		CLVD (2, -1, -1)	0.265	0	0	0	2, -0.41, -0.46
							2, -1.16, -1.12
		DC (1, 0, -1)	0.291	0	0	0	1, 0.14, -0.72
							1, 0, -1

† Positive depth values indicate shallower depth with respect to the input location

* The first row associated with each source type shows the eigenvalue ratios of the free inversion solution at the input source location; the second row reports the eignvalue ratios of the constrained inversion solution at the input source location.

The consistency of the source time function over its duration is measured through point-by-point eigenvector decomposition (Chouet *et al.,* 2003; Waite *et al.,* 2008). Whereas the ratios of the eigenvalues of the scalar moment tensor give insight into the source mechanism, the eigenvectors give the orientation of the principal axes. We only consider points with amplitudes of at least 80% of the peak amplitude for this analysis. For the selected configurations (C5, C6, C8 and C10) the median ratios of minimum and intermediate eigenvalues to the largest are reported in Table 2.1. In general, the ratios of the eigenvalues are in agreement with the input source mechanisms. Note that the eigenvalue ratios refer, for both free and constrained solutions (see next section for details on the constrained inversion), to the solutions at the input source location rather than at each best-fit centroid (E_{2min} solutions).

We further examined the source-time history by calculating the lune longitude γ and the latitude δ for each point of the source-time history of each moment tensor. The use of γ - δ representation can be very useful to quantify the stability of the derived moment tensor source type. We represent each point of the source-time history in the γ - δ space. Points with negative δ were projected to the upper portion of the plot (Figure 2.2).

Altogether, the point-by-point decomposition of the moment tensor source time functions and the γ - δ representation shows that all source models are well recovered with the best fits for the isotropic source and poor fits for the CLVD and DC sources. Greater inconsistency, indicated by greater scattering in both γ and δ values, is associated with subnets that either have an uneven azimuthal coverage (C6), or fewer stations (C8), although the poor azimuthal coverage seems to have a higher impact on degrading the subnet performances with respect to the number of stations.

In general, if the azimuthal coverage and the number of stations are the same, the distance from the source (closer or farther) does not seem to significantly affect the stability of the moment tensor solution (e.g., subnets C1 through C4). However, velocity structures at volcanoes can commonly be complicated by near-surface low-velocity layers which introduce errors in velocity models and require consideration of

signal contamination from path effects. Other studies have therefore suggested deploying stations as close to the source as possible (e.g., Neuberg and Pointer, 2000). Decreasing the number of stations from 10 to 8 (subnets C11 and C12), while maintaining good azimuth coverage does not decrease the resolution of the source-time functions. This pattern is common for all six source input models.

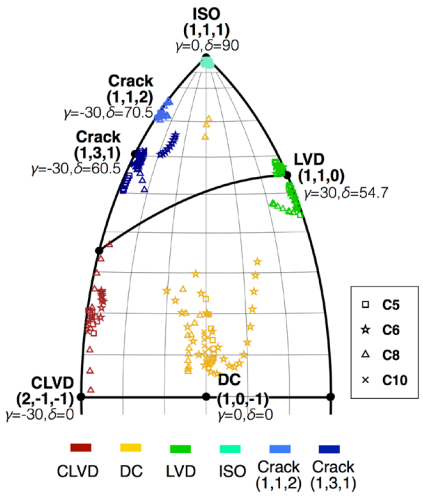

Figure 2.2. Point-by-point decomposition of the source time functions represented in the γ -δ plane for the results of the free inversion for each input source model. For clarity, only the four most representative station configurations are shown (subnets C5, C6, C8, and C10). Colors refer to the six input source types considered in the study. Points with negative δ are projected to the upper portion of the plot.

2.3.2. Constrained inversion results

One of the advantages of synthetic modeling is that there are no uncertainties in the velocity model, meaning the differences in the source time functions across the different subnets must be attributed to other factors. We further investigated these differences in source mechanisms when considering different subnets by performing a nonlinear inversion for source type. For each of the subnets and source models, the input model location was used to investigate the constraint on the source type. In Figure 2.3 we show the misfits for the selected subnets; for each moment tensor type the orientation that gives the lowest misfit is used. The point-by-point source time function eigenvector analysis for the free inversions that were plotted in Figure 2.2

are shown in the appropriate plots with white circles. The contours define the misfit values for all moment tensor orientations for each γ - δ pair in the lune plot.

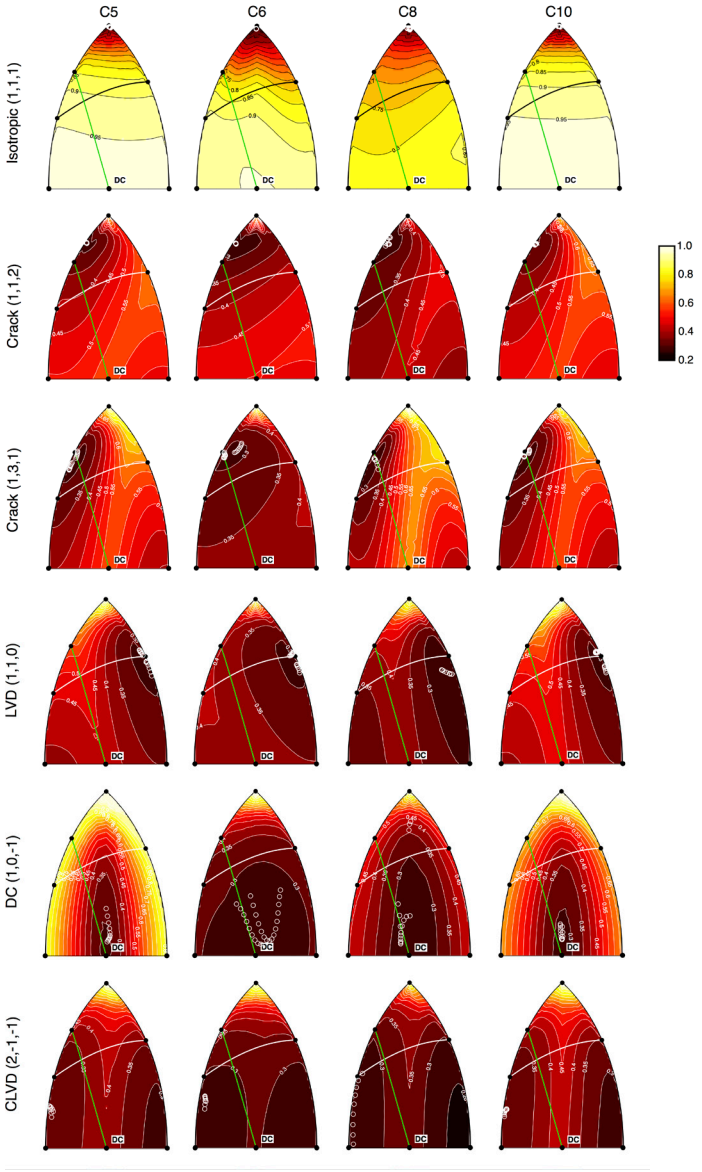

Figure 2.3. Error by fixed moment tensor solution, plotted together with the point-by-point mechanism type for the free inversion as white circles. The lack of stability in the free inversion for subnet C6 is reflected in the lack of a resolved moment tensor in the constrained inversion for almost all input source models. Only the four subnets discussed in the text are shown here for clarity. Note that for the CLVD input source the white circles, representing the point-by-point decomposition for the free inversion, are plotted on the left side of the lune as a result of the projection of the negative points in the upper-half portion of the lune.

To give a sense of the waveform fits on individual channels, we computed cross-correlation coefficients and lag times between the synthetic data and the free inversion synthetics, the constrained inversion synthetics at the lowest misfit value of the contour error maps shown in Figure 2.3, and the constrained inversion synthetics at the highest misfit value. Figure 2.4 shows an example of the waveform fits for the four configurations discussed in the paper in the case of a CLVD input source. For clarity we show only station number 14 as this station is common to all subnets considered, except for subnet 8, in which a different set of stations are used as it reflects the actual local network installed at Pacaya volcano. However, station 14 is located only few meters away from the location of station P03 of the seismic array, therefore we deemed acceptable to use station 14 also for subnet 8, in order to ease the comparison.

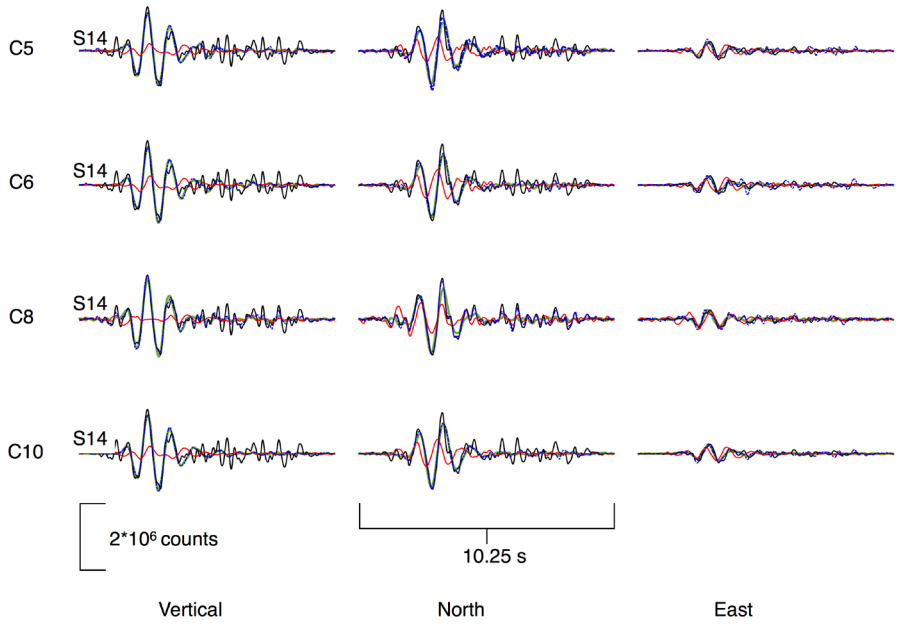

Figure 2.4. Data (black line), free-inversion synthetics (dotted blue line), best-fitting constrained inversion synthetics (green line), and worst-fitting constrained inversion synthetics (red line) are shown for a CLVD source for each of the four configurations discussed in the paper: C5, C6, C8, and C10. Only station 14 is shown. The free inversion results are in good agreement with the best-fitting constrained inversion models.

The waveform fits at almost all channels, with some exceptions for the east channel, for the free inversion and for the best fits of the constrained inversion are above 0.82 at lags of between -0.02 and 0.08 s. This indicates a highly agreement between the waveform fits from the free and best fixed inversions. In contrast, all channels for the worst fixed inversion model clearly fit less well, with correlation coefficients below 0.73 and lags comprises between -1.64 and 0.24 s (Table 2.2*).*

Table 2.2. Correlations between data from one common station (S14) and synthetic waveforms from the free and constrained inversion models, and corresponding lag times, for each channel used.

Inversion type	Subnet	Channel	Corr. coef.	Lag [s]	Channel	Corr. coef.	Lag [s]	Channel	Corr. coef.	Lag [s]
free	C5	S14 Z	0.85	0.00	S14 N	0.88	0.00	S14 E	0.64	0.06
	C6	S14 Z	0.85	0.00	S14 N	0.87	-0.02	S14 E	0.68	0.08
	C8	S14 Z	0.94	0.00	S14 N	0.98	0.00	S14 E	0.83	0.00
	C10	S14 Z	0.84	0.00	S14 N	0.86	0.00	S14 E	0.72	0.06
constrained (min E_{2min})	C5	S14 Z	0.87	0.00	S14 N	0.86	-0.02	S14 E	0.83	0.04
	C6	S14 Z	0.85	0.00	S14 N	0.87	0.00	S14 E	0.85	0.04
	C8	S14 Z	0.89	0.00	S14 N	0.88	0.00	S14 E	0.82	0.04
	C10	S14 Z	0.86	0.00	S14 N	0.86	0.00	S14 E	0.86	0.04
constrained (max E_{2min})	C5	S14 Z	0.54	-1.46	S14 N	0.68	0.18	S14 E	0.63	0.16
	C6	S14 Z	0.54	-1.46	S14 N	0.67	0.24	S14 E	0.70	-0.72
	C8	S14 Z	0.47	-1.64	S14 N	0.71	0.00	S14 E	0.61	-0.04
	C10	S14 Z	0.55	-1.46	S14 N	0.73	0.20	S14 E	0.67	0.14

The nonlinear analysis confirms the general observations from the inversion inversions and adds to the characterization of the uncertainties associated with the best fits. Clearly, subnet C6, in which we have an uneven station distribution with respect to the azimuth, shows fairly broad uncertainties. When considering networks with the same excellent azimuthal distribution but different numbers of stations, similar fits are reached for subnet C5 (16 stations) and subnet C10 (40 stations) indicating the resolution of the moment tensors does not improve when a larger number of stations is included in the inversion. This is also shown more quantitatively in Figure 2.5, where the portion (expressed in percentage) of the lune below a chosen cut off of E_2 equal to 0.35 is plotted across different configurations for all the input source types. In general, results computed with larger numbers of stations are better (they have a small lune portion below $E_2 = 0.35$) than results computed with just a few stations. But this plot also highlights the importance of azimuthal distribution.

Configurations with good azimuthal coverage, (e.g., C5 or C7 which have maximum azimuthal gaps between adjacent stations < 130°), perform much better than configurations with the same number of stations but larger azimuthal gaps (e.g., configuration C6). For all mechanisms, a similar percentage is calculated for configurations that include as many as 40 stations and as low as 8 stations. This is good news for those cases when deployments are limited due to logistical issues or lack of resources.

For configurations with fewer than 8 stations the quality of the model fits becomes strongly dependent on the input source model. For example, in the case of subnet C8, which includes only 4 stations, a crack mechanism is recovered and resolved with accuracy similar to other configurations with more stations. However, for source types with smaller contribution of the volumetric component, C8 has more dispersed γ - δ pairs and wider range of possible mechanism types with lune portions of about double the average of the other configurations with more stations. Higher uncertainties and poorly-constrained source time functions usually characterize configurations with fewer than 4 stations.

Furthermore, we observe that, for those source models that do not have a volumetric component, the source inversion generally has a wider range of acceptable models than for those with a volumetric component. The nonlinear inversion for source type for CLVD and DC input models suggests a wider range of possible mechanism types fit the data across all configurations, even though the waveform fits at the lowest misfit values shows high correlation. For example, the range of acceptable solutions ($E_2 < 0.35$) for a CLVD input source model includes volumetric sources in some cases. As might be expected, this problem is most significant for network configurations with smaller numbers of stations and poor azimuthal coverage.

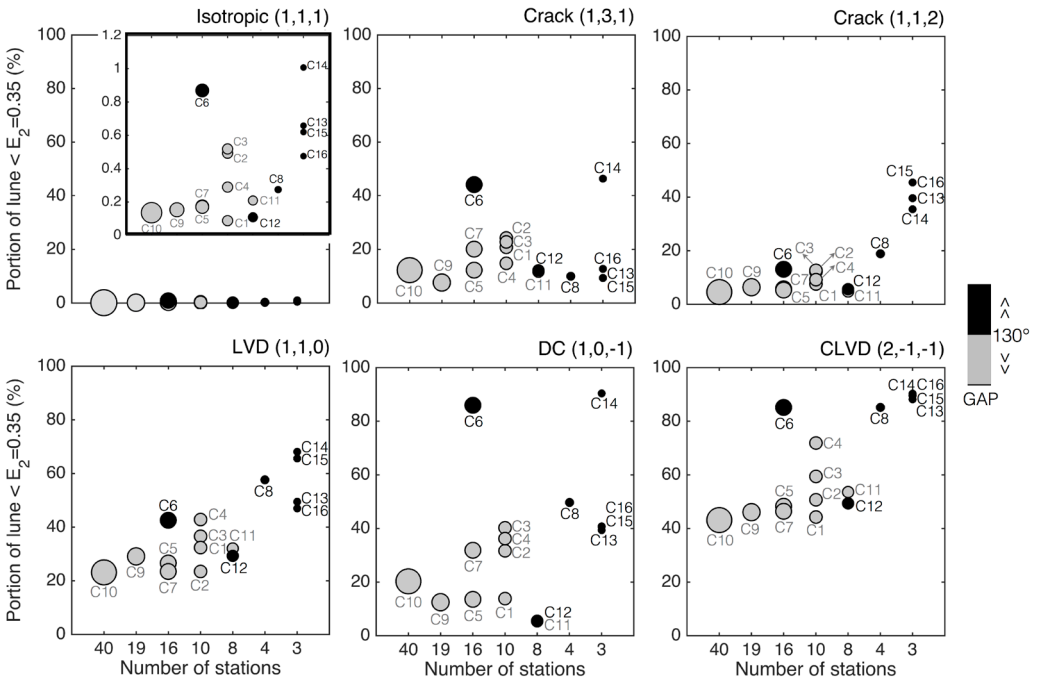

Figure 2.5. Portion of the lune space below E_2 cutoff of 0.35 for all 16 configurations across the six input source models. The size of the circles is proportional to the number of stations of each network. Configurations with azimuthal gap greater than 130° are shown in black.

Finally, we also explored the affect of source depth on the resolution. This might be especially important in the case of volcanic sources where all stations are on the edifice at a range of elevations. We applied the same inversion procedure to (1) deeper input source models located at 1400 m a.s.l., about 250 m below the lowest station; and (2) shallower input source models located at 2490 m a.s.l.,100 m below the highest topography point. Somewhat surprisingly, the results of these tests do not demonstrate significant differences in the misfits between the three source locations. Even with a smaller volumetric coverage, the solution does not degrade with depth.

We also observed that there is not a significant difference in moment tensor resolution for configurations with closer stations as opposed to those with stations located farther away from the source, assuming an equivalent azimuth distribution. This finding is likely only valid in our synthetic tests where the velocity structure is perfectly known. Errors in the velocity model due to the complicated near-surface

velocity structure commonly found at volcanoes, can lead to source contamination from path effects which increase with distance from the source.

The nonlinear inversion procedure not only allows us to quantify the uncertainty of the source type, but also provides a means to explore the range of acceptable source orientations. We analyzed the relation between misfits and orientation of the source mechanisms for the best-fitting γ - δ pair for all station configurations and for each of the source input models, with the exclusion of the isotropic case. Perhaps unsurprisingly we found that the subnets with a better moment tensor resolution appear to have a better control on the geometry of the source, but overall we found that the orientations of the moment tensors are well constrained. Figure 2.6 shows rose diagrams of φ (azimuth) and ϑ (inclination angle) for moment tensor solutions whose orientations have E_2 values within 5% of the absolute minimum E_2. Only the vertical crack and the DC mechanism are shown, as the different symmetries of the other input mechanisms do not allow for a meaningful comparison. We show only the orientation of the maximum eigenvector. For a DC mechanism, if we compare subnet C6, which has been shown to have the worst fits among the subnets, with subnet C10, which has the best fits, subnet C6 shows a wider range of φ orientations for similar misfit values. For the vertical crack, we observe small wider range in the ϑ values for C6 and C8 where the stations are either poorly distributed or in small number. The azimuth orientation is instead well constrained across the configurations. In general, this suggests that errors not only in the source type, but also in the geometry of the retrieved mechanism, are more likely introduced when azimuth and/or number of stations is inadequate.

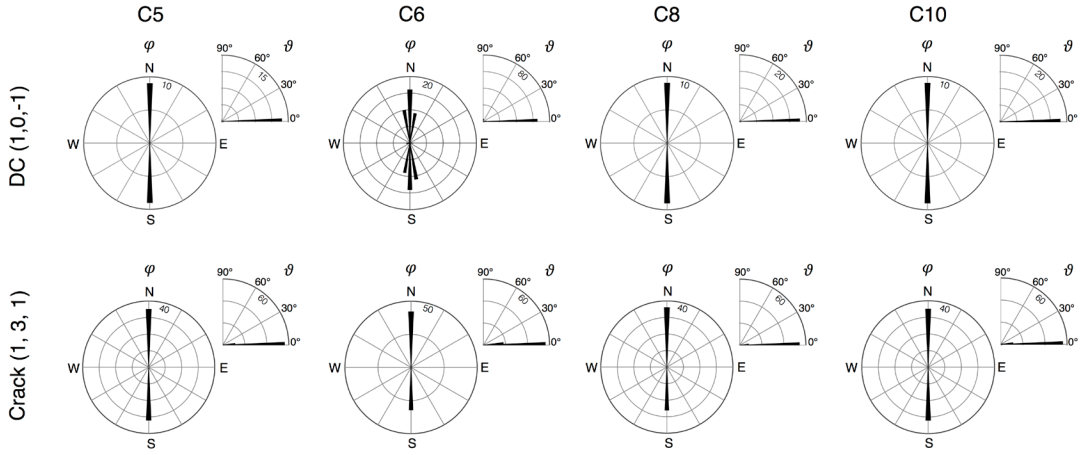

Figure 2.6. Rose diagrams for azimuth (φ) and inclinations angles (ϑ) of moment tensor solution with E_2 within 5 % for the absolute minimum E_2. Only the maximum eigenvector is shown for DC and vertical crack input source models.

2.4. Concluding remarks

We investigated the capability and accuracy of limited seismic networks that are common on volcanoes to recover source mechanisms using synthetic modeling. We examined six mechanism types with 16 network configurations using a nonlinear inversion approach. Because we explore the entire solution space, this inversion approach for source type provides quantitative constraints on source model uncertainty, which can aid in the interpretation of mechanism types. The importance of showing the variations of the misfits over the space of source types is also highlighted in Alvizuri and Tape (2016) where uncertainty estimation of moment tensors of small magnitude events at Uturuncu volcano, Bolivia, is represented by the variance reduction for the misfit function between the observed and synthetic waveforms. While we do not explore the affects of unmodeled structure on modeling in this study, the results should serve as a guide to interpreting models as well as planning temporary experiments on volcanoes.

One observation from this study is that larger numbers of stations are nearly always better, but when network sizes are equal, azimuthal distribution has an important effect. When azimuthal instrument coverage is poor, that is, when the gap

is greater than 130°, the model uncertainty increases dramatically. Solutions were generally good across all input source models when more than 8 stations where considered, but no significant improvements were reached by employing more than 16 stations.

Uncertainty, as measured by the percentage of the total model space below a chosen misfit value increases gradually with decreasing numbers of stations, but then rises dramatically when just three stations are used. Based on these observations, networks with as few as four stations should be capable of modeling moment tensors provided they are well distributed. However, we find that for smaller numbers of stations, the resolution of the recovered source time function is somewhat dependent on the source type; lower uncertainties are generally associated with source mechanisms having a higher volumetric component and CLVD sources are particularly difficult to constrain. Nonetheless, the waveform fits for the best-fitting constrained inversion model agree well with the free inversion solution.

The use of known velocities and densities in a model with realistic 3D topography allows for isolation of model sensitivity to network geometry. While we did not explore the significance of unmodeled structure in this study, we suspect that effects related to smaller numbers of stations, and especially networks with more distant stations, will be magnified if there are significant errors in the Green functions. The influence of realistic unmodeled structure is examined in Chapter 3, in which we find this nonlinear approach to be promising not only for synthetic testing, but for modeling real data as well.

Acknowledgments

This work was supported by National Science Foundation Award No. 1053794.

CHAPTER 3

Nonlinear moment tensor inversion at Pacaya volcano, Guatemala: a data application[3]

[3] The material contained in this chapter has been submitted to the *Geophysical Journal International* and it is currently undergoing the second round of reviews.

Abstract

Detailed models of low-frequency seismicity at volcanoes provide insights into conduit structure and dynamics of magmatic systems. We examine explosion-related long-period (LP) events from Pacaya volcano, Guatemala, that were recorded during a temporary installation of four broadband seismic stations from October 2013 to November 2013. The repetitive LP events are identified with the aid of infrasound measurements using a matched filter due to the high level of background tremor and the small magnitude of the recorded events. We derive a representative seismic signal from the phase-weighted stack of 8,587 of these similar events, and invert for a source moment tensor. To address the limitations posed by the limited number of stations of the local network, we use a recently developed non-linear waveform inversion that uses a grid search for source type to obtain a quantitative measure of the source mechanism reliability. With only 4 stations, Pacaya represents a case of limited availability of resources and observational data, where a quantitative description of moment tensor uncertainty is needed before any interpretation is to be attempted. Results point to a shallow source mechanism somewhat like a crack, dipping ~ 40° to the east. The uncertainties determined from the non-linear inversion are not insignificant, but clearly constrain the mechanism to be a volumetric source.

3.1. Introduction

Pacaya volcano (14.381°N, 90.601°W) is a 2552 m high composite stratovolcano located about 30 km SSW of Guatemala City, in the Central American Volcanic Arc (Figure 3.1). The current eruptive phase began in 1961, and has seen persistent degassing interrupted by intermittent strombolian-type eruptions from the active summit vent (Mackenney cone) and lava flows extruding from the flanks of the Mackenney cone (Rose *et al*., 2013). Beginning in January 2013, the volcano entered a new period of increased activity characterized by more continuous and energetic strombolian eruptions, ash eruptions, and lava flows often accompanied by strong seismic tremor as reported by INSIVUMEH (Instituto Nacional de Sismologìa, Vulcanologìa, Meterologìa and Hidrologìa). Tremor was not only recorded by the INSIVUMEH seismic network, but it was also felt by the population of the nearby villages (Gustavo Chigna, personal communication).

This new unrest prompted the installation of a local network to augment the single permanent station with the aim of monitoring and investigating the seismic activity. Seismic signals produced by volcanoes can be seen as windows to magmatic systems and the complex interactions between gas, liquid, and solid along magma pathways (Chouet, 1996). Their origin can be related to fluid transport phenomena as well as shear failure along conduit walls. Models of these pathways, processes, and geometries can be extrapolated by retrieving the source mechanisms of the seismic events occurring beneath volcanoes. In particular, the analysis of low-frequency events, which include tremor, long-period (LP) and very-long-period (VLP) signals, has been a powerful tool to discern information on the physical processes connected to eruption activity. Source geometries and mechanisms for LPs and VLPs are obtained with full-waveform moment-tensor inversion. This technique has been used successfully at numerous active volcanoes around the world (Chouet and Matoza, 2013).

This study focuses on modeling the source mechanism of thousands of small LP events associated with weak strombolian explosions at the summit vent of Pacaya

volcano. Due to the limited number of stations available for the seismic experiment, we extend the conventional moment-tensor inversion with a recently developed nonlinear inversion for source types (Waite and Lanza, 2016; see also Chapter 2). The latter adds a more thorough quantitative evaluation of source mechanism reliability. The procedure involves a grid search over all possible moment tensor types and orientations at the best-fit centroid location. The results provide arrange of acceptable models that fit the data.

3.2. Data Acquisition and Processing

3.2.1. Temporary seismic network

We conducted a seismic experiment at Pacaya volcano during October-November 2013 to study the continuous tremor-like signals and the explosions occurring at the summit crater. Three Guralp CMG-ESPC 3-component broadband seismometers (60s corner period) and one Guralp CMG-40T sensor (30s corner period) were installed around the central vent at distances between 0.6 and 1.5 km from the crater (Figure 3.1).

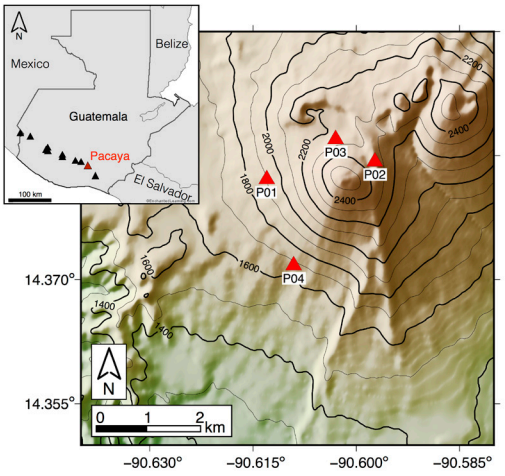

Figure 3.1. Map of Pacaya volcano showing the location of the seismic stations used in this study (red triangles). Contour interval is 100 m. The box in the upper left corner shows the position of Pacaya volcano in Guatemala with respect to the Central American Volcanic Arc volcanoes marked as black triangles.

Two of these stations (P01 and P02) were also outfitted with 3-element, equilateral triangular infrasound arrays, with ~30 m between elements. Data were recorded on Reftek 130 digitizers operating in continuous mode at 125 samples per second and equipped with Global Positioning Systems (GPS) timing. Concerns about vandalism and theft discouraged us from deploying solar panels; therefore the experiment ran for about 10 days from 31 October through 10 November.

3.2.2. LP events

The infrasound network recorded thousands of impulsive events with an inter-event time of about 1-2 seconds. Because the events were better recorded in the infrasound than the seismic, we used one of these events as a template and performed waveform cross-correlation to search for similar events within the acoustic record. By applying a time-domain matched filter approach, we were able to identify hundreds of events that correlated with the template with a cross-correlation coefficient of 0.9 or higher, which were stacked to create a new template (Shearer, 1994*;* Richardson and Waite, 2013). To improve the signal-to-noise (S/N) ratio of the template, we then ran this new template through the dataset again with a cross-correlation cut off of 0.8. In this way, we identified more than 30,000 events over a 5-day long period from 31 October to 4 November 2013. This infrasound catalog was then used to extract the corresponding waveforms from seismic data. This revealed the presence of a repetitive seismic signal (LP event type) associated with each acoustic emission that was not clearly visible above the background tremor and/or other noise sources (Figure 3.2).

While the infrasound data helped to identify the associated seismic event, the seismic data had minor time shifts when aligned with the times of the infrasound events. While the seismic velocity structure was presumably stable over the course of the deployment, variations in wind velocity and air temperature may have produced small variations in the sound speed profile between the vent and our array. In order to overcome this, we cross-correlated one channel of the seismic data at each station to

determine time shifts that would improve the alignment. These shifts were on the order of 0.1 s.

We reduced the number of events from 32,908 to 8,587 by considering only those events that have a S/N ratio greater than 1.2 on the east component of station P02. We then followed the phase-weighted stacking approach (Schimmel and Paulssen, 1997; Thurber *et al*., 2014), which resulted in waveforms with a much improved signal to noise ratio when compared to the linear stacks. Although the phase-weighted stack is slightly lower in amplitude, the pre- or post-event noise is much lower (Figure 3.2).

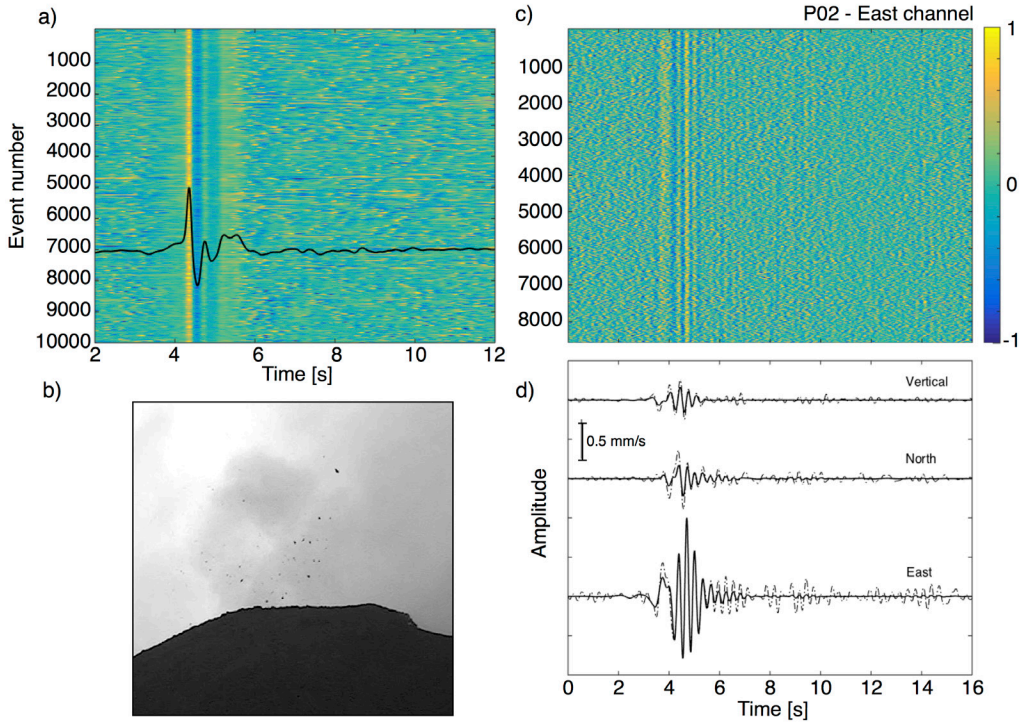

Figure 3.2. a) Waveforms of 10,101 events on the infrasonic record over a 5-day long period from 31 October to 4 November 2013, normalized to the maximum absolute amplitude. Plotted in black is the stacked infrasound template event used in the matched filter approach. b) Image of one small explosion at the crater recorded on November 3, 2013. c) Unfiltered waveforms of 8,587 seismic events observed on station P02 (east channel) over the same 5-day long period, normalized to the maximum absolute amplitude. d) Stacked seismograms for all three-components at station P02. Both linear time-domain (dashed lines) and phase-weighted stacks (bold lines) are shown.

One additional challenge in obtaining a representative stacked seismic event resulted from the somewhat discontinuous nature of the seismic data. Because the stations were not all contemporaneously operational, simply stacking waveforms to obtain a waveform that would synthesize the response from all four stations would produce a stack with disproportionally low amplitudes for those stations with fewer events. We employed a method described by Richardson and Waite (2013) to assure correct amplitudes in the stacks. As station P02 was running concurrently with all the other stations, we used it to tie events recorded by different stations and to compare amplitudes. Since the east component is consistently the highest amplitude component for P02, we used it as the reference channel. For each of the other stations, we generated temporary stacked seismograms of P02 east that included only the events recorded by the station of interest. We then calculated the ratio of the stacked amplitude for a particular component to that of the P02 east component stack for the same subset of events. In this way, all the channels were converted from stacked amplitudes to amplitudes proportional to the east component of P02 (Figure 3.3). All relative amplitudes were then converted back to true amplitudes proportional to one of the largest observed LP events seen at P02 through simple multiplication of each trace by the maximum velocity amplitude of P02 for that event.

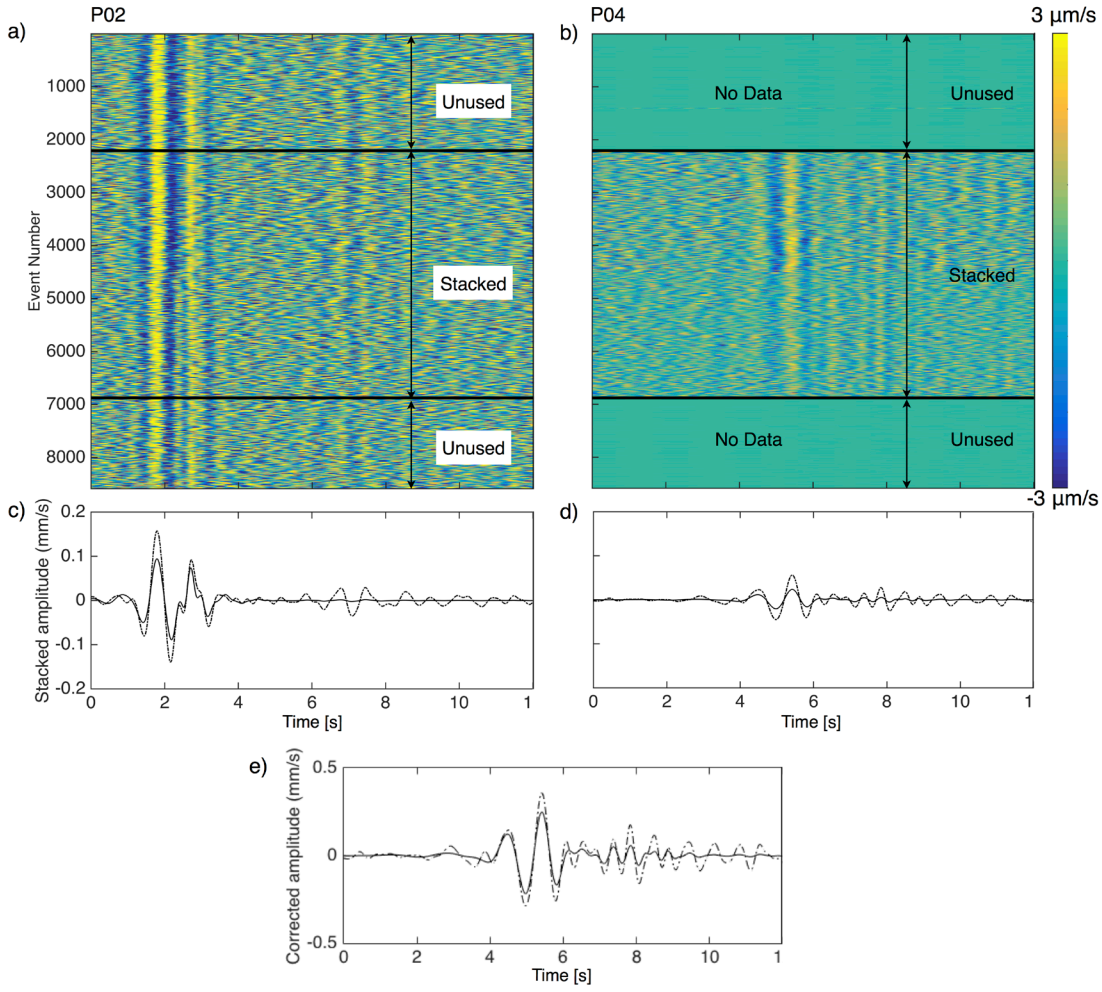

Figure 3.3. Stacking procedure with east components of P02 (a) and P04 (b). Black lines indicate the P04 stacking interval for P04. Waveforms are bandpass filtered between 0.5-2.0 Hz, and amplitudes are scaled appropriately to the color bar. Stacks of the east components of P02 (c) and P04 (d) are shown over the P04 stacking interval. Stacked P04 east component waveform (e) with amplitude normalized by the maximum absolute amplitude in (c).

We prepared the stacked waveforms for the full-waveform inversion by band-pass filtering 0.5-2 Hz with a zero-phase Butterworth filter. The data were also downsampled from 125 samples per seconds (sps) to 50 sps, trimmed and multiplied by a cosine tapered window centered on the highest amplitudes. Last, we transformed the data into the frequency domain.

3.3. LP inversion

3.3.1. Full-waveform inversion procedure

We followed an inversion approach that is similar to other studies (see e.g., Auger *et al.,* 2006; Waite *et al.,* 2008; Dawson *et al.*, 2011; Richardson and Waite, 2013) where the inversion is performed in the frequency domain to reduce the computation time and permit a grid search over a large volume. In this approach, the model moment tensor source time function is derived from the inverse Fourier transform of the inversion results at thousands of points within the three-dimensional (3D) model of the volcano. Following Lanza and Waite (Chapter 2), the inversion is initially unconstrained, meaning that the inversion is performed for different combinations of the 9 free parameters (six moment-tensor components and three single forces). The unconstrained, or 'free' inversion provides a spatial estimate of the location and its corresponding uncertainty. Constrained inversions at the best-fit centroid obtained from the free inversion are later performed as part of the nonlinear inversion procedure which involves a grid search over all possible moment tensor types and orientations.

For both free and constrained inversions, synthetic Green's functions were computed with the 3-D finite-difference method of Ohminato and Chouet (1997). We follow the same model parameterization as in Lanza and Waite (Chapter 2) where synthetic tests were carried out using the topography of Pacaya volcano. We used a cosine smoothing function to synthetize the Green's functions and assure stability. This wavelet has a time –constant period of one second to approximate the peak frequency of the LP events recorded at Pacaya volcano. The Green's functions convolved with the cosine function represent the elementary source time functions used in the inversion. We used a model that includes the 3-D topography of Pacaya, derived from a digital elevation map (DEM) from 2006 with a resolution of 10 m. The model domain is centered on the active summit crater of the volcano (Mackenney cone), and it has lateral dimensions of 4 km by 4 km and a vertical extend of 3.5 km. This yields a model with 401 x 401 x 351 nodes spaced 10 m apart. All station

locations were rounded to the nearest node, and topography was resampled to match the correct node grid. The node spacing does not violate the criterion of minimum number of grids per wavelength of 25 established by Ohminato and Chouet (1997). The model is also wide enough to minimize edge reflections of the boundaries while including all the stations. To find the best location for each of the point sources, we conducted a grid search over a volume of 740 m x 740 m x 500 m centered on the summit vent at a spacing of 20 m. In order to reduce the number of calculations required to derive the Green's functions, we followed Chouet *et al.* (2005), and used the reciprocal relation (Aki and Richards, 2002) between source and receiver in which each station is treated as a point source and each potential source as a receiver.

3.3.2. Nonlinear inversion procedure

We briefly summarize here the nonlinear inversion procedure, and we refer to Waite and Lanza (2016) and Lanza and Waite (Chapter 2) for a comprehensive description. The nonlinear inversion employs a grid search over all possible moment tensor types and orientations. For each model, the moment tensor is fixed using the method of Lagrange multipliers and the data fit are computed for each source type explored. The grid search uses the fundamental lune source-type definition of Tape and Tape (2012), in which each point is described by the spherical coordinates γ and δ, which are a function of the moment tensor eigenvalues. The longitude parameter, γ, ranges from -30° to 30°, while the latitude parameter, δ, ranges from -90° to 90°. The latitude δ is zero for deviatoric patterns, and both δ and γ are zero for double couple mechanisms. Because of the symmetry of the lune (the lower half of the lune is simply the opposite sign of the upper half), δ is evaluated only from 0 to 90°. The search over the lune space is performed using an even sampling of the moment tensor source type space, and the range of possible orientations of each moment tensor is explored by rotating the moment tensor at intervals using a sequence of three rotations about the initial coordinate system of the moment tensor (Waite and Lanza, 2016). As discussed in Lanza and Waite (2016), a 10° interval is deemed adequate as

tests with finer intervals showed that are no significant changes in the pattern ofmisfits. Given the large number of possible solutions, we performed the full grid search only for the best-fit location obtained from the unconstrained inversion.

3.3.3. Evaluation of the inversion results

The overall selection of the best solution was based on a weighted squared error between the observed and modeled data described as E_2 (Chouet *et al.,* 2003; Ohminato *et al.,* 1998):

$$E_2 = \frac{1}{N_r}\sum_{n=1}^{N_r}\left[\frac{\sum_{1}^{3}\sum_{p=1}^{N_s}\left(u_n^0(p\Delta t)-u_n^s(p\Delta t)\right)^2}{\sum_{1}^{3}\sum_{p=1}^{N_s}\left(u_n^0(p\Delta t)\right)^2}\right] \tag{3.1}$$

where $u_n^0(p\Delta t)$ is the pth sample of the nth data trace, $u_n^s(p\Delta t)$ is the pth sample of the nth synthetic trace, N_s is the number of samples in each trace, and N_r is the number of three-component receivers. Here the squared error is normalized by station, so that stations with varying amplitude contribute equally to the error. The use of misfit information here is not only employed to define uncertainty on the source centroid as a result of the free inversion, but also to examine the uncertainty in the moment tensor type.

For the free inversion results, the influence of the number of free parameters in each source model was evaluated by calculating the Akaike's information criterion (AIC) (Akaike, 1974), expressed as:

$$AIC = N_t N_s ln E_2 + 2N_m N_f \tag{3.2}$$

where E_2 is the squared error from equation (3.1), N_m is the number of source mechanisms, and N_f is the number of frequencies in the passband of interest. In general, the use of more free parameters is considered justified when both the squared error and AIC are reduced.

3.3.4. Evaluation of the velocity model

We considered a homogeneous velocity model with P-wave velocity of 978 m/s, S-wave velocity of 565 m/s and density of 1750 kg/m^3. These values represent the mean of the first 5 layers (first 130 m in depth) of the shear-wave velocity structure derived from Love and Rayleigh dispersion curves as in Lanza *et al.* (2016). While this homogenous model is not ideal, we did not have a detailed 3D model available. In order to evaluate how the limitations in the velocity model influence the solution, we performed synthetic tests that use a smooth 1D model. The 1D model follows the topography and is composed of 2 layers followed by a half space. The first layer extends until 100 m depth and we assigned P-velocity of 866 m/s, so that it will be lower than the homogeneous model in which V_P is set to 978 m/s. The second layer extends until 530 m, which is the maximum depth reached by the S- wave velocity model of Lanza *et al.* (2016). This layer has a P-velocity of 1.66 km/s obtained by averaging the V_P velocities of Lanza *et al.* (2016)'s model for layers encompassing the same depths. A P-wave velocity of 3.05 km/s was assigned to the half space. The S wave speed is fixed at Vp/√3. For each layer, the density was calculated averaging by depth the density values derived from the S- wave velocity model of Lanza *et al.* (2016), so that the first layer has a density of 1.99 g/cm^3, the second layer of 2.24 g/cm^3, and the half space of 2.56 g/cm^3.

We modeled synthetic data through the smooth 1D model at two depths below the vent using vertical cracks as the input mechanisms. We then inverted these synthetic waveforms using the Green's functions generated for the homogeneous velocity model. The resulting moment tensor source time functions have a shift in the source type from the initial input crack model towards a linear-vector dipole (LVD)

source mechanism. The values of E_2 are higher with respect to the misfits obtained with the homogenous model. On the other hand, the orientation of the reconstructed mechanism seems to be recovered quite well in both cases (Figure 3.4). These tests confirm an expected degradation of the accuracy of the solution related to the incorrect velocity model (Bean *et al.,* 2008). However, even with an incorrect velocity, which usually constitutes one of the major unknowns in source modeling studies, we can constrain the reconstructed source mechanism to a region of the lune that includes source types similar to the input source model.

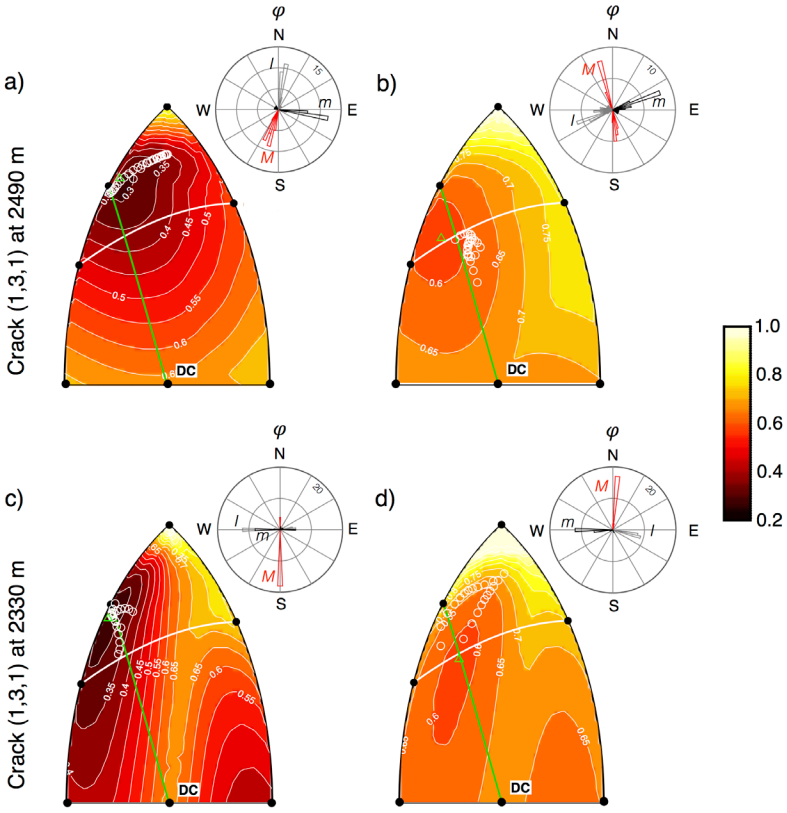

Figure 3.4. Error by fixed moment tensor solution, plotted together with the point-by-point mechanism type for the free inversion as white circles for a vertical crack input source models located at 2490 m, and 2330 m a.s.l. The green triangles indicate the γ - δ pairs with the minimum misfit. a) Solution for synthetic data generated with a homogeneous velocity model. b) Solution for synthetic data generated with a 1D velocity model. c) and d) same as a) and b) but for an input source located at 2330 m a.s.l. Rose diagrams show the orientations of the maximum, intermediate and minimum eigenvectors for the free inversion solutions.

3.4. Inversion Results

3.4.1. Free inversion results

Data were first inverted in the 0.5-2 Hz band without constraining the solution in any way. We solved for single forces alone (3-components), moment-tensor components alone (6-components) and a combination of both single forces and moment components (9-components). Because no constraints were used in the inversion, model source time functions can be inconsistent over time, resulting in a difficult to interpret, geologically unreasonable model. Therefore, we identified new best solutions by measuring the stability of the moment tensor throughout the source time function. For source nodes with E_2 within 5 % of the minimum, we calculated the consistency of the source time function over its duration using the standard deviations of the ratios of the eigenvalues. This measurement is expressed by a statistic called gamma by Matoza *et al.* (2015), and *g* by Waite and Lanza (2016) to avoid possible confusion with the previously defined moment tensor lune longitude. The parameter *g* is obtained by calculating the square root of the sum of the squared standard deviations of the ratios of the minimum to maximum and intermediate to maximum eigenvalues. We computed the ratio of eigenvalues at each point in the source time function having amplitude greater than 60% of the maximum to reduce the influence of noise in low-amplitudes. The solution with the lowest value of *g* within these error volumes is very similar to the source time function at the minimum E_2. Because the source time function is comparable and the minimum *g* (0.014) is close to the value of *g* calculated for the solution with the minimum E_2 (0.06), we chose to retain the E_2 min solution as the preferred source-fit centroid. The best-fit source centroids for minimum misfit, together with the g_{min} best-fit locations, and all the solutions within 5% of the minimum misfit, are shown in Figure 3.5. To note is that the absolute value of *g* is a function of the moment tensor eigenvalue ratios used in the calculation. For example, Waite and Lanza (2016), based on *a priori* information, used moment tensor eigenvalue ratios of 2:1:1 for examining *g* values for a source time function of a VLP signal recorded at Fuego volcano. However, they

demonstrated that, by considering different ratios, although the values for *g* vary, there was no difference in which solutions had the lowest *g*. We here examined *g* for ratios of 1:1:1, as no a priori knowledge on the source type is available. For the case of single forces only, the single forces are treated as the diagonal components of the moment tensor, and *g* was derived as before by computing the standards deviations of the ratios of the eigenvalues. This is reasonable as *g* is examined for ratios of 1:1:1.

Generally, source locations for all of the free inversion trials (3-, 6-, and 9-components) are mainly displaced from the summit either to the north for the 3-, 9-components and a local minimum of solutions for the 6-components, or to the east for the global minimum solution for the 6-components inversion. All reveal a shallow source location ranging from 20 m to 240 m below the highest topographical point (Figure 3.5).

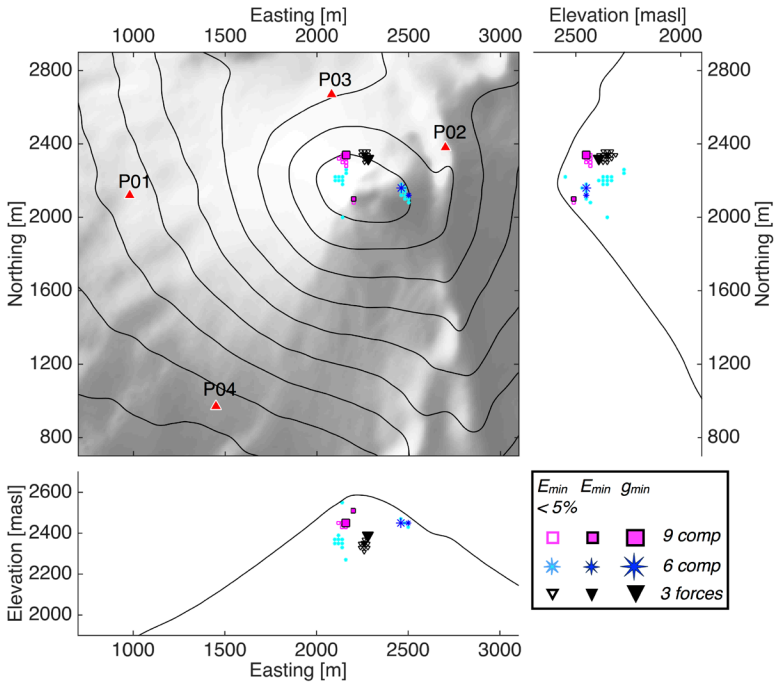

Figure 3.5. Locations of best-fit source centroids for minimum misfit (E_{min}), for all solutions within 5% of the minimum misfit ($E_{min} < 5$ %), and when both source time function stability and minimum misfit are considered (g_{min}). Locations for all three free inversion trials are shown. Contour interval is 100 m. Red triangles indicate the broadband network position.

We acknowledge here that a significant source of uncertainty is to be attributed to the poorly constrained homogeneous model used in the inversion. In addition to error in the mechanism type demonstrated above, the uncertainties seen in the location can be a result of a combination of errors in the velocity model and station distribution.

The best-fit model, based on both the residual error estimates and AIC, is the one that includes a combination of six moment-tensor components and three single forces. As seen in Table 3.1 the inversion result with the largest number of free parameters would appear to be the best statistically. However, the choice of the best source model has to take into account, not only an assessment of the overall misfits, but also an evaluation of whether the model is geologically reasonable. We explore interpretations of the single forces in terms of other observations of the events and previous work to determine if they are reasonable, or more likely a result of unmodeled structure in the model.

Table 3.1. Unconstrained inversion results from the case study example

	E_{2min} solutions						g_{min} solutions				
Inverted Parameters	E-W position relative to summit [m]	N-S position relative to summit [m]	Depth below topography [m]	E_2	**AIC**	Eigenvalue ratios	E-W position relative to summit [m]	N-S position relative to summit [m]	Depth below topography [m]	g	Eigenvalue ratios
3 forces + 6 moments	40 W	60 S	60	0.140	-7471.8	0.35, 0.45, 1	80 W	180 N	20	0.016	0.37, 0.43, 1
6 moments	260 E	40 S	40	0.323	-3871.4	0.20, 0.35, 1	220 E	0	40	0.014	0.23, 0.30, 1
3 forces	20 E	180 N	120	0.531	-2353.1	0.22, 0.13, 1	40 E	160 N	100	0.111	0.16, 0.09, 1

We attribute the LPs to strombolian bubble-burst events based on visual observations of the events as well as the infrasound records. We can then compare the amplitudes of the single forces to prior work on bubble ascent. Using the empirical scaling relation of James *et al.* (2009), in which the magnitude of the upward force is proportional to the square root of the slug mass, and the magnitude of our vertical single force of 1.08 GN, we estimated a slug mass of ~10^8 kg. Such a large value is unrealistic given the weak strombolian explosions and degassing activity observed at the summit. The size of the recorded infrasound events associated with the LPs and the short time scale of the oscillations, argue also against the presence of such strong vertical force as responsible of the type of mechanism. Furthermore, Dalton *et al.*

(2010) calculated that the mass of gas from discrete infrasound events recorded at Pacaya in 2008 were on the order of 12 to 962 kg. Their study was conducted during a period in which the style of summit activity was very similar to the 2013 activity. They found repeated events characteristic of strombolian explosions with peak amplitudes ranging from 0.17 to 2.61 Pa at 1 km, which are nearly the same as the range of 1.0 to 3 Pa at a similar distance.

Based on these considerations, we attribute the single forces in the 9-component solution to be related to complex, un-modeled velocity structure. This demonstrates how, while the moment tensor solution can be correct, errors in the velocity structure contaminate the single force terms, leading to spurious single forces whose physical interpretation is unreliable (Bean *et al.,* 2008). We therefore disregard the 9-components solution. As for the 3-component solution, in addition to fact that it has the worst fit, which is partially due to the smaller number of parameters used in the inversion, the single forces only inversion source time function components are not in phase indicating that the mechanism is not stable in time. The relatively high value of *g* with respect to the 9- and 6- component inversions also indicates a decrease in the stability of the moment tensor throughout the source-time function (Table 3.1). Therefore, we exclude this mechanism, and we attribute the most reasonable data fit to a 6-component mechanism. The best-fitting source for the 6-component inversion when both source time function stability and minimum misfit are considered is found to the ESE of the Mackenney cone at 2450 m above sea level, corresponding to about 40 m below the highest node in the topographical model in this location (Figure 3.5). While the epicenter of the source is displaced from the active vent, the shallow depth is consistent with the related infrasound and observed explosions.

Figure 3.6 shows the data (black) along with the synthetic waveforms. The free inversion synthetics, shown in red, generally fit the data fairly well. The synthetics from the fixed tensor solution, shown in cyan and described in the following section, have greater misfits, as expected for models with fewer free parameters. The source time function for the free inversion is shown in Figure 3.7a.

Note how the dipole components M_{xx} and M_{zz} are in phase and dominate the source time function. We used the general formulation convention with M_{xx} oriented East, M_{yy} North, and M_{zz} Up.

The source type is further analyzed through point-by-point eigenvector decomposition. We use only points with amplitude of at least 60% of the peak amplitude to assure stability. Figure 3.8 shows the statistics of the eigenvectors through rose diagrams of the azimuth φ (measured counterclockwise from the east direction), and inclination angle ϑ, measured from the vertical. For each point of the source-time history, we calculated the longitude γ and the latitude δ of the fundamental lune and the ratios of minimum and intermediate eigenvalues to the largest, whose median values are reported in Table 3.1. The eigenvector analysis and the point-by-point γ - δ pairs define a fairly constrained solution in the region that includes sources from a tension crack (white circles in Figure 3.7b) dipping ~40° to the east (φ = -6.4°). Although the network includes only four stations, they are well distributed. The solution behaves consistently through time, in agreement with the finding by Lanza and Waite (Chapter 2) that the azimuthal coverage has an important influence in the stability of the source time function compared to factors such as the number of stations used in the inversion.

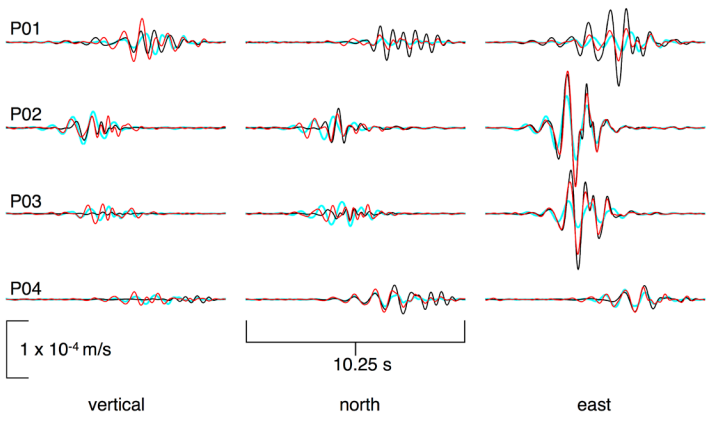

Figure 3.6. Waveform fits for the representative LP event obtained from the phase-weighted stacks of 8,587 repeating events. Fits are for the g_{min} solution for the 6-components free inversion. Red lines indicate free-inversion synthetics, cyan lines are best-fitting constrained inversion synthetics, and black lines represent observed velocity waveforms.

3.4.2. Constrained inversion results

The source time function derived from the free inversion was further investigated through a constrained inversion for source type. Figure 3.7b shows the misfits at each moment tensor type for the lowest misfit tensor orientation. That is, each point in the lune plot represents the lowest misfit value for all moment tensor orientations with the γ - δ pair. The misfits for the constrained inversion results are much larger than those of the free inversions, ranging from values of 0.64 to 0.84, with respect to the minimum value of 0.32 obtained from the unconstrained inversion. This is not unexpected given that there is essentially one model parameter in the constrained inversions, compared to six independent model parameters for the free inversions. The nonlinear inversion suggests a slightly larger area of possible source mechanisms types, however the region surrounding 5% above the minimum occupies an area of volumetric source type solutions. The ratio of eigenvalues (0.20, 0.42, 1) from the nonlinear inversion points to a source not precisely like a known theoretical source. It is somewhat like a theoretical tensile crack in a Poisson solid (1, 1, 3) in which the largest eigenvalue is perpendicular to the crack, but with less symmetry in the in-plane deformation. This is explored further below.

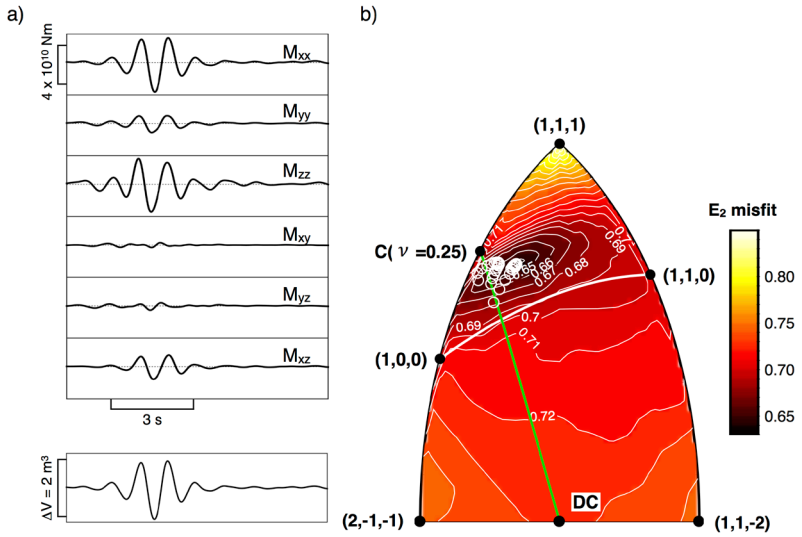

Figure 3.7. a) Source-time function from the 6- components free inversion. b) Error by fixed moment tensor solution, plotted together with the point-by-point mechanism type for the free inversion as white circles.

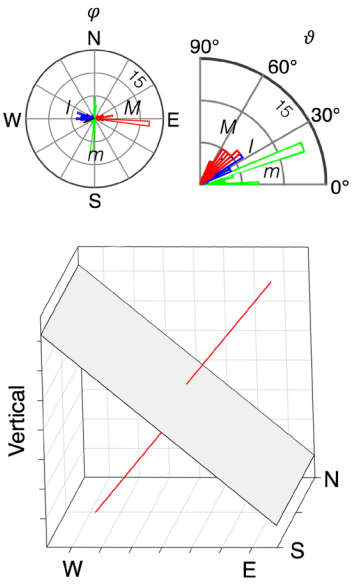

Figure 3.8. Eigenvector statistic for the free inversion solution obtained with 6 moment component sonly. The smallest (*m*), intermediate *(I*), and largest (*M*) eigenvectors are shown by green, blue, and red bins, respectively. The orientation of the crack plane and its normal (maximum eigenvector) are also shown in the xyz coordinate system.

3.5. Discussion

The LP events we recorded at Pacaya volcano in 2013 are associated with small explosive outgassing events at the summit. As previously described these events involve mass transfer on the order of 100s to 1000s of kg. Any single force associated with the ascent of these bubbles must be many orders of magnitude smaller than what we find with our 9 component free inversion. We examine this further by comparing other studies where single forces constitute an important part of the source time function. At Kilauea, Chouet *et al.* (2010) modeled VLP events as resulting from the ascent, expansion, and burst of a large slug of gas. They justified the presence of a dominant vertical single force as a result of an upward force on the Earth induced by the approaching of the slug to the surface and consequent pressure decrease and conduit deflation below the slug. The magnitudes of the vertical forces were

consistent with slug masses of 10^4 to 10^6 kg.

In another study, Richardson and Waite (2013) found that a dipping single force best-fit LPs associated with strombolian explosions at Villarrica volcano. In that case, the E-W oriented particle motions at all azimuths were attributed to near horizontal viscous forces associated with a structural feature in the upper conduit. There was little evidence for a volumetric component to the source time and therefore the moment tensor components were not required by the data. When we attempted to fit the Pacaya data with single forces only, we found that the particle motions were generally inconsistent; the data require a model with moment components.

An important limitation of this work is the small number of stations. We can clearly identify a dominant LP event, but questioned how reliably we could resolve the source mechanism. Synthetic tests described in Lanza and Waite (Chapter 2) have shown that a complete azimuthal coverage, with a maximum gap of about 130º, is desired for a higher resolution of the retrieved source time function. They also stated that azimuthal coverage has a larger influence on network performances over the number of stations used. However, for volumetric sources, four stations was deemed to be the limit of acceptable performances as with a lower number of stations the source mechanisms are unconstrained. Therefore, the case study of Pacaya where LP events were recorded by a network of only 4 stations with a fairly good azimuthal coverage should provide a reasonable model of the source mechanism.

As shown by additional synthetic tests described in this study, an unknown velocity model can introduce a further degradation of the solution. Although the source time function is constrained to a region of a volumetric source, the range of source-type shown in Figure 3.7 could reflect the affect of a scarcity of stations and of an incorrect velocity model.

With that in mind, we find that both the constrained and unconstrained inversions point to a source mechanism somewhat like a crack but with less symmetry. The nonlinear inversions indicate a range of possible solutions could fit the data reasonably well. The magnitude of the derived moment tensor is around 4 x

10^{10} Nm. This is comparable to moment tensor solutions obtained for low-amplitude LPs at other volcanoes. At Mount St. Helens, Matoza *et al.* (2015) inverted small LP events and found a moment tensor with amplitudes on the order of 10^{10} Nm. Small LP events have been also imaged at Popocatepetl, Mexico, and showed moment tensor components of similar order of magnitude (Arciniega–Ceballos *et al.,* 2012). In both cases the low-amplitude LP events were related to shallow crack mechanisms, and interpreted as hydrothermally driven fractures. At Pacaya, while the source mechanism is not precisely a theoretical crack, the finding of a volumetric source is consistent with a repetitive source that is associated with bubble bursts. We estimate the volume change in the source time function from the amplitude $(\lambda + 2\mu)\Delta V$, assuming $\nu = 1/4$ ($\lambda = \mu$) as the source-time function occupies a region along the arc with $\nu = 1/4$ in the fundamental lune (Figure 3.7). We use a shear modulus for the crack wall rock of 10 GPa following Lyons and Waite (2011)'s study at Fuego volcano. The calculated volume change is ~ 2 m^3. This value reflects the representative average event obtained from the stacked waveforms, and it is reasonable for the size of the events recorded. We used the relationship between excess pressure and volume change in a penny-shaped crack (equation 11 from Chouet *et al.,* 2010) to estimate the crack radius as ~ 1.14 m. We envision the crack not as an isolated feature, but as a component of the shallow conduit that responds to the passage of these bubbles.

A schematic of the proposed physical interpretation of the source of these small shallow long-period events is shown in Figure 3.9. As gas slugs rise toward the surface, they burst, creating an initial positive infrasonic pulse followed by a negative pulse. This generates the infrasound signal which was also observed in 2008 by Dalton *et al.,* 2010. Both LPs and the acoustic waves show compressional first motions, with LP signals preceding the infrasound by ~ 1 s. The timing and first motion help constrain the physical interpretation to one of two different processes. One possibility is that the non-destructive LP events are originating from the movement of the slugs (or bubbles) through a crack that inflates and deflates as a result of the passage of fluids; when the slugs (bubbles) reach the lava free surface,

they burst creating the infrasound signals. Given the short delay between the seismic and infrasound arrivals, the LP source must be very close to the surface. A second possible explanation is that the LPs are a manifestation of the reaction of the conduit to the expansion and ejection of the slugs (or bubbles). The pressure change at the lava surface generates an oscillatory response in the shallow segment of the conduit that, in turn, results in the generation of the LP events. The latter explanation invokes a simultaneous process. Indeed, we observe that the infrasound signal starts ramping up approximately at the same time as the LPs first arrivals (Figure 3.2). It is not clear whether the source is due to passage of bubbles through some constricted part of the upper conduit, or simply a reaction to the disturbance of the lava free surface by bubble bursts, or some other process. One thing that is clear, is that the continuous tremor-like signal we observed at Pacaya is dominated by this small repetitive source process.

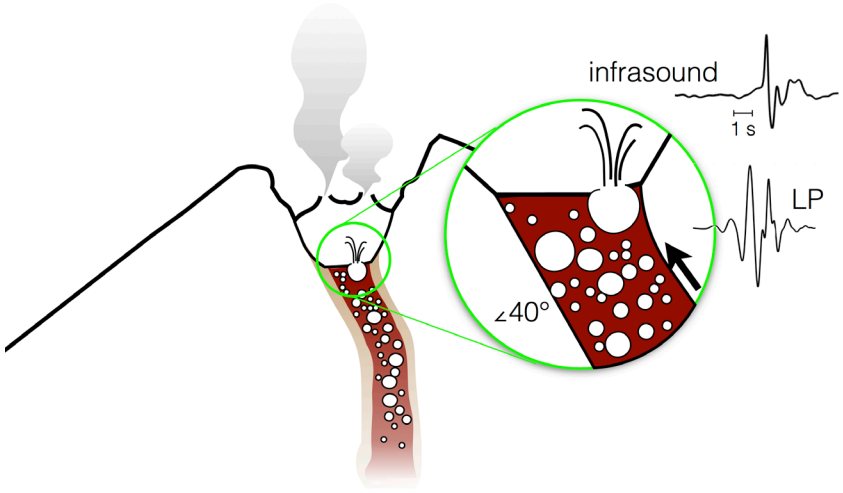

Figure 3.9. Schematic of the proposed interpretation of the source time function of the small long-period events recorded at Pacaya. Bubble bursting at the lava surface is likely at the origin of the infrasound signal. Pressure oscillations due to the bubbles rising or linked to consequent disturbances of the lava surface result into small LP events. The inclination of the shallow conduit reflects the orientation of the LP source.

3.6. Concluding remarks

We investigated the source mechanism and geometry of a class of LP events that includes thousands of small, repetitive, events that are associated with weak strombolian explosions at the summit vent of Pacaya volcano, Guatemala. LP events were recorded in October-November 2013 by four broadband stations located around the summit. Our modeling demonstrates that the LP events reflect a shallow crack-like mechanism most likely related to bubble-bursting events at the summit. Uncertainty in the velocity model and the small number of stations employed in the inversion allow for a certain degree of ambiguity in the source location, but we can clearly demonstrate that this event involves volume change in the source process. Tremor-like seismic signals dominate the records at Pacaya during much of the time. We show that the tremor is actually comprised in part by many small events, closely spaced in time.

Acknowledgments and Data

This work has been supported by the National Science Foundation career Award No. 1053794. The phase-weighted stacking code was provided by D. Mikesell. We thank J. Richardson for his guidance and fieldwork support. We are grateful to Parque Nacional Volcán de Pacaya for allowing access and permission to install seismometers. Data collected during the 2013 experiment are available through the IRIS Data Management Center. The facilities of the IRIS Consortium are supported by the National Science Foundation under Cooperative Agreement EAR-0552316 and by the Department of Energy National Nuclear Security Administration.

CHAPTER 4

Nonlinear inversion for 3D local earthquake tomography at Pacaya volcano, Guatemala[4]

[4] The material contained in this chapter is in preparation for submission to the *Journal of Volcanology and Geothermal Research.*

Abstract

The nonlinear inverse problem of 3D local earthquake tomography is typically accomplished using linear approximations. However, the inversion results and the associated reliability estimates obtained from linearized approaches are strongly dependent on the initial reference velocity model and other a priori constraints imposed by the modeler. In order to address the uncertainties and the non-uniqueness posed by the linear model estimation problem, the model space has to be sampled more effectively. In this study, we employ a nonlinear inversion technique based on a 'guided' Monte-Carlo method in which starting velocity models are randomly selected and, through simulating annealing, only a subset of models that satisfies acceptability criteria is retained. Synthetic reconstruction tests for checkerboard models demonstrate that the nonlinear inversion method is able to recover the synthetic anomalies within the limit of the resolution given by the posed problem. Because of the wider sampling of the solution space that can be achieved with the nonlinear inversion, this approach has the potential to increase our confidence level in the accuracy of the tomographic models. A data application example is carried out at Pacaya volcano, in Guatemala, where hundreds of local events were detected during a temporary seismic network installation in January 2015. Although limitations due to the quality and distribution of events in the dataset needs to be taken into account, we find that the range of acceptable models obtained with the nonlinear inversion shows some features comparable with the results from the linearized inversion, and provide confidence in the model. In both cases, the events are consistently relocated directly beneath the summit vent highlighting the presence of a straight conduit connecting the magma reservoir to the surface.

4.1. Introduction

The nonlinear inverse problem of three-dimensional (3D) local earthquake tomography (LET) is a widely employed technique for determining velocity structure, and many implementations of the method exists to simultaneously solve for velocity structure and earthquake hypocenter parameters (e.g., Thurber, 1986; Kissling, 1988; Thurber, 1993; Rawlinson *et al.,* 2010). While methods may differ in the treatment of the hypocenter-velocity coupling or in the technique for travel time and ray-path calculations, they all include linear approximations to the problem. As a consequence, the initial reference velocity model has a strong influence on the linear inversion results and on the reliability of the estimates of the model parameters (structure and hypocenters). The calculation of a minimum 1D model as the first step in the 3D modeling process is therefore highly recommended (Kissling *et al.,* 1994) and considered a key factor for reaching the convergence to an optimal solution, if one exists.

A number of studies have addressed these limitations of linearized inversion by implementing model space sampling methods, such as Monte-Carlo methods (e.g., Mosegaard and Tarantola, 1995). In addition to allowing for a broader sampling of the model space, an important advantage of Monte-Carlo inversions is that they can provide a range of acceptable models whose variability provides information about model uncertainty (Shapiro and Ritzwoller, 2002). On the other hand, the choice of the acceptance criterion is strongly subjective and problem-specific. Another limitation is the longer computation time involved in the random walk searches and multiple model runs. Despite this, Monte-Carlo type inversions can provide a powerful means to quantify uncertainties and identify features of the model that are worthy of interpretation (Lomax and Snieder, 1994; Shapiro and Ritzwoller, 2002). Monte-Carlo inversions have been applied with success to surface-wave tomography at local and global scale (Shapiro and Ritzwoller, 2002), and more in general to a wide range of geophysical inverse problems (see Sambridge and Mosegaard, 2002 for a comprehensive review).

In this study, we apply a nonlinear approach to both the initial search of the minimum 1D model and the subsequent 3D modeling. Following a procedure similar to that of Clarke *et al.* (2009), using the inversion algorithm **Velest** (Kissling *et al.,* 1994), we calculate a 1D P-wave velocity model through a sequence of inversions with each search beginning at a different randomly generated initial velocity model. Once a minimum 1D model is derived, we use a simulating annealing algorithm to explore the 3D solution space and randomly vary the starting velocity at each node of the 3D model grid. Comparisons between solutions are carried out in multiple steps by evaluating total residual errors, model variance, and by statistics performed at each node.

After performing tests with synthetic data, we test the capabilities of the nonlinear inversion at Pacaya volcano, in Guatemala. Pacaya is a 2552 m persistently active basaltic volcano characterized by strombolian style eruptions and occasional lava flows. An effort to learn about the velocity structure of the volcano was conducted by Lanza *et al.* (2016) where a 1D shallow shear-wave velocity model was produced from surface waves dispersion curves obtained from a small-aperture array analysis of the seismic tremor characteristic of the volcano. The study revealed low velocities for the upper 500 m, but was limited by the extent of the array. This paper constitutes the first attempt of producing a more complete image of the velocity structure of the volcano.

4.2. Seismic experiment and data selection

The seismic data used in this study were collected in January 2015 on and adjacent to Pacaya's active Mackenney cone. Much of the cone was constructed since 1961 through basaltic lava flows and accumulation of tephra (Rose *et al.,* 2013). During the 14 day 2015 campaign, Pacaya was in an open vent condition with continuous outgassing. Although the lava free surface was not visible from the summit incandescence was observed at night.

4.2.1. Temporary seismic network

We installed a temporary seismic network of 19 three-component, short-period sensors distributed between 100 and 1600 m from the active vent of Pacaya volcano. Station PS02 re-occupied a location from previous experiments and it was also outfitted with 3-element, equilateral triangular infrasound array, with ~30 m between elements. Another 3-element infrasound array was located at ~1 km north of the summit. Figure 4.1 shows the station locations indicated by red triangles, and the infrasound arrays, shown as black squares. Data were recorded on 19 Reftek 130 digitizers operating in continuous mode at 125 samples per second and equipped with Global Positioning Systems (GPS) timing.

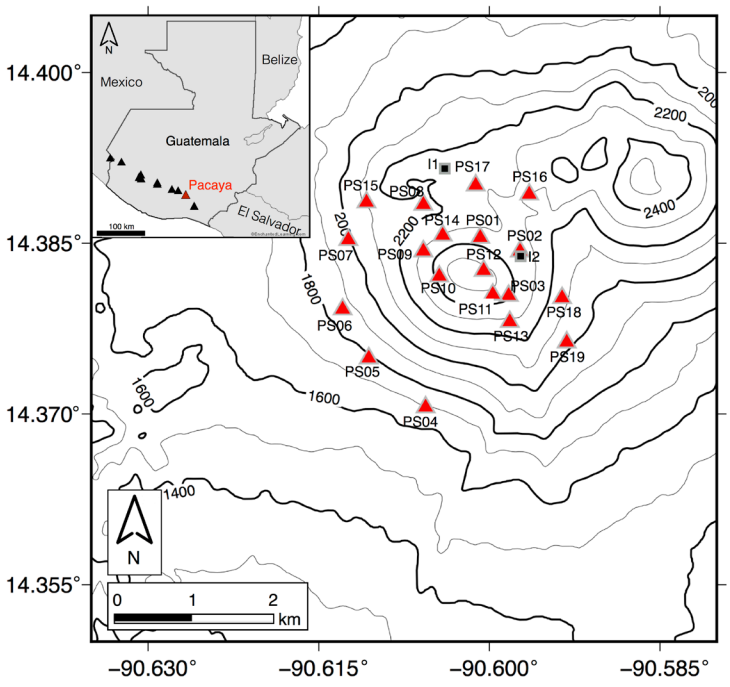

Figure 4.1. Station location map showing the 19 short-period stations (red triangles) and the 3-element infrasound arrays (black squares). Topography contour interval is 100 m. Inset in the upper left corner shows the location of Pacaya in Guatemala with respect to the Central American Volcanic Arc volcanoes marked as black triangles.

4.2.2. Earthquake data and selection

In addition to seismic tremor, ~1606 local seismic events were detected. These events were concentrated between 0 and 2000 m below the summit crater, but also included hundreds of events outside the seismic network. Spectral analysis revealed the presence of hybrid and high-frequency events with frequency peaks up to 10-12 Hz. The initial earthquake detection was obtained by using a Short Term Average/Long Term Average (STA/LTA) detection algorithm. Data were first bandpass filtered from 1 to 15 Hz and STA/LTA windows of 1 and 10 seconds were chosen respectively. Phase picking was then performed using the Antelope Environmental Monitoring Software package by BRTT (www.brtt.com/software). All phase picks were reviewed by hand before further processing and re-location. In LET problems, the only known variables are the receiver locations and the observed arrival times, so results are highly dependent on the data selection. Tomographic results are extremely sensitive to even a small number of bad data errors (Claerbout and Muir, 1973; Evans *et al.,* 1994); it is therefore important to restrict the analysis to include only well-picked events.

Our Pacaya dataset is particularly challenging to work with because of the presence of many events with emergent onsets. The source process of these events likely involves fluid pressure fluctuations in the magmatic conduit rather than brittle failure. Pick qualities were assigned values between 0 and 4, representing estimated errors of 0.06, 0.12, 0.30, 0.60, and > 0.60 s, respectively. The initial 1606 events resulted in 13,605 P-phase arrivals of which 372 (~2.7%) had pick quality of 0 (P0), 9852 (~72.4%) had pick quality of 1 (P1), 2189 (~16.1%) were assigned pick quality of 2 (P2), 533 (~3.9%) had quality of 3 (P3), and 659 (~4.9%) had pick quality of 4 (P4). Events with quality picks of 3 (0.60 s) and 4 (> 0.60 s) were immediately discarded and were not considered further on in the location and inversion applications. In order to assess the influence of analyst subjectivity in assigning pick errors, a subset of 10 events was randomly chosen, and it was separately hand-picked by four different users. Figure 4.2 shows an example of an event with a high level of

agreement between the users, and an example of low agreement, respectively. Low agreement situations were usually associated with picks that had higher estimated errors. Although the subjectivity test somewhat increased our confidence in the estimated pick errors, we conservatively further restricted the data to be selected to only include events that have more than 8 phase picks and whose pick qualities are equal or less than 2 with at least four picks with quality 0 or 1. This first quality cut reduced the number of earthquakes considered in the analysis from 1606 to 660.

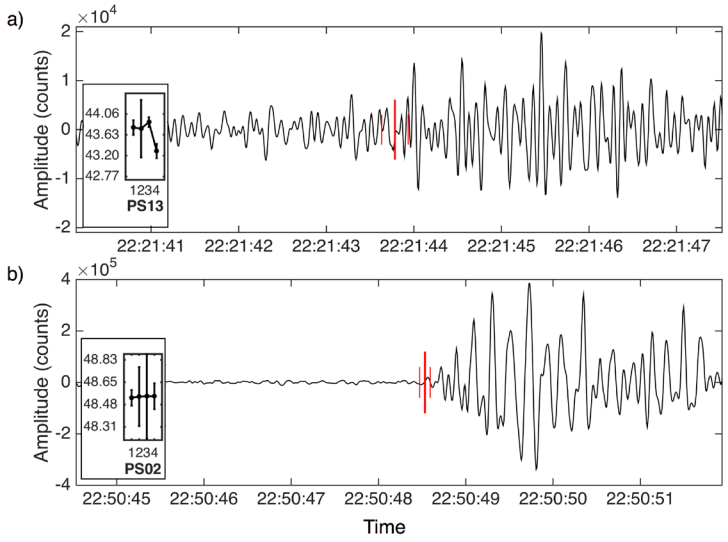

Figure 4.2. Pick quality control. a) Example of pick time with a low level of agreement between analysts at station PS13. The tall red line indicates the final pick with the correspondent uncertainties shown as thin red lines. Inset in the lower left corner shows, for each picker, the pick time with its error bar. b) Example of pick time with a high level of agreement at station PS02. Note that the range of the y-axis of the inset is 0.52 s in (b), whereas it reaches ~ 1.29 s in (a).

In order to further improve the phase arrival picks, we sought the presence of repeating earthquake with the aim to use clean stack of similar events for picking purposes and use in this way higher-quality arrival picks. We used REDPy (Repeating Earthquake Detector in Python) to investigate the presence of repeating earthquakes in the dataset (Hotovec-Ellis, 2016). In REDPy events are clustered into "families" via the OPTICS (Ordering Points To Identify the Clustering Structure) algorithm, with distance defined by cross-correlation. There is no requirement for

choosing a template event a priori. For consistency, we chose the same STA/LTA settings that we employed in Antelope. We identified seven families with more than five members and a cross-correlation threshold higher than 0.75. We then proceeded to stack the events of each cluster using the phase-weighted stacking technique (Schimmel and Paulssen, 1997; Thurber *et al.,* 2014). This produced waveforms with an improved signal to noise ratio, especially on those stations closer to the summit vent (Figure 4.3).

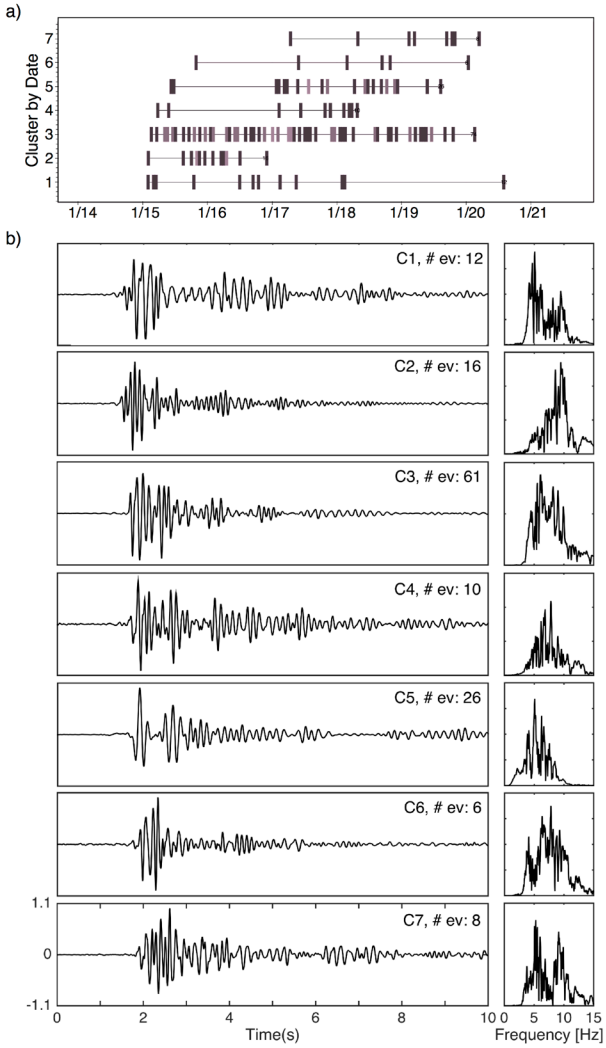

Figure 4.3. a) Time occurrence of families with more than five repeating events. Shades of gray indicate the number of events per hours, the more events occur in one hour, the lighter the color. b) Phase-weighted stacks of each family for station PS12, the closest station to the summit vent. Individual correspondent spectra are shown on the right of each trace. Note the high content in frequency, up to 10-12 Hz.

The stacks were then used for phase picking using the interactive picking environment **seis_pick** (Verdon J., 2011). This allowed higher quality picks than the ones one would have obtained from single events. After eliminating those events that belonged to a repeating family, and substituting those picks with the phase-weighted stacks, we had a total of 484 events.

Quality selection was further carried on based on azimuthal station gap distribution (< 240°), and root mean square (RMS) residual values (< 0.3) obtained after the first relocation–velocity inversion from Antelope through **Velest** (see section below). The final number of usable events in the inversion application was reduced to 259.

4.3. Methodology

We obtained the P-wave velocity structure for Pacaya volcano following a two-step procedure. First, we used the joint hypocenter-velocity model program **Velest** (Kissling *et al.,* 1994) to derive a starting 1D model that included P-wave velocities and station delays. We then used the derived minimum 1D model to solve for a 3D velocity structure using both a linearized and nonlinear approach. The linearized inversion was performed with the simultaneous inversion code **SIMULPS14T**, extended from **SIMULPS12** (Thurber, 1983; Eberthart-Phillips, 1990; Evans *et al.,* 1994) to include the option to use full 3D ray shooting (Haslinger and Kissling, 2001) and to account for 3D topography, so that no rays or earthquakes could be above the ground (Waite and Moran, 2009). Our nonlinear approach used the ray tracing and location algorithms in **SIMULPS14T**, but solved for velocity structure using a simulated annealing algorithm. Details of the implementations are given below.

4.3.1. Minimum 1D model

Given the non-linear nature of the hypocenter-velocity model problem, finding the absolute minimum model is strongly dependent on the initial starting velocity model (Kissling *et al.,* 1994). In order to reach a final model that represents the overall minimum misfit for the entire solution space and not solely a local minimum, it is necessary to approach this minimum model from various directions. We addressed this using a range of starting models with both high and low velocities following Clarke *et al.* (2009). Beginning with an initial location from Antelope, we carried out 1000 **Velest** inversions, each with a different, randomly chosen starting velocity model for the subset of 259 events. Layer boundaries were assigned fixed values of -1.1, 0, 1.5, 3, 5, 7, 12, 20, and 34 km in which higher definition (smaller depth spacing) was chosen for shallower depths in order to enhance the resolution at near-surface layers. The datum was shifted from sea level to 1500 m a.s.l. in order to keep all stations within the same layer, which is required by **Velest**, but at the same time, to have at least two layers within the volcano edifice. The value -1.1, once corrected for the datum is equal to 2.6 km a.s.l. For each starting model the shallowest layer velocity was randomly selected from a uniform distribution between 0.2 and 1.5 km/s while the second deepest layer velocity was randomly chosen from a uniform distribution between 2.0 and 5.0 km/s. All other velocities were randomly picked with the constraint that layer velocity always increased with depth, therefore not allowing the presence of low-velocity layers.

Although the input models have a wide range of velocities, the output models with the lowest 1 % of the total root-mean-square error (RMS) values are tightly constrained, particularly in the first two layers where most of the events are located. At greater depths, fewer rays pass through the layers, decreasing the resolution and the convergence between models. The minimum weighted RMS is equal to 0.115, which is inline with the average pick error of 0.134 seconds.

Because 3D variations are expected in the uppermost layers, we also inverted for station delays. The stations closest to the summit show negative delays

(seismically fast path) up to 0.4 s, while the farthest stations show positive delays (slow path) in the range of 0.6-0.8 s. These large variations indicate that the complex near-surface structure is being absorbed by the station corrections. As a likely effect of the station delays, the distribution of the hypocenters obtained by the best **Velest** model for the 259 events, is skewed to the NE with increasing depth from the summit. The velocity model with the minimum root-mean-square error (RMS), which was interpolated for the 3D starting model is shown in Figure 4.4.

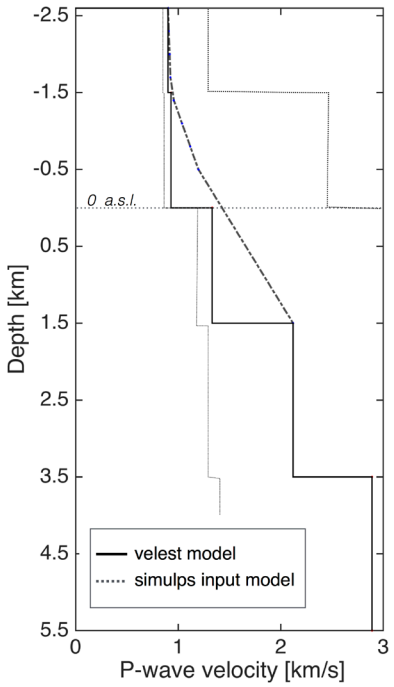

Figure 4.4. Minimum one-dimensional velocity model obtained with **Velest**. Light dashed lines represent the boundary of the range of models output from the 1000 inversions. Thick dashed line is the interpolated velocity model from which 3D models were derived.

4.3.2. Linearized LET inversion and initial model parameters

The 259 events located using the minimum 1D model were re-examined for quality. We sorted the data by RMS and selected only events with RMS < 0.15 and individual pick residuals < 0.10. This left 178 earthquakes with 1,979 P-wave arrival

times for the 3D LET inversions. The grid spacing used for the tomographic reconstruction was chosen taking into account the distribution of the earthquake hypocenters and the receiver geometry. The 3D grid is centered on the summit of Pacaya volcano, it has lateral dimensions of 5 km x 5 km and it extends up to 1.5 km below sea level vertically. The spacing between nodes is not uniform, but increases away from the vent. A spacing of 200 m was deemed appropriated for an area within 600 m of the vent, where most of the events and stations are and where most of the ray paths cross. Layer thickness also increases with depth to allow for a higher resolution at near-surface depths.

We interpolated the minimum 1D model obtained from **Velest** across additional layers that were added to increase the sampling for shallow layers where most of the earthquakes are located (Figure 4.4). The datum was kept the same as the one used in the search of the minimum model. In this interpolated 3D starting model the velocities in nodes located above the topography were fixed at 0.33 km/s.

One of the critical aspects of the linearized inversion is the choice of the damping. We empirically explored a wide range of damping values by running a series of single-iteration inversions with different damping values. The trade-off curve of the data misfit and model variance obtained for these test runs shows that the inversion is not behaving consistently for damping values of 0.5 and lower. We chose a value of 5, which is a good compromise between a too smooth model (small data variance) and a too complex model that would fit noise in the data (large model variance). This choice was validated with synthetic tests, described below.

Initial linearized inversions tests demonstrated that by decreasing the number of events, there was little effect on the resulting velocity structure. This is ascribable to the fact that the events are clustering in a small area, and therefore they share similar travel paths to the receivers. As a result, we chose to decrease the number of earthquakes in favor of better data quality, and reduced the earthquakes used in the 3D inversion to 123 by discarding events that were located above the topography due to failure of the shooting method and those events that had RMS residual above 0.20

after a first linearized inversion run. All the station correction terms were set to zero and damped, since, as shown by the results from **Velest**, they tend to absorb most of the near surface structure.

4.3.3. Nonlinear LET inversion

Because of the additional challenge of limited event distribution and the difficulty in picking events, we employed a nonlinear inversion approach that uses a simulated annealing (SA) algorithm to explore a wider sample of the solution space. One of the valuable properties of SA algorithms is that, due to its random nature, it minimizes the risk of getting trapped in a local minimum. The technique of simulated annealing considers the objective function of a minimization problem as an equivalent energy function of an illusory annealing of a solid (Kirkpatrick *et al.,* 1983). The term "annealing" refers to a cooling process in which a liquid is brought back to a perfect crystallized state by slowly decreasing the initial temperature. Such organized solid state represents the global minimum of the energy function.

Typically, in SA optimization algorithms, each model realization is generated as a random perturbation to the previous model in which the randomness of the searching process is controlled by a statistical parameter, usually called temperature (T) to maintain the analogy to the annealing of solids. At first, for high values of T, the search is performed totally at random, and then, as T decreases, the search becomes more and more directive to a state of minimal internal energy. This is similar to a 'guided' Monte-Carlo technique. The choice of the initial temperature and the rate at which the temperature is going to be decreased (i.e., the cooling schedule) represent the two most important factors for the success of the algorithm. Both parameters are problem-dependent and they are usually determined by a trial and error procedure, if a priori information is not available. We therefore performed multiple tests to properly tune the algorithm. The tests involved simulations with three different cooling schedules; a logarithmic, geometric and exponential schedule were considered. For each cooling schedule, we varied the cooling speed parameter

α within a range of values comprises between 0.5 and 1. In general, the most typical values for α are between 0.8 and 0.99. The maximum number of iterations allowed was also varied between 100 and 1000. We observed that a logarithmic schedule was extremely slow, and convergence was not reached after 1000 iterations, with the algorithm still moving randomly through the model space. The best performances of the algorithm in terms of cooling rate were instead obtained when a geometric schedule was used. A geometric schedule is expressed as:

$$T_n = \alpha^n T_0 \qquad (4.1)$$

where T_n is the value of the temperature at iteration *n,* T_0 is the initial temperature and α is the cooling speed parameter. This schedule allowed for a slow enough cooling rate that permitted to reach a minimum solution within ~ 80 iterations in an acceptable computational time. T_0 was chosen to be equal to 1 after tests with lower values showed a lost in the global character of the search as the search area became restricted around the starting point. Higher values did not show significant differences in the performance.

A proper search is characterized by a higher degree of randomness at the beginning of the search, followed by convergence to a minimum. This condition was reached by choosing a value of α equal to 0.9. Higher and lower values of α produced either perpetual randomness or too rapid of a convergence, where the solution space was not properly sampled.

Once we established the cooling schedule, and chose the initial temperature, we started the iterative procedure by using the minimum 1D model obtained from **Velest** (the initial model) to re-locate the 123 best events remaining after running the final quality selection on the results obtained from the initial linearized tests. Relocation of the events was derived using **SIMULPS** with the option for the inversion of the velocity switched off. Then, at each iteration, we randomly perturbed the velocity model, computed a new 3D model, re-located the earthquakes and used the Metropolis-Hasting criterion for determining if the new solution was going to be carried on to the next iteration or it was going to be discarded (Metropolis *et al.,*

1953). Following the analogy with the annealing of solids, the acceptance criterion is expressed in terms of "energy variation" (ΔE). Here ΔE is computed by subtracting the value of the events RMS from the initial model to the RMS value obtained from the updated model:

$$\Delta E = E(m_n) - E(m_{n-1}) \qquad (4.2)$$

where $E(m_n)$ is the RMS value of the updated model, and $E(m_{n-1})$ is the RMS of the initial (or previous) model. Then, if $\Delta E < 0$ the updated model m_n is always accepted; but if $\Delta E \geq 0$ the updated model is accepted with probability:

$$P(\Delta E) = \exp\left(-\frac{\Delta E}{T}\right) \qquad (4.3)$$

where T is the temperature. The criterion allows for a preference for any model when T is high, while, as T decreases, only models for which ΔE is small will have a substantial chance of occurrence. If the updated model is not accepted, the new iteration will proceed with the same model of the current iteration. A schematic of the procedure is shown in Figure 4.5.

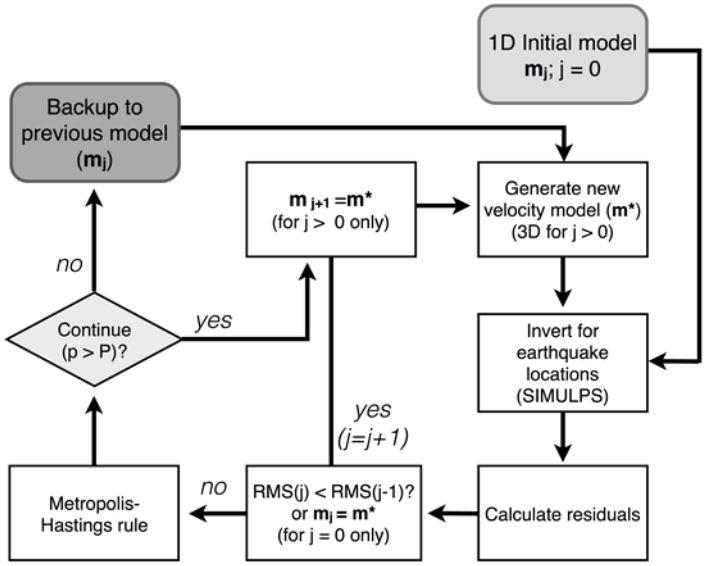

Figure 4.5. Schematic showing nonlinear inversion iterative procedure.

The model perturbations were computed at random, using a Gaussian distribution with standard deviation of 0.05 and mean set to the current model velocity. Since each node was perturbed individually, the resulting model was often extremely rough. Therefore, we applied a Gaussian smoothing function to the model before the re-location of the hypocenters. The horizontal dimensions of the Gaussian convolution kernel were set to be 3 x 3, the vertical extent was fixed at 1, and the standard deviation was set equal to 0.65. Multiple model runs were conducted in parallel in order to increase the randomness and solution space sampling.

The other model parameters used in the linear inversion such as grid spacing, earthquake dataset, and initial velocity model were kept the same in the nonlinear inversion in order to allow for later comparisons between the solutions obtained from the two approaches.

4.3.4. Model Resolution

Model resolution is typically assessed using synthetic reconstruction or checkerboard type tests along with other quantitative measures. For the linearized inversion, model quality was assessed by considering the diagonal and spread of the model resolution matrix. Since we do not have access to a resolution matrix for the nonlinear inversions, for each iteration, we evaluated the total residual error. For the final models of each random walk search, we performed statistics (mean, standard deviation) at each of the most sampled nodes. The calculation of the variances is performed only on models that have a final RMS less than an arbitrary RMS threshold. We interpret model grid nodes that have low variance across multiple nonlinear models to be relatively more reliable than those with large variance. Taken together, the tests point to those regions where anomalies are required by the data, and those areas where anomalies are not resolved.

We first describe inversions of a synthetic, noise-free, checkerboard test performed using both methods (Figure 4.6). In this case, the starting anomalies have a

lateral extent of 400 m in the center of the model space (equivalent to 2 grid nodes in each direction), and a vertical extent that also encompasses 2 grid nodes equivalent to 600 m in depth for the shallower layers. Since the grid is not uniform across the model space, the size of the anomalies increases far away from the center of the model and at higher depths. Gaps were left between anomalies to highlight any trade-off between neighboring anomalies. As shown in Figure 4.6a, for the linear inversion, the anomalies are fairly well recovered for the first 900 m, but at larger depths, the resolution decreases due to the scarce ray coverage. The gaps between the anomalies suffer some smearing and they are not always well defined.

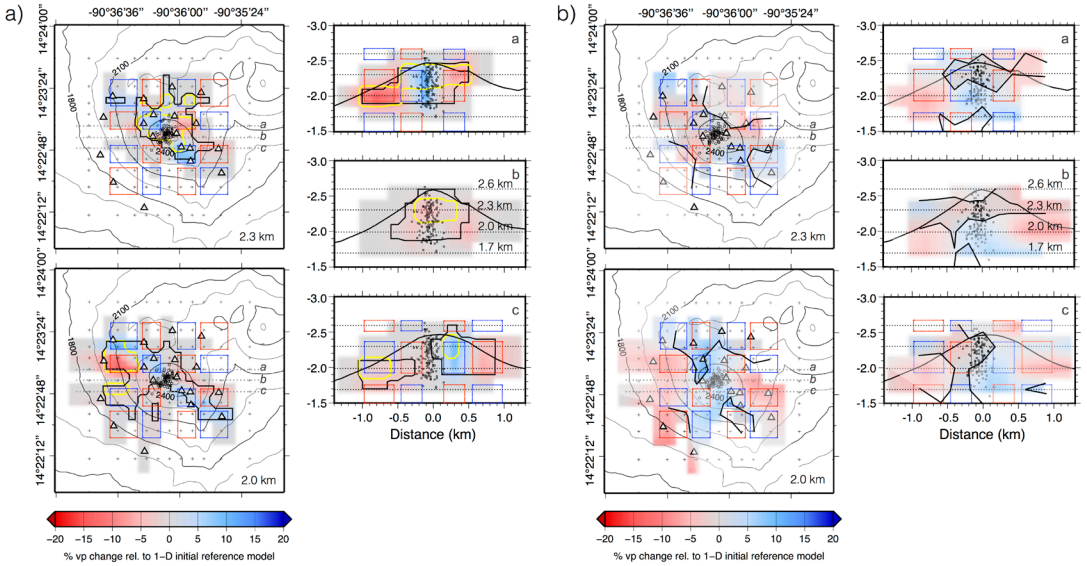

Figure 4.6. Horizontal and vertical slices through a synthetic checkerboard test model derived from the linearized inversion (a) and nonlinear inversion (b). In both (a) and (b) the input synthetic anomalies are outlined with red and blue boxes, the node positions are plotted with black crosses, stations are plotted as triangles, and dotted lines marked with letters *a, b*, and *c* indicate the profile sections of the vertical slices. Topography contour interval is 150 m. In (a) black lines outline regions with spread values less than 0.7, whereas yellow lines represent the diagonal element of the resolution matrix with values less than 0.1. In (b) black lines outline areas with variance across the 8 models with RMS below 0.0585 seconds, that is less than 0.0016 km^2 s^{-2}. The plots are faded were the variance has higher values.

Similarly, for the nonlinear case, the anomalies are well recovered where the variance across multiple models is low. For the synthetic tests we performed 20 different random walk searches, 8 of these resulted in a RMS values below the chosen cutoff of 0.0585 seconds. The checkerboard tests demonstrate that the nonlinear inversion method is able to reconstruct fairly well the synthetic anomalies in the limit of the resolution given by the posed problem. In the case of Pacaya, the velocity structure can be resolved only for the first 900 m due to the clustered distribution of the events in the upper cone.

4.4. Inversion Results

The synthetic results suggest model resolution is reasonably good in the upper part of the cone. We next compare the results from the nonlinear and linearized approaches using real data. Data errors results in more diversity between the models produced using the two methods, but results are consistent in some areas.

4.4.1. Linearized inversion results

Map views for depths of 2.3 and 2.0 km a.s.l. and latitude sections spaced 200 m apart in both south and north direction, are shown in Figure 4.7. The color scale indicates velocity changes with respect to the initial **Velest** minimum 1D model. We observe a root mean square residual reduction of 12.76% from an initial weighted RMS of 0.12 seconds. This reduction is accompanied by variations in the earthquake locations with respect to the results obtained with the 1D model. Indeed, most of the events are relocated directly below the summit vent; all the events are within the volcanic cone. As a consequence of this clustered distribution, resolution of the tomography results is limited to the first upper 900 m.

A dominant feature of the model is the presence of a fast area high in the cone. A possible explanation of this fast anomaly can be found in the station corrections. In the 1D model the summit area is characterized by high negative

delays, as a result, once the delays are reset to zero in the 3D modeling, the near-surface structure that was absorbed by the station delays shows as a fast region with respect to the initial model. The area northwest of the summit shows up as a fast anomaly as well. This seems to be a robust feature as it is also present in the nonlinear inversion results where the model is considered to have high resolution (see section below). However, interpretation of the anomalies is somewhat limited by the error in the data.

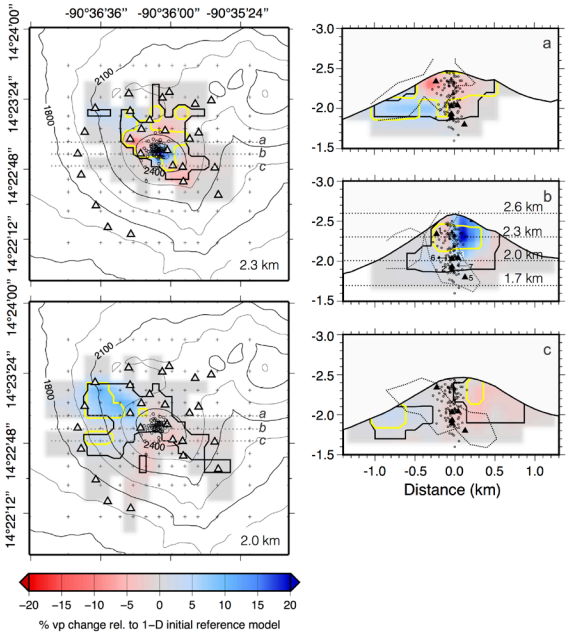

Figure 4.7. Horizontal and vertical slices through the linearized inversion model. Color scale indicates percent deviations from the 1D starting model shown in Figure 4.4. Black lines outline regions with spread values less than 0.7, whereas yellow contours define areas with diagonal element of the resolution matrix less than 0.1. Dotted lines in the vertical slices define the contour variance at 0.0016 $km^2 s^{-2}$ from the nonlinear inversion acceptable models. Earthquakes are plotted as black circles with black triangles representing the phase-weighted stacks of six repeating families. In the map views, stations are plotted as gray triangles, and node positions are plotted as crosses. Topography contour interval is 150 m.

4.4.2. Nonlinear inversion results

The same model slices are shown in Figure 8 for the nonlinear inversions. In this case we carried out 50 individual random walk searches, 14 of which resulted in a

final RMS value less than 0.102 seconds, which was chosen as RMS threshold. We reached a maximum RMS reduction of 15.2%, comparable with the one obtained for the linearized inversion. In all 14 acceptable models, similarly to the results from the linearized inversion, the events re-located in a cluster in the first few hundreds meters below the summit vent. In order to highlight well-resolved areas, we calculated, for each node the variance across the 14 minimum RMS models. Based on the synthetic tests, we chose a value of 0.0016 $km^2 s^{-2}$ (standard deviation of 40 m/s) as a threshold to distinguish well resolved from poor resolved areas (Figure 4.8). The fast anomaly seen in the linearized case is now located in a region of high variance across the models, and in the model with the lowest RMS shown in Figure 8 is non-existent. As previously mentioned, the area to the northwest shows a fast anomaly in agreement with the linearized results.

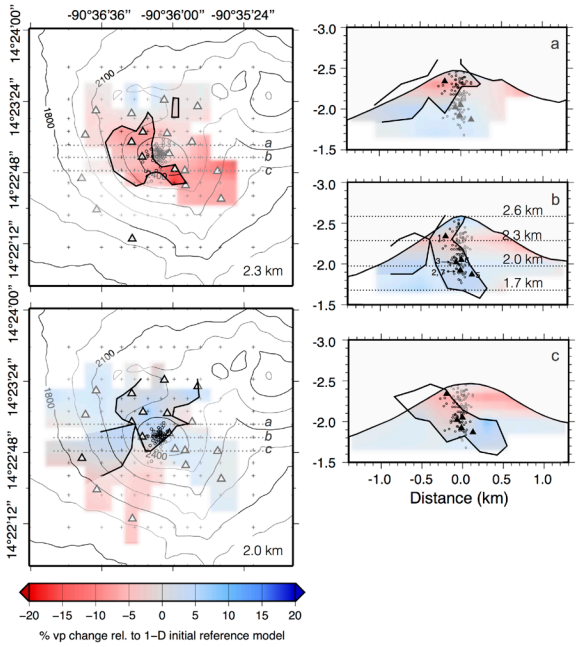

Figure 4.8. Horizontal and vertical slices through the nonlinear inversion model. The color scale indicates percent deviations from the 1D starting model shown in Figure 4.4. Black lines outline regions with variance across the 14 acceptable models less than 0.0016 $km^2 s^{-2}$. Faded areas indicate areas with variance values higher than 0.0016 $km^2 s^{-2}$. Earthquakes are plotted as black circles with black triangles representing the phase-weighted stacks of six repeating families. In the map views stations are plotted as gray triangles, and node positions are plotted as crosses. Topography contour interval is 150 m.

In addition, we observe that the events are in slightly different locations across the chosen acceptable models. The variations seen in the models, even in those regions where crossing rays are abundant, can partially be attributed to earthquakes wandering from model to model. Figure 4.9 tracks in space the distribution of six phase-weighted stacked events across the 14 models showing variations of 200 to 400 m in all directions. These become significant when the scale of the features to resolve is of the same order of magnitude.

In summary, although the interpretation is very limited, in areas of low variance, the nonlinear inversion presents similar characteristics of the linearized case making the nonlinear inversion a feasible approach. Moreover, perhaps the most striking similarity between the linearized and nonlinear inversion models is the location of the events. Both 3D velocity models produce a straight pattern below the summit vent of Pacaya, extending until about 900 m in depth. This points most likely to the presence of a straight conduit connecting the magma reservoir to the surface.

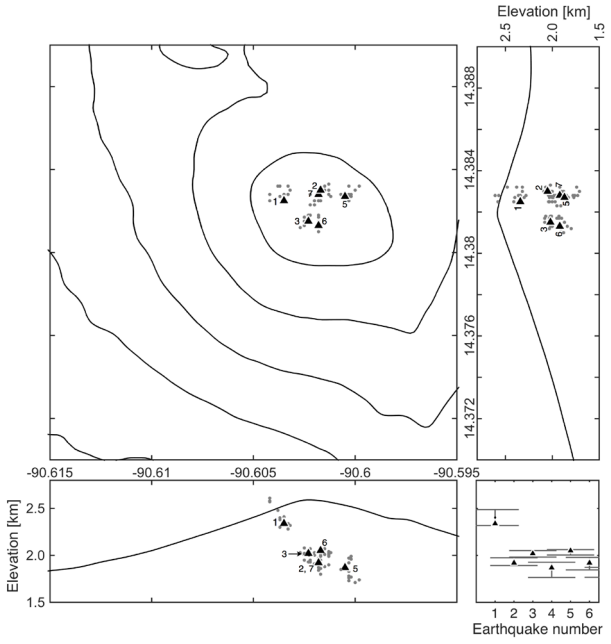

Figure 4.9. Spatial variations of six phase-weighted stacked events across the 14 acceptable models. Triangles indicate the locations of the model with the lowest RMS, this is the model also represented in Figure 4.8. The lower right corner shows error bars relative to depth uncertainties of the six events.

4.5. Conclusions

We obtained P-wave velocity structure models for Pacaya volcano, Guatemala, using both the widely known linearized local earthquake tomography approach and a 'guided' Monte-Carlo nonlinear inversion technique. While the nonlinear inversion requires almost an order of magnitude more computational time and the tuning of the optimization algorithms for the random walk searches is problem-dependent, it has the advantage to explore a wider sample of the solution space, does not require choosing a damping value and it is not strongly dependent on the initial velocity model. These advantages make nonlinear inversions for local earthquake tomography a powerful alternative to linearized approaches. Synthetic reconstructions for checkerboard models show that the nonlinear inversion applied to LET has the capability to recover the synthetic input anomalies in within the limitation given by the case problem, similarly to the linearized case.

Although the dataset collected at Pacaya volcano had some limitations related to spatial distribution and quality of first arrivals picks, and it didn't allow for an in depth interpretation of the velocity structure, we successfully test the nonlinear approach as a valuable alternative to more common linearized techniques. The case study also shows the importance of a 3D model for properly re-locating events, especially when high station corrections tend to absorb the near-surface structure.

Acknowledgments and Data

This work has been supported by the National Science Foundation Award No. 1053794. We thank Kyle Brill, Hans Lechner, Chet Hopp, Max Guettinguer, and Carlo Prandi for fieldwork support. We are grateful to Parque Nacional Volcán de Pacaya for allowing access and permission to install seismometers. Data collected during the 2015 experiment are available through the IRIS Data Management Center. The facilities of the IRIS Consortium are supported by the National Science Foundation under Cooperative Agreement EAR-0552316 and by the Department of

Energy National Nuclear Security Administration.

Summary

In this study we introduced nonlinear inversion strategies for both source characterization of volcanic seismic signals and for 3D local earthquake tomography (LET). Data applications of both techniques are carried out at Pacaya volcano, Guatemala.

Chapter 1 shows the importance of using ambient noise recorded on small arrays for deriving a shallow velocity model. Knowledge of the near- surface heterogeneous layering and compositional variety characteristic of young volcanic cones is indeed critical for constraining various seismic analyses, from computing source mechanisms of shallow volcanic events, to producing tomographic images of the shallow magmatic system. At Pacaya, because the individual events were difficult to pick out, using ambient noise on a small array provided a means to determine the shallow velocity structure beneath it.

With a velocity model in hand, the nonlinear inversion for source type presented in Chapters 2 and 3 allows us to search through all possible moment tensor solutions, providing quantitative constraints on the source time function resolution and uncertainty. This facilitates the interpretation of mechanism types especially when limited resources and observational data are available, a common situation found in volcanic environments. Synthetic analysis of different network configurations shows that a degradation in resolution and geometry on the moment tensor solutions is expected when azimuthal instrument coverage has gap greater than 130°. Constrained and stable source-time functions are obtained when more than 8 stations are considered, but no significant improvements are reached by employing more than 16 stations. With a lower number of stations, the resolution of the recovered source time function is dependent on the source type, with lower uncertainties associated with source mechanisms with a higher volumetric component. Using only 4 stations, the inversion of thousands of small LP events at Pacaya volcano, Guatemala, shows a certain degree of ambiguity in both the source location and type to be attributed to uncertainties in the velocity model and the small

number of stations employed. Despite this, the moment tensor solution is found to be fairly well constrained and it reflects a shallow crack-like mechanism most likely related to bubble-bursting events at the summit. This small repetitive source process is likely to dominate the continuous tremor-like signal that usually characterizes the seismic records at Pacaya.

The sensitivity analysis for moment tensor solutions carried out in Chapter 2 and Chapter 3 demonstrates that a minimum number of 4 stations are necessary to adequately constrain the moment tensor. While Chapter 1 showed that small aperture arrays are powerful tools to derive information on the shallow velocity structure beneath them, an accurate velocity model of the entire edifice is critical for constraining seismic analysis, such as earthquake locations. Combining the results from the two studies, we suggest that best practices for network design on volcanoes could involve arrays of arrays to get both an adequate azimuthal coverage and a better handle of the complex shallow velocity structure beneath volcanoes.

The derivation of a velocity structure is further investigated in Chapter 4, where the proposed 'guided' Monte Carlo nonlinear inversion approach for LET problems allows us to better sample the solution space. Synthetic checkerboard tests show that the nonlinear inversion has a promising capability to recover velocity anomalies within the limitation given by the case problem, similarly to the linearized inversions. The data application performed at Pacaya volcano had limitations related to spatial distribution and quality of first arrival picks, and it didn't allow for an in depth interpretation of the velocity structure. However, similar features were recognized across both the linearized and nonlinear models showing very low P-wave velocities, on the order of 900-950 m/s, in the upper cone. Moreover, the case study shows that 3D velocity models are necessary to properly locate events when high station corrections tend to absorb near-surface structure. Indeed, the earthquakes relocate directly below the summit vent, possibly indicating a straight conduit connecting a shallow magma reservoir. With higher quality earthquake data we foresee this technique to be a valuable alternative to the widely applied linearized approaches.

Appendix A

Included within these supplementary materials are figures which demonstrate aspects of the model uncertainties and inversion procedure described within the Chapter 1. Supplementary Figure A1 shows an example of the dependence of the results on the starting model, and shows the results of different inversions obtained with different starting parameters. Supplementary Figure shows the effects of changes in the initial V_P/V_S ratio on the retrieved velocity structures. All the models have comparable fits to the dispersion data, indicating that Rayleigh wave and Love wave velocities are more dependent on the shear velocity structure rather than on density and Poisson ratio.

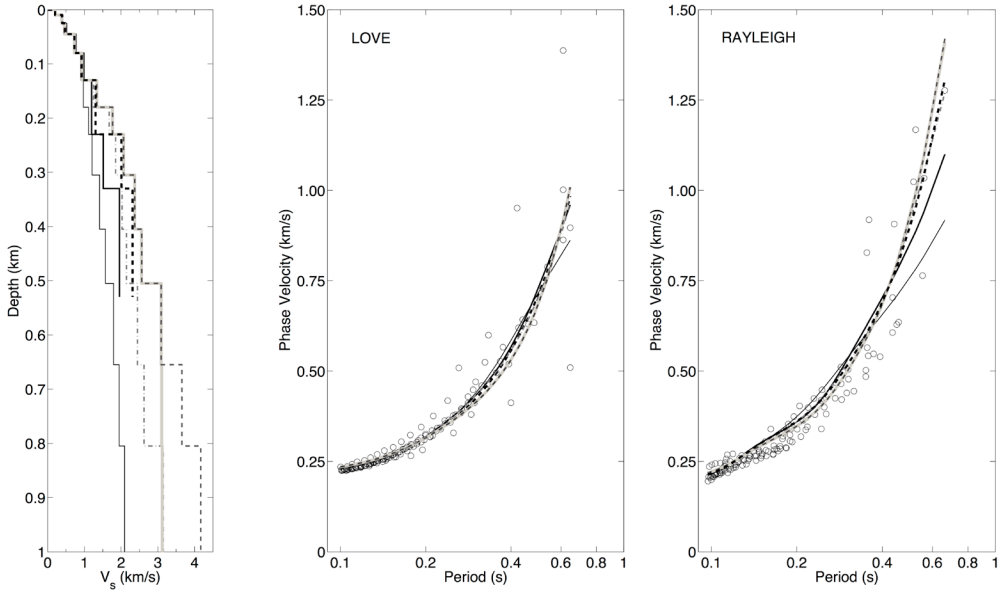

Figure A1. Examples of some of the estimate of the shear-wave velocity models obtained from inversions for Rayleigh and Love wave dispersion curves using different number of layers, thickness of layers, and starting velocities. Open circles represent the phase velocity data obtained from the zero-crossings, maxima, and minima of the correlation functions for the 7 distinct radii. Individual curves are the best-fitting phase velocity curves for each model considered.

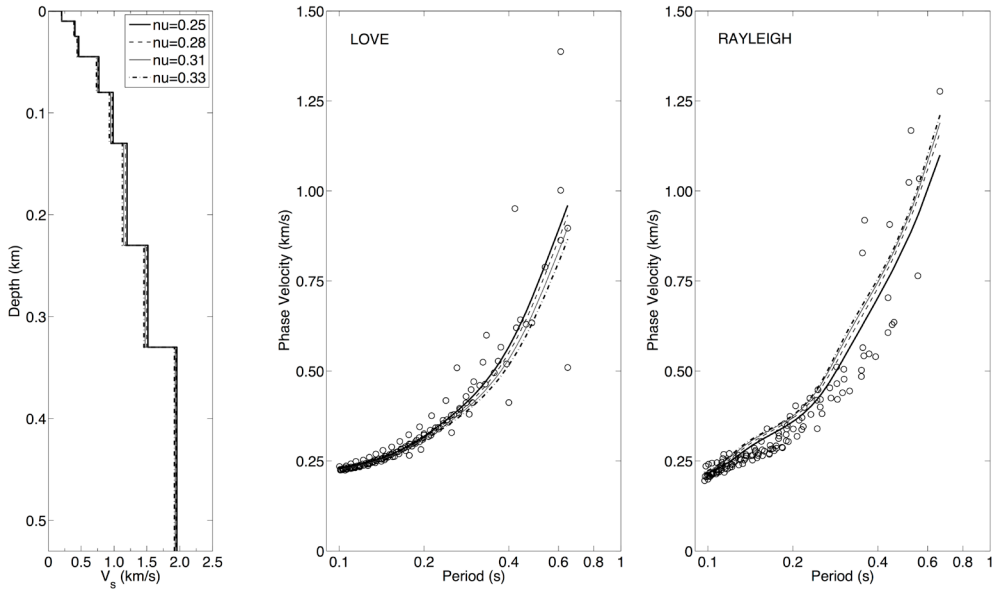

Figure A2. Estimate of the shear-wave velocity models obtained from inversions for Rayleigh and Love wave dispersion curves using different initial Poisson ratios (nu). The thick solid line corresponds to the model with the minimum misfit to the dispersion curves. Open circles represent the phase velocity data obtained from the zero-crossings, maxima, and minima of the correlation functions for the 7 distinct radii. Individual curves are the best-fitting phase velocity curves for each model considered.

Appendix B

Included within these supplementary materials are the results obtained from the synthetic modeling described in Chapter 2. This consists of a table (Table B1) and six figures (Figure B1 through Figure B6). Table B1 summarizes the results from the 96 free-inversions of all network configurations and source input models explored in the chapter. Figures B1 through B6, instead, shows the results obtained from the nonlinear inversion of all network configurations and source input models.

Table B1. Synthetic inversion results for 6-component unconstrained inversion

Subnet	# of stations	Input source	E_2	E_{2min} solutions			
				E-W position relative to input source [m]	N-S position relative to input source [m]	Depth position relative to input source [m] †	Eigenvalue ratios *
1	10	Isotropic (1, 1, 1)	0.261	0	0	60	1, 0.97, 0.95 1, 1, 1
		Crack (1, 1, 2)	0.192	0	0	0	1.04, 1, 2 1.14, 1.1, 2
		Crack (1, 3, 1)	0.266	0	0	0	0.93, 3, 0.77 0.84, 3, 0.76
		LVD (1, 1, 0)	0.221	0	0	80	1, 0.96, -0.09 1, 0.99, -0.16
		CLVD (2, -1, -1)	0.221	0	0	80	2, -0.21, -0.28 2, -1.1,- 0.91
		DC (1, 0, -1)	0.315	0	0	20	1, 0.14, -0.75 1, 0, -1
2	10	Isotropic (1, 1, 1)	0.202	0	0	0	1, 0.94, 0.87 1, 1, 1
		Crack (1, 1, 2)	0.208	0	0	0	0.98, 0.93, 2 1.14, 1.1, 2
		Crack (1, 3, 1)	0.221	0	0	0	0.91, 3, 0.69 0.84, 3, 0.76
		LVD (1, 1, 0)	0.238	0	0	0	1, 0.97, -0.04 1, 0.96, 0.03
		CLVD (2, -1, -1)	0.196	0	0	0	2, -0.5, -0.57 2, -1.16, -1.12
		DC (1, 0, -1)	0.218	0	0	0	1, 0.1, -0.7 1, 0, -1
3	10	Isotropic (1, 1, 1)	0.211	0	20 N	-60	1, 0.96, 0.9 1, 1, 1
		Crack (1, 1, 2)	0.204	0	0	60	1, 0.93, 2 1.14, 1.1, 2
		Crack (1, 3, 1)	0.205	0	0	0	1.15, 3, 0.88 1.2, 3, 1.05
		LVD (1, 1, 0)	0.225	0	0	-20	1, 0.94, 0.06 1, 0.96, 0.03
		CLVD (2, -1, -1)	0.225	0	0	80	2, -0.42, -0.53 2, -1.1,- 0.91
		DC (1, 0, -1)	0.228	0	0	0	1, 0.21, -0.55 1, 0, -1
4	10	Isotropic (1, 1, 1)	0.232	0	0	20	1, 0.96, 0.9 1, 1, 1
		Crack (1, 1, 2)	0.222	0	0	120	1.06, 1.02, 2 1.14, 1.1, 2
		Crack (1, 3, 1)	0.240	0	0	0	1.06, 3, 0.95 0.84, 3, 0.76
		LVD (1, 1, 0)	0.211	20 W	0	40	1, 0.96, 0.12 1, 0.96, 0.03
		CLVD (2, -1, -1)	0.216	0	0	60	2, -0.73, -0.87 2, -1.16, -1.12
		DC (1, 0, -1)	0.246	0	0	-20	1, 0.2, -0.6 1, 0, -1

Table B1 (continued). Synthetic inversion results for 6-component unconstrained inversion

				E_{2min} solutions			
Subnet	**# of stations**	**Input source**	E_2	E-W position relative to input source [m]	N-S position relative to input source [m]	Depth position relative to input source [m] †	Eigenvalue ratios *
5	16	Isotropic (1, 1, 1)	0.265	0	0	0	1, 0.99, 0.96 1, 1, 1
		Crack (1, 1, 2)	0.230	0	0	-20	1.07, 1.04, 2 1.14, 1.01, 2
		Crack (1, 3, 1)	0.284	0	0	0	0.81, 3, 0.72 0.84, 3, 0.76
		LVD (1, 1, 0)	0.279	0	0	0	1, 0.97, -0.03 1, 0.96, 0.03
		CLVD (2, -1, -1)	0.259	0	0	0	2, -0.38, -0.45 2, -1.16, -1.12
		DC (1, 0, -1)	0.319	0	0	-20	1, 0.17, -0.71 1, 0, -1
6	16	Isotropic (1, 1, 1)	0.265	0	0	0	1, 0.95, 0.92 1, 1, 1
		Crack (1, 1, 2)	0.242	0	0	-20	1.08, 1.01, 2 1.06, 0.91, 2
		Crack (1, 3, 1)	0.295	0	0	0	1,.18, 3, 0.86 1.2, 3, 1.05
		LVD (1, 1, 0)	0.280	0	0	0	1, 0.97, -0.04 1, 0.96, 0.03
		CLVD (2, -1, -1)	0.252	0	0	0	2, -0.22, -0.37 2, -1.10, -0.91
		DC (1, 0, -1)	0.273	0	0	-20	1, 0.25, -0.65 1, 0, -1
7	16	Isotropic (1, 1, 1)	0.266	0	0	0	1, 0.98, 0.96 1, 1, 1
		Crack (1, 1, 2)	0.243	0	0	-20	1.01, 0.98, 2 1.14, 1.01, 2
		Crack (1, 3, 1)	0.242	0	20 S	0	0.79, 3, 0.73 0.84, 3, 0.76
		LVD (1, 1, 0)	0.267	0	0	-20	1, 0.93, -0.08 1, 0.96, 0.03
		CLVD (2, -1, -1)	0.253	0	0	20	2, -0.41, -0.53 2, -1.16, -1.12
		DC (1, 0, -1)	0.266	0	0	0	1, 0.1, -0.79 1, 0, -1
8	4	Isotropic (1, 1, 1)	0.167	20 W	0	20	1, 0.97, 0.91 1, 1, 1
		Crack (1, 1, 2)	0.254	0	0	-20	1.12, 1.07, 2 1.14, 1.1, 2
		Crack (1, 3, 1)	0.140	0	0	20	0.88, 3, 0.66 0.84, 3, 0.76
		LVD (1, 1, 0)	0.157	20 E	20 N	-60	1, 0.87, -0.2 1, 0.99, -0.16
		CLVD (2, -1, -1)	0.150	40 W	20 S	40	2, -0.35, -0.42 2, -1.1,- 0.91
		DC (1, 0, -1)	0.214	0	20 N	-40	1, 0.22, -0.43 1, 0.09, -0.95

Table B1 (continued). Synthetic inversion results for 6-component unconstrained inversion

Subnet	# of stations	Input source	E_2	E_{2min} solutions			
				E-W position relative to input source [m]	N-S position relative to input source [m]	Depth position relative to input source [m] †	Eigenvalue ratios *
9	19	Isotropic (1, 1, 1)	0.268	0	0	0	1, 0.97, 0.96 1, 1, 1
		Crack (1, 1, 2)	0.237	0	0	-20	1.07, 1.01, 2 1.06, 0.9, 2
		Crack (1, 3, 1)	0.303	0	0	0	1.1, 3, 0.94 1.2, 3, 1.05
		LVD (1, 1, 0)	0.265	0	0	0	1, 0.93, -0.06 1, 0.96, 0.03
		CLVD (2, -1, -1)	0.263	0	0	0	2, -0.39, -0.45 2, -1.16, -1.12
		DC (1, 0, -1)	0.336	0	0	0	1, 0.15, -0.71 1, 0, -1
10	40	Isotropic (1, 1, 1)	0.277	0	0	0	1, 0.97, 0.96 1, 1, 1
		Crack (1, 1, 2)	0.252	0	0	-20	1.03, 1, 2 1.14, 1.1, 2
		Crack (1, 3, 1)	0.282	0	0	0	0.98, 3, 0.87 0.84, 3, 0.76
		LVD (1, 1, 0)	0.282	0	0	0	1, 0.97, -0.04 1, 0.96, 0.03
		CLVD (2, -1, -1)	0.265	0	0	0	2, -0.41, -0.46 2, -1.16, -1.12
		DC (1, 0, -1)	0.291	0	0	0	1, 0.14, -0.72 1, 0, -1
11	8	Isotropic (1, 1, 1)	0.245	0	0	0	1, 0.97, 0.93 1, 1, 1
		Crack (1, 1, 2)	0.221	0	0	-20	1.11, 1.08, 2 1.14, 1.1, 2
		Crack (1, 3, 1)	0.274	0	0	-20	0.96, 3, 0.77 0.84, 3, 0.76
		LVD (1, 1, 0)	0.235	0	0	-20	1, 0.95, -0.04 1, 0.96, 0.03
		CLVD (2, -1, -1)	0.233	0	0	0	2, -0.45, -0.61 2, -1.1,- 0.91
		DC (1, 0, -1)	0.349	0	0	0	1, 0.21, -0.66 1, 0, -1
12	8	Isotropic (1, 1, 1)	0.245	0	0	0	1, 0.97, 0.93 1, 1, 1
		Crack (1, 1, 2)	0.203	0	0	0	1.08, 1.03, 2 1.14, 1.1, 2
		Crack (1, 3, 1)	0.274	0	20 S	0	1.09, 3, 0.85 0.84, 3, 0.76
		LVD (1, 1, 0)	0.234	20 W	0	40	1, 0.93, -0.1 1, 0.96, 0.03
		CLVD (2, -1, -1)	0.215	0	0	0	2, -0.25, -0.34 2, -1.1,- 0.91
		DC (1, 0, -1)	0.377	0	0	20	1, 0.25, -0.6 1, 0, -1

Table B1 (continued). Synthetic inversion results for 6-component unconstrained inversion

Subnet	# of stations	Input source	E_2	E_{2min} solutions			
				E-W position relative to input source [m]	N-S position relative to input source [m]	Depth position relative to input source [m] †	Eigenvalue ratios *
13	3	Isotropic (1, 1, 1)	0.103	20 E	60 N	-80	1, 0.91, 0.82
							1, 1, 1
		Crack (1, 1, 2)	0.089	40 E	20 S	-80	0.93, 0.82, 2
							1.06, 0.9, 2
		Crack (1, 3, 1)	0.197	0	160 S	120	0.89, 3, 0.63
							0.84, 3, 0.76
		LVD (1, 1, 0)	0.089	40 W	100 N	-60	1, 0.89, -0.006
							1, 0.96, 0.03
		CLVD (2, -1, -1)	0.082	20 W	100 N	-60	2, -0.19, -0.64
							2, -1.1,- 0.91
		DC (1, 0, -1)	0.167	0	40 N	-60	1, 0.23, -0.38
							1, -0.09, -0.91
14	3	Isotropic (1, 1, 1)	0.093	40 W	40 S	0	1, 0.93, 0.86
							1, 0.92, 0.84
		Crack (1, 1, 2)	0.092	20 E	20 N	-20	0.95, 0.86, 2
							1.14, 1.1, 2
		Crack (1, 3, 1)	0.110	0	0	20	1.11, 3, 0.82
							1.2, 3, 1.05
		LVD (1, 1, 0)	0.095	20 E	0	-20	1, 0.9, 0.28
							1, 0.96, 0.03
		CLVD (2, -1, -1)	0.079	60 E	160 N	-60	2, -0.1, -0.85
							2, -1.39, -1.2
		DC (1, 0, -1)	0.084	20 E	0	-20	1, 0.22, -0.42
							1, 0.004, -0.86
15	3	Isotropic (1, 1, 1)	0.097	0	20 N	-20	1, 0.93, 0.87
							1, 0.92, 0.84
		Crack (1, 1, 2)	0.086	0	0	-40	1.16, 0.86, 2
							1.14, 1.1, 2
		Crack (1, 3, 1)	0.208	20 W	0	0	1.2, 3, 0.98
							1.2, 3, 1.05
		LVD (1, 1, 0)	0.081	40 W	0	-20	1, 0.9, 0.21
							1, 0.96, 0.03
		CLVD (2, -1, -1)	0.101	40 W	0	-20	2, -0.02, -1.24
							2, -1.1, -0.91
		DC (1, 0, -1)	0.174	20 E	0	-40	1, 0.1, -0.46
							1, -0.09, -0.91
16	3	Isotropic (1, 1, 1)	0/115	20 W	20 S	20	1, 0.92, 0.84
							1, 1, 1
		Crack (1, 1, 2)	0.091	0	0	80	1.16, 0.95, 2
							1.06, 0.9, 2
		Crack (1, 3, 1)	0.197	40 W	20 N	60	1.06, 3, 0.81
							1.2, 3, 1.05
		LVD (1, 1, 0)	0.102	40 W	0	20	1, 0.93, 0.52
							1, 0.96, 0.03
		CLVD (2, -1, -1)	0.094	20 W	20 S	60	2, -0.12, -0.35
							2, -1.1, -0.91
		DC (1, 0, -1)	0.124	20 W	20 S	40	1, 0.23, -0.49
							1, 0.004, -0.86

† Positive depth values indicate shallower depth with respect to the input location

* The first row associated with each source type shows the eigenvalue ratios of the free inversion solution at the input source location; the second row reports the eignvalue ratios of the constrained inversion solution at the input source location.

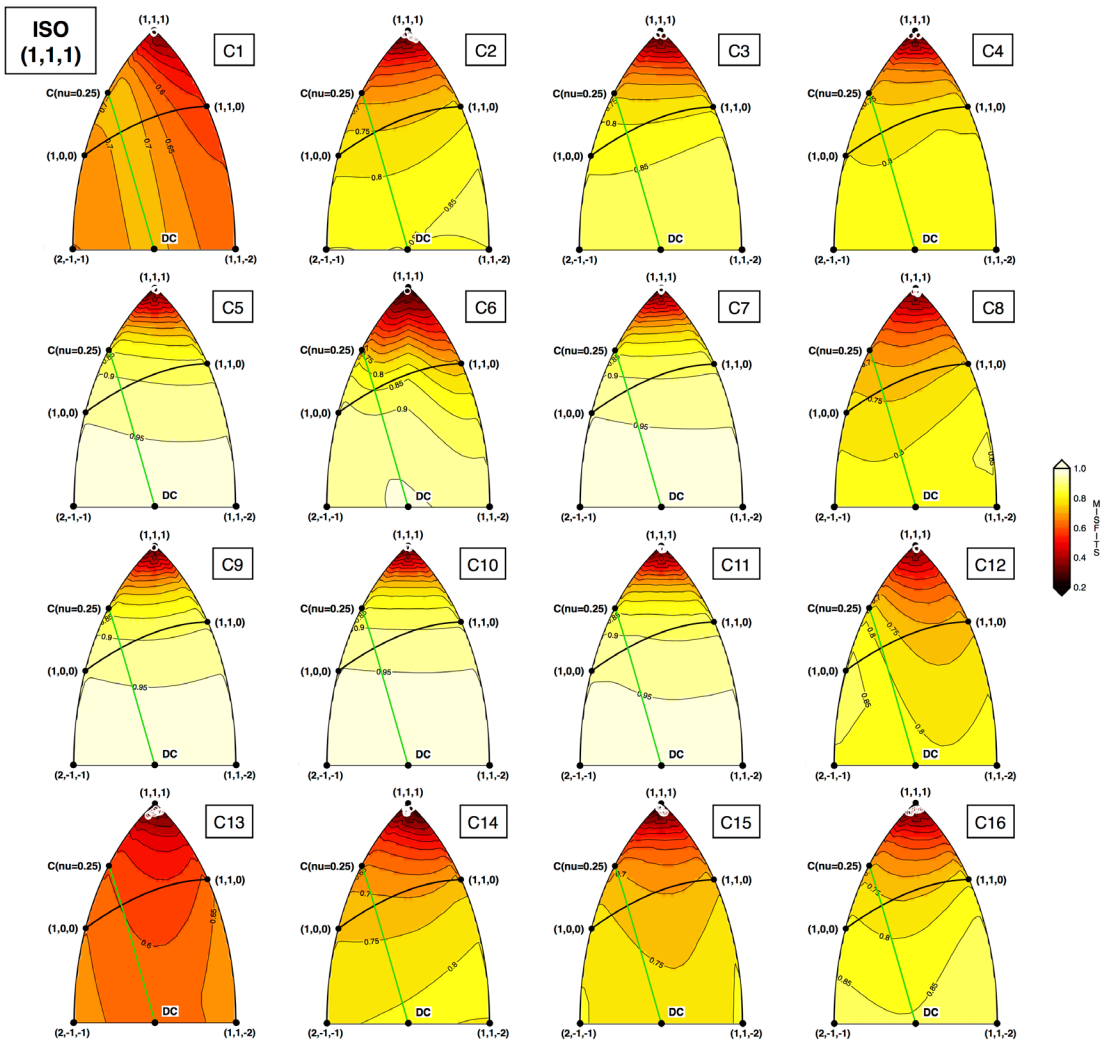

Figure B1. Error by fixed moment tensor solution for the isotropic input model (1, 1, 1), plotted together with the point-by-point mechanism type for the free inversion as white circles. Labels in the upper right corner of each lune indicate the station configuration number. We refer to Figure 2.1 in Chapter 2 for subnet geometries.

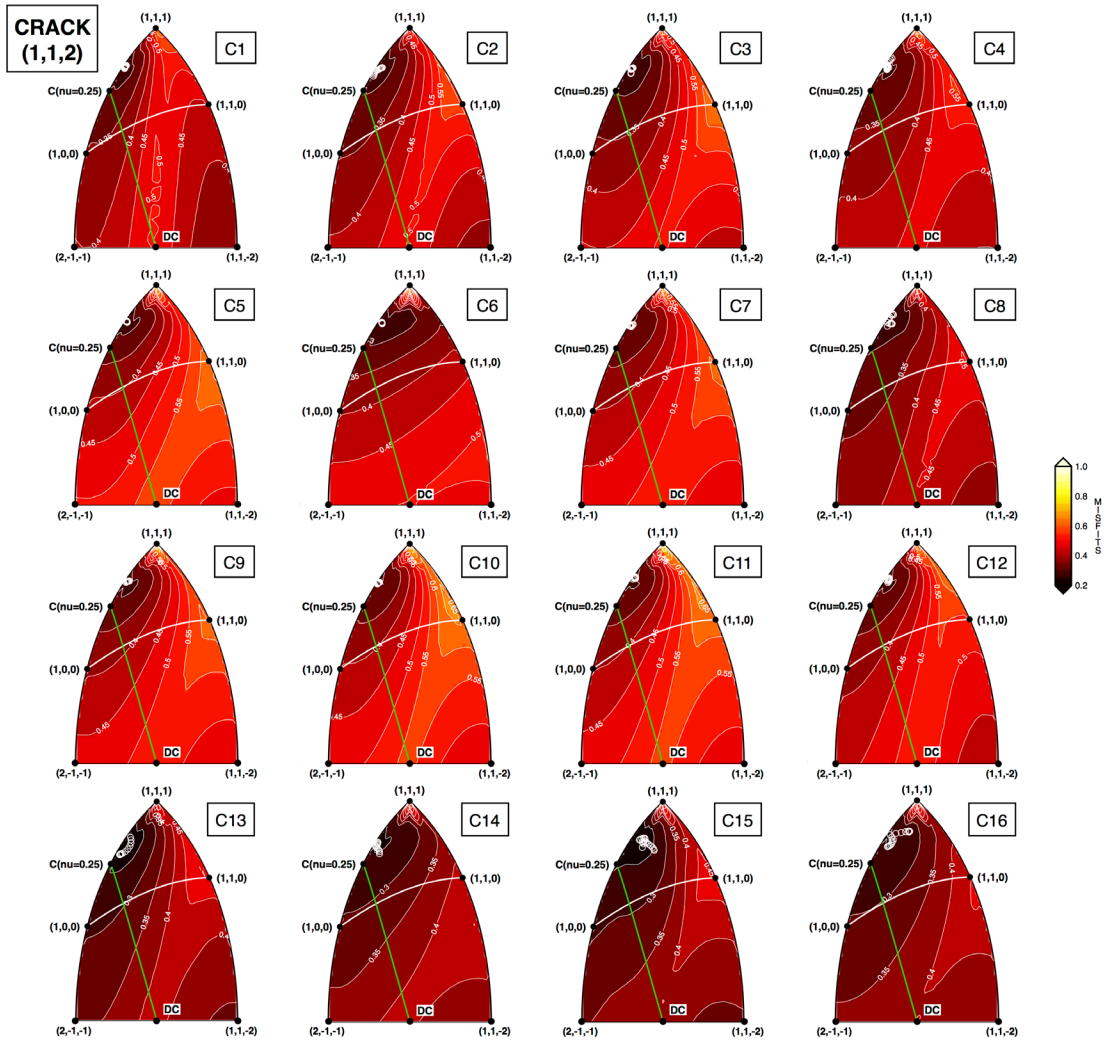

Figure B2. Error by fixed moment tensor solution for the horizontal crack input model (1, 1, 2), plotted together with the point-by-point mechanism type for the free inversion as white circles. Labels in the upper right corner of each lune indicate the station configuration number. We refer to Figure 2.1 in Chapter 2 for subnet geometries.

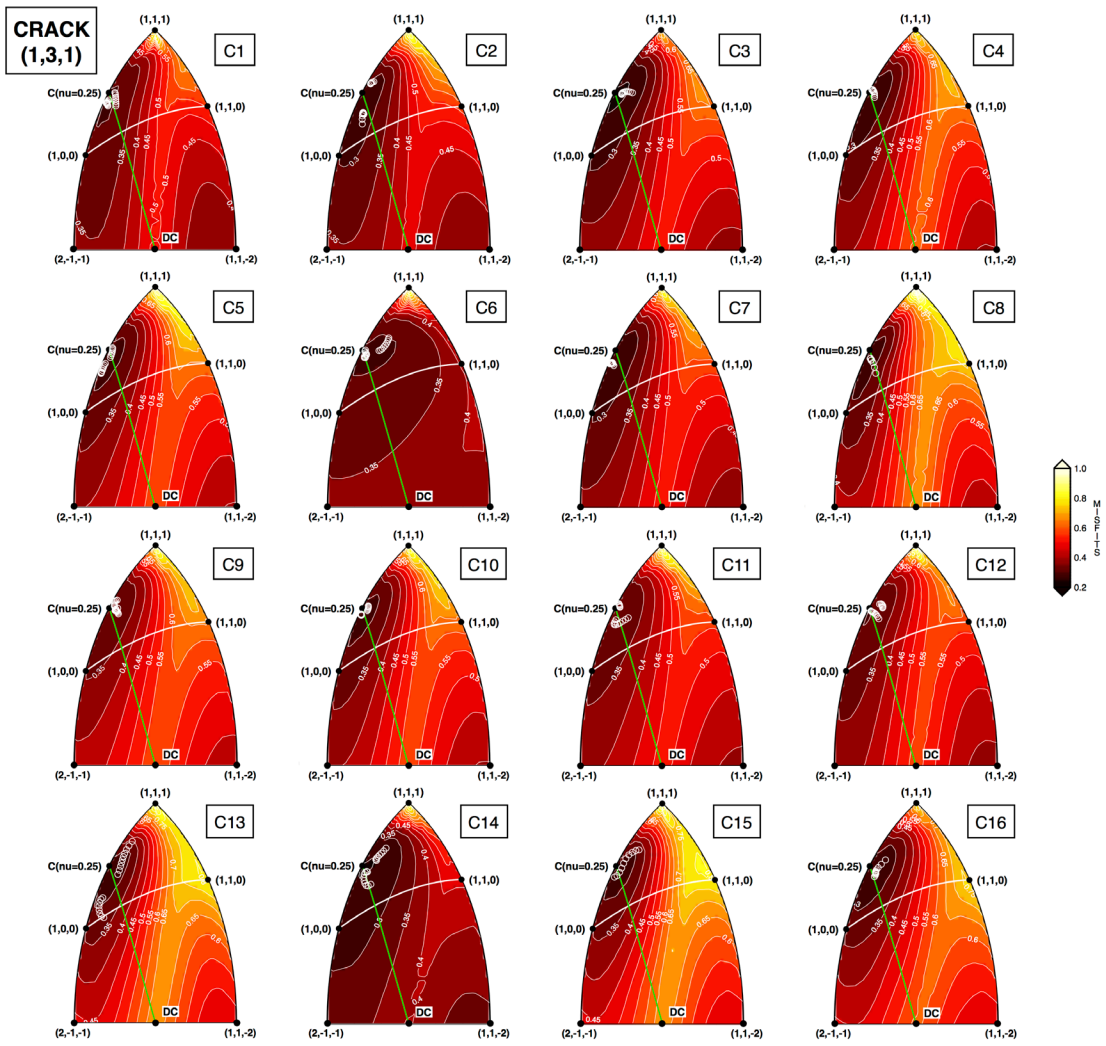

Figure B3. Error by fixed moment tensor solution for the vertical crack input model (1, 3, 1), plotted together with the point-by-point mechanism type for the free inversion as white circles. Labels in the upper right corner of each lune indicate the station configuration number. We refer to Figure 2.1 in Chapter 2 for subnet geometries.

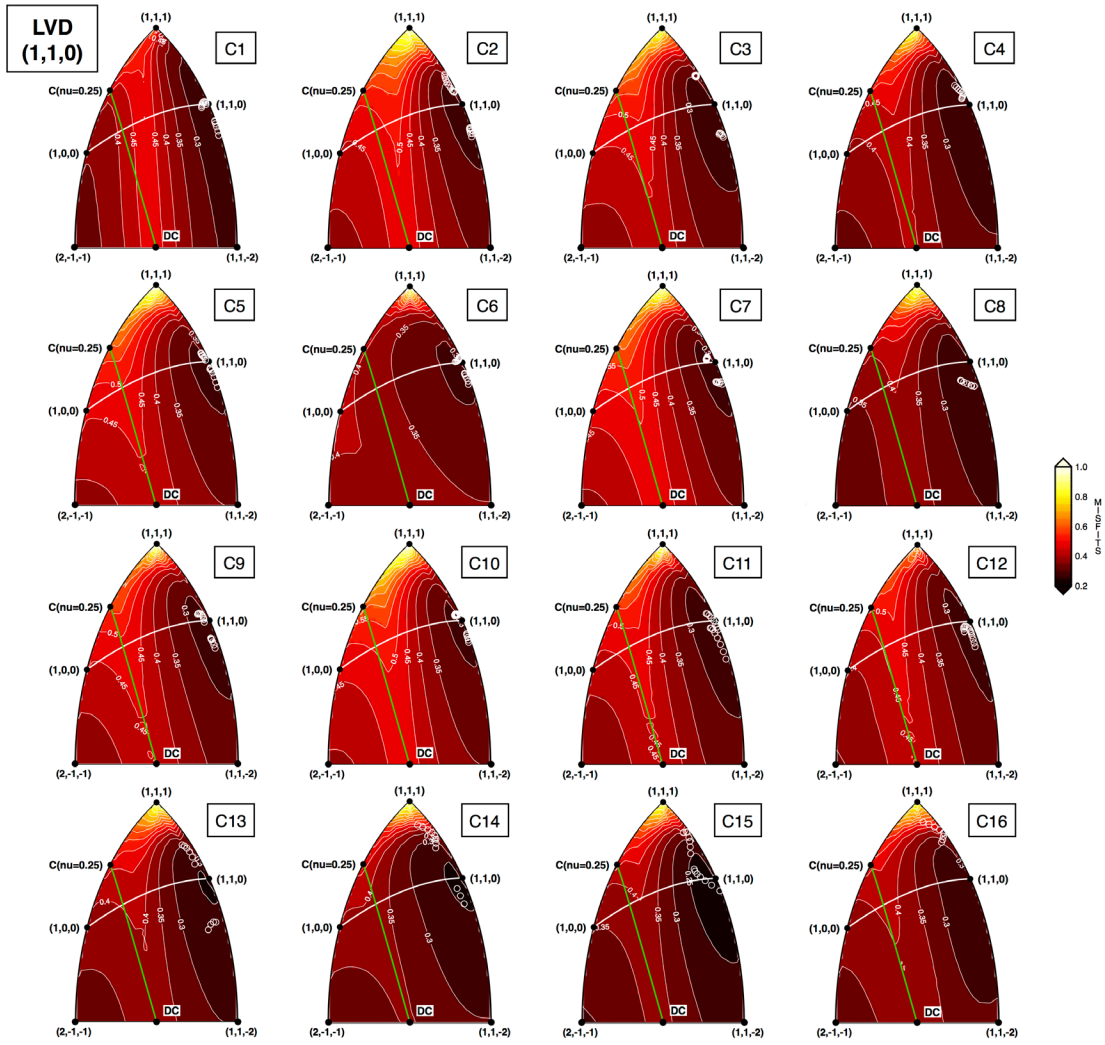

Figure B4. Error by fixed moment tensor solution for the LVD input model (1, 1, 0), plotted together with the point-by-point mechanism type for the free inversion as white circles. Labels in the upper right corner of each lune indicate the station configuration number. We refer to Figure 2.1 in Chapter 2 for subnet geometries.

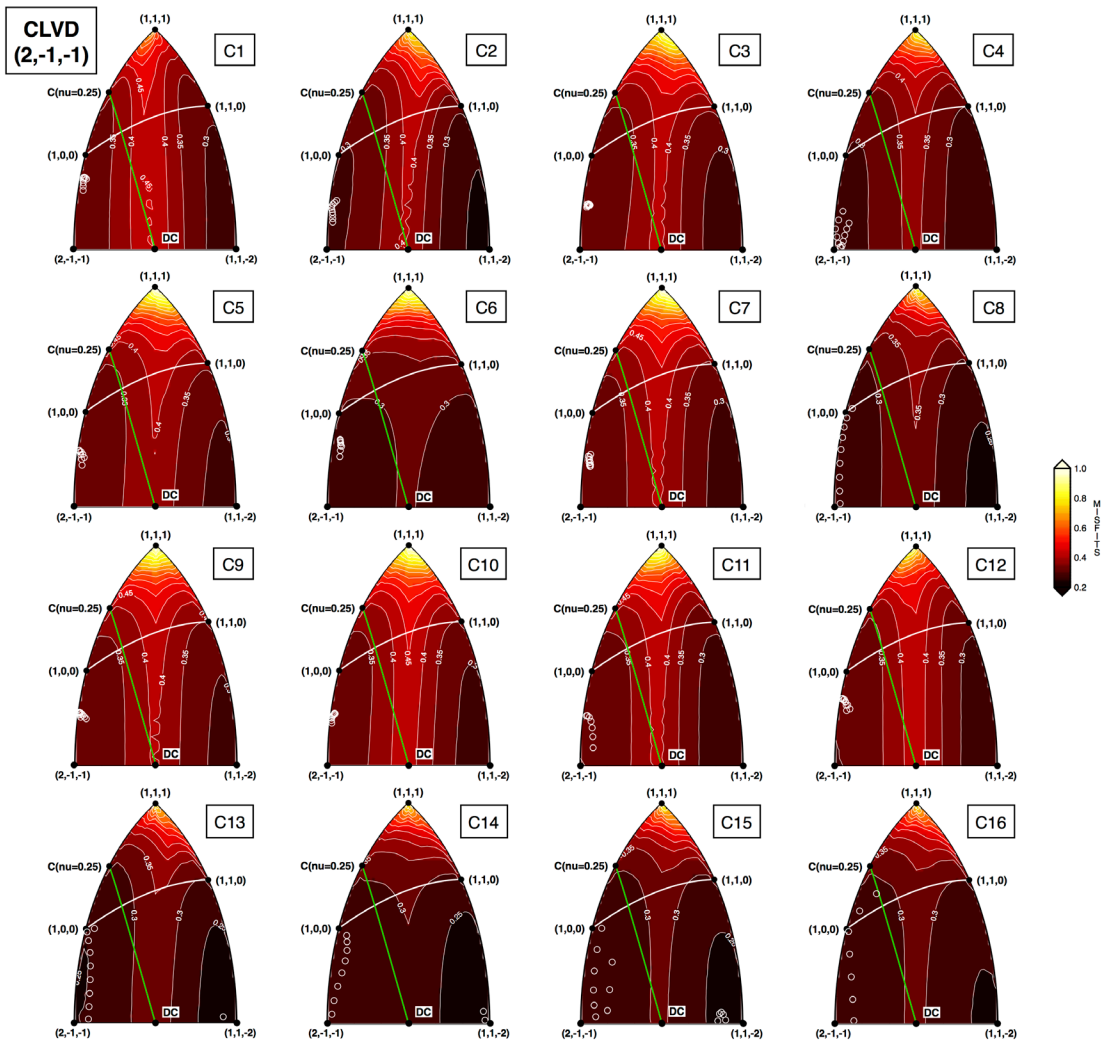

Figure B5. Error by fixed moment tensor solution for the CLVD input model (2, -1, -1), plotted together with the point-by-point mechanism type for the free inversion as white circles. Labels in the upper right corner of each lune indicate the station configuration number. We refer to Figure 2.1 in Chapter 2 for subnet geometries. Note that the white circles are plotted on the left side of the lune as a result of the projection of the negative points in the upper-half portion of the lune.

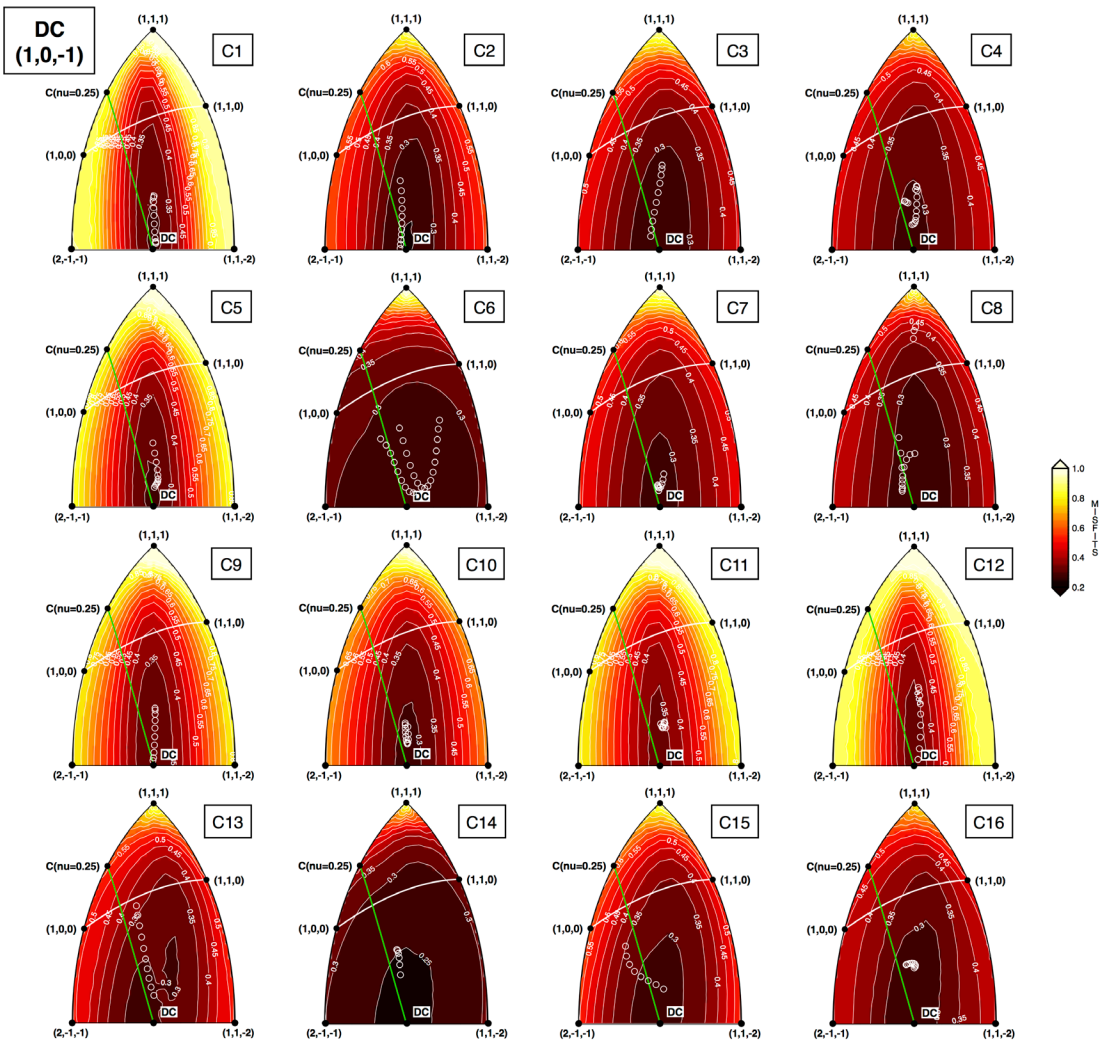

Figure B6. Error by fixed moment tensor solution for the DC input model (1, 0, -1), plotted together with the point-by-point mechanism type for the free inversion as white circles. Labels in the upper right corner of each lune indicate the station configuration number. We refer to Figure 2.1 in Chapter 2 for subnet geometries.

Appendix C

Michigan Tech

Federica Lanza <flanza@mtu.edu>

Copyright permission

2 messages

Federica Lanza <flanza@mtu.edu> Thu, Oct 27, 2016 at 10:30 AM
To: info@seismosoc.org

Hello,
I am completing my PhD dissertation at Michigan Technological University and I would like to request permission to re-use, for one of my dissertation chapters, the material published in the BSSA in my recent paper entitled;

Lanza, F., L.M. Kenyon, and G.P. Waite (2016). Near-surface velocity structure of Pacaya volcano, Guatemala, derived from small-aperture array analysis of seismic tremor, *Bull. Seism. Soc. Am.*, **106** (4), doi: 10.1785/0120150275.

Our graduate school requires official permissions to reuse copyrighted material.

Thank you,

Best regards,

Federica Lanza

--
Federica Lanza
Ph.D. Candidate
Geological and Mining Engineering and Sciences
Michigan Technological University
HOUGHTON, MI 49931 USA

Nan Broadbent <nbroadbent@seismosoc.org> Fri, Oct 28, 2016 at 11:16 AM
To: flanza@mtu.edu

Federica,

Yes, you have permission to re-use a chapter from your BSSA paper for the purpose you state in your note.

Thank you,

Nan Broadbent
[Quoted text hidden]
--
Nan Broadbent
Executive Director
Seismological Society of America
400 Evelyn Avenue, Suite 201
Albany, CA 94706
Desk: 510-559-1782

References

Akaike, H. (1974). A new look at the statistical model identification, *IEEE* Transactions on Automatic Control AC-9, 716–723.

Aki, K. (1957). Space and time spectra of stationary stochastic waves, with special reference tomicrotremors, *Bull. Earthq. Res. Inst*. Tokyo Univ. 25, 415–457.

Aki, K. (1959). Correlational study of near earthquake waves, *Bull. Earthq. Res. Inst*. Tokyo Univ. 37, 207–232.

Aki, K. (1965). A note on the use of microseisms in determining the shallow structures of the Earth's crust, *Geophysics* 30, 665–666.

Aki, K. and P.G. Richards (2002). Quantitative seismology, 2nd ed. Sausalito, CA: University Science Books.

Almendros, J., J.M. Ibáñez, G. Alguacil, and E. Del Pezzo (1999). Array analysis using circular-wave-front geometry: An application to locate the nearby seismo-volcanic source, *Geophys. J. Int.* 136, 159–170, doi:10.1046/j.1365-246X.1999.00699.x.

Alvizuri, C. and Tape, C., 2016. Full moment tensors for small events (Mw < 3) at Uturuncu volcano, Bolivia, *Geophys. J. Int.,* **206** (3): 1761-1783, doi:10.1093/gji/ggw247

Andres, R.J., and A.D. Kasgnoc (1998). A time-averaged inventory of subaerial volcanic sulfur emissions, *J. Geophys. Res.* 103, 25,251–25,261, doi: 10.1029/98JD02091.

Arciniega-Ceballos, A., P.B. Dawson, and B.A. Chouet (2012). Long period seismic source characterization at Popocatépetl volcano, Mexico, Geophys. Res. Lett., 39, L20307, doi:10.1029/2012GL053494.

Auger, E., L. D'Auria, M. Martini, B.A. Chouet, and P.B Dawson (2006). Real-time monitoring and massive inversion of source parameters of very long period seismic signals: An application to Stromboli Volcano, Italy, Geophys. Res. Lett*.,* 33, L04301, doi:10.1029/2005GL024703.

Bardintzeff, J.M., and C. Deniel (1992). Magmatic evolution of Pacaya and Cerra Chiquito volcanological complex, Guatemala, *Bull. Volcanol.* 54, 267–283, doi: 10.1007/BF00301482.

Beachley, M., E. Hooft, D. Toomey, and G.P. Waite (2012). Upper crustal structure of Newberry volcano from P-wave tomography and finite difference waveform modeling, *J. Geophys. Res.* 117, no. B10311, doi: 10.1029/2012JB009458.

Bean, C.J., I. Lokmer, and G.S. O'Brien (2008). Influence of near-surface volcanic structure on long-period seismic signals and on moment tensor inversions:

Simulated examples from Mount Etna, *J. Geophys. Res.*113 (B8), doi:10.1029/2007jb005468.

Bonnefoy-Claudet, S., F. Cotton, and P.Y. Bard (2006). The nature of noise wavefield and its applications for site effects studies: A literature review, *Earth Sci. Rev.* 79, 205–227, doi: 10.1016/j.earscirev.2006.07.004.

Brenguier, F., N.M. Shapiro, M. Campillo, A. Nercessian, and V. Ferrazzini (2007). 3-D surface wave tomography of the Piton de la Fournaise volcano using seismic noise correlations, *Geophys. Res. Lett.* 34, L02305, doi: 10.1029/2006GL028586.

Capon, J. (1969). High resolution frequency–wavenumber spectrum analysis, *Proc. IEEE* 57, 1408–1418.

Chávez-García, F.J., T. Domínguez, M. Rodríguez, and F. Pérez (2007). Site effects in a volcanic environment: A comparison between HVSR and array techniques at Colima, Mexico, *Bull. Seismol. Soc. Am.* 97, no. 2, 591–604, doi: 10.1785/0120060095.

Chouet, B.A. (1996). New methods and future trends in seismological volcano monitoring, in Monitoring and Mitigation of Volcano Hazards, R. Scarpa and R. I. Tilling (Editors), Spinger-Verlag, Berlin, Germany, 23–97.

Chouet, B.A., P.B. Dawson, and A. Arciniega-Ceballos (2005). Source mechanism of Vulcanian degassing at Popocatepetl Volcano, Mexico, determined from waveform inversions of very long period signal, *J. Geophys. Res.*, 110, B07301, doi:10.1029/2004JB003524.

Chouet, B.A., P.B. Dawson, T. Ohminato, M. Martini, G. Saccorotti, F. Giudicepietro, G. De Luca, G. Milana, and R Scarpa (2003). Source mechanisms of explosions at Stromboli Volcano, Italy, determined from moment-tensor inversion of very-long-period data, *J. Geophys. Res.,* 108, (B1), 2019, doi:10.1029/2002JB001919.

Chouet, B.A., P.B. Dawson, M.R. James, and S.J. Lane (2010). Seismic source mechanism of degassing bursts at Kilauea Volcano, Hawaii: results from waveform inversion in the 10–50 s band. *J. Geophys. Res.,* 115**,** B09311. doi:10.1029/2009JB006661.

Chouet, B.A., and R.S Matoza (2013). A multi-decadal view of seismic methods for detecting precursors of magma movement and eruption, *J. Volcanol. Geotherm. Res.,* 252*,* 108-175, doi:10.1016/j.jvolgeores.2012.11.013.

Chouet, B.A., G. De Luca, G. Milana, P. Dawson, M. Martini, and R. Scarpa (1998). Shallow velocity structure of Stromboli volcano, Italy, derived from small-aperture array measurements of Strombolian tremor*, Bull. Seismol. Soc. Am.* 88, 653–666.

Chouet, B.A., G. Saccorotti, M. Martini, P. Dawson, G. De Luca, G. Milana, and R. Scarpa (1997). Source and path effects in the wave fields of tremor and

explosions at Stromboli volcano, Italy, *J. Geophys. Res.* 102, 15,129–15,150, doi: 10.1029/97jb00953.

Claerbout, J.F., and F. Muir (1973). Robust modeling with erratic data, *Geophysics, 38*, 826-844.

Clarke D., J. Townend, M.K. Savage, and S. Bannister (2009). Seismicity in the Rotorua and Kawerau geothermal systems, Taupo Volcanic Zone, New Zealand, based on improved velocity models and cross-correlation measurements, *J. Volcanol. Geotherm. Res.,* 180(1) 50-66 doi:10.1016/j.jvolgeores.2008.11.004.

Conway, M.F., J.F. Diehl, and O. Matias (1992). Paleomagnetic constraints on eruptive patterns at the Pacaya composite volcano, Guatemala, *Bull. Volcanol.* 55, 25–32, doi: 10.1007/BF00301117.

Dalton, M.P., G.P. Waite, I.M. Watson, and P.A. Nadeau (2010). Multiparameter quantification of gas release during weak Strombolian eruptions at Pacaya volcano, Guatemala, *Geophys. Res. Lett.* 37, L09303, doi: 10.1029/2010GL042617.

Dawson, P., B.A, Chouet, and A. Pitt (2016). Tomographic image of a seismically active volcano: Mammoth Mountain, California, J. Geophys. Res. Solid Earth*,* 121, 114–133, doi:10.1002/2015JB012537.

Dawson, P.B., B.A. Chouet, and J. Power (2011). Determining the seismic source mechanism and location for an explosive eruption with limited observational data: Augustine Volcano, Alaska, Geophys. Res. Lett.*,* 38, L03302, doi:10.1029/2010GL045977.

De Barros, L., I. Lokmer, and C.J. Bean (2013). Origin of spurious single forces in the source mechanism of volcanic seismicity, *J. Volcanol. Geotherm. Res.,* 262, 1–6, doi:10.1016/j.jvolgeores.2013.06.006

De Luca, G., R. Scarpa, E. Del Pezzo, and M. Simini (1997). Shallow structure of Mt. Vesuvius volcano, Italy, from seismic array analysis, *Geophys. Res. Lett.* 24, no. 4, 481–484.

Eberthart-Phillips, D. (1990). Three-dimensional P and S velocity structure in the Coalinga region, California*, J. Geophys. Res.,* 95 (B10), 15,343-15,363. doi:10.1029/JB095iB10p15343.

Evans, J.R., D. Eberthart-Phillips, and C.H. Thurber (1994). User's manual for SIMULPS12 for imaging v_p and v_p/v_s: a derivative of the "Thurber" tomographic inversion SIMUL3 for local earthquakes and explosions. Open-file Rep. *U.S. Geol. Surv.,* Reston, VA. 94-431, 101.

Eyre, T.S., C.J. Bean, L. De Barros, F. Martini, I. Lokmer, M.M. Mora, J.F. Pacheco, and G.J. Soto (2015). A brittle failure model for long-period seismic events recorded at Turrialba Volcano, Costa Rica. *J. Geophys. Res. Solid Earth,* 120*,* 1452–1472. doi: 10.1002/2014JB011108.

Ferrazzini, V., K. Aki, and B.A. Chouet (1991). Characteristics of seismic waves composing Hawaiian volcanic tremor and gas piston events observed by a near-source array, *J. Geophys. Res.* 96, 6199–6209.

Goldstein, P., C.P.J. Poole, and L.L. Safko (2002). *Classical Mechanics*, 3rd ed., Pearson.

Goldstein, P., and R.J. Archuleta (1987). Array analysis of seismic signals, *J. Geophys. Res.* 14, 13–16.

Goldstein, P., and R.J. Archuleta (1991a). Deterministic frequency-wave number methods and direct measurements of rupture propagation during earthquakes using a dense array: Theory and methods, *J. Geophys. Res.* 96, 6173–6185.

Goldstein, P., and R.J. Archuleta (1991b). Deterministic frequency-wave number methods and direct measurements of rupture propagation during earthquakes using a dense array: Data analysis, *J. Geophys. Res.* 96, 6187–6198.

Goldstein, P., and B. Chouet (1994). Array measurements and modeling of sources of shallow volcanic tremor at Kilauea volcano, Hawaii, *J. Geophys. Res.* 99, 2637–2652.

Haslinger, F., E. Kissling (2001). Investigating effects of 3-D ray tracing methods in local earthquake tomography. *Phys. Earth Planet. Inter., 123*, 103-114.

Herrmann, R.B. (2013). Computer Programs in Seismology: An evolving tool for instruction and research, *Seismol. Res. Lett.* 84, 1081–1088, doi: 10.1785/0220110096.

Hotovec-Ellis, A. (2016). REDPy (Repeating Earthquake Detector in Python), https://github.com/ahotovec/REDPy, last accessed September 2016.

Hudson, J.A., R.G. Pearce, and R.M. Rogers (1989). Source type plot for inversion of the moment tensor, J. Geophys. Res., 94 (B1), 765–774, doi:10.1029/JB094iB01p00765.

James, M.R., S.J. Lane, L. Wilson, and S.B. Corder (2009). Degassing at low magma‐viscosity volcanoes: Quantifying the transition between passive bubble‐burst and Strombolian eruption, *J. Volcanol. Geotherm. Res.,* 180, 81–88, doi:10.1016/j.jvolgeores.2008.09.002.

Jolly, A. D., L. Chardot, J. Neuberg, N. Fournier, B.J. Scott, and S. Sherburn (2012). High impact mass drops from helicopter: A new active seismic source method applied in an active volcanic setting, *Geophys. Res. Lett.* 39, L12306, doi: 10.1029/2012GL051880.

Kirkpatrick, S.C., D. Gelatt, and M.P. Vecchi (1983). Optimization by simulating annealing, *Science*, *220*, 671-680.

Kiser, E., I. Palomeras, A. levander, C. Zelt, S. Harder, B. Schmandt, S. Hansen, K. Creager, and C. Ulberg (2016). Magma reservoirs from the upper crust to the Moho inferred from high-resolution Vp and Vs models beneath Mount St.

Helens, Washington State, USA. *Geology,* 44, 411-414, doi:10.1130/GE7591.1

Kissiling, E. (1988). Geotomograpy with local earthquake data, *Rev. Geophys.,* 26*,* 659-98

Kissling, E., W.L. Ellsworth, D. Eberhart-Phillips, and U. Kradolfer (1994). Initial reference models in local earthquake tomography, *J. Geophys. Res.,* 99, 19,635-19,646.

Lanza, F., L.M. Kenyon, and G.P. Waite (2016). Near-surface velocity structure of Pacaya volcano, Guatemala, derived from small-aperture array analysis of seismic tremor, *Bull. Seism. Soc. Am.,* 106 (4), doi: 10.1785/0120150275.

Lees, J. M. (2007). Seismic tomography of magmatic systems, *J. Volcanol. Geoth. Res.* 167, nos. 1/4, 37–56, doi: 10.1016/j.jvolgeores.2007.06.008.

Lomax, A., and R. Snieder (1994). Finding sets of acceptable solutions with a genetic algorithm with application to surface wave group dispersion in Europe, *Geophys. Res. Lett., 21* (24), 2617-2620.

Ludwig,W. J., J.E. Nafe, and C.L. Drake (1970). Seismic refraction, in The Sea, A. E. Maxwell (Editor), Vol. 4, Wiley-Interscience, New York, New York, 53–84.

Matias Gomez, R.O. (2010). Volcanological map of Pacaya volcano, Guatemala, M.S. Thesis, Michigan Technological University, Houghton, Michigan, 57 pp.

Matoza, R.S., B.A. Chouet, P.B. Dawson, P.M. Shearer, M.M. Haney, G.P. Waite, S.C. Moran, and T.D. Mikesell (2015). Source mechanism of small long-period events at Mount St. Helens in July 2005 using template matching, phase-weighted stacking, and full-waveform inversion, *J. Geophys. Res.,* 120 (9), 6351-6364, doi:10.1002/2015jb012279.

Menke, W. (1989). Geophysical Data Analysis: Discrete Inverse Theory, Academic Press, New York, New York.

Métaxian, J.P., P. Lesage, and J. Dorel (1997). Permanent tremor of Masaya volcano, Nicaragua: Wave field analysis and source location, *J. Geophys. Res.* 102, 22,529–22,545, doi: 10.1029/97JB01141.

Metropolis, N., M.N. Rosenbluth, A.W. Rosenbluth, A.H. Teller, and E. Teller (1953), Equation of state calculations by fast computing machine, *J. Chem. Phys.,* 21*,* 1087-1092.

Mora, M.M., P. Lesage, B. Valette, G.E. Alvarado, C. Leandro, J.P. Métaxian, and J. Dorel (2006). Shallow velocity structure and seismic site effects at Arenal volcano, Costa Rica*, J. Volcanol. Geoth. Res.* 152, 121–139, doi: 10.1016/j.jvolgeores.2005.09.013.

Mosegaard, K., and A. Tarantola (1995), Monte Carlo sampling of solutions to inverse problems, *J. Geophys. Res.,* 100 (B7), 12,431-12,447.

Nardone, L., and R. Maresca (2011). Shallow velocity structure and site effects at Mt.

Vesuvius, Italy, from HVSR and array measurements of ambient vibrations, *Bull. Seismol. Soc. Am.* 101, no. 4, 1465–1477, doi: 10.1785/0120100165.

Neidell, N., and T. Taner (1971). Semblance and other coherency measures for multichannel data, *Geophysics* 36, 482–497.

Neuberg, J., and T. Pointer (2000). Effects of volcano topography on seismic broadband waveforms, *Geophys. J. Int.,* 143*,* 239–248, doi:10.1046/j.1365-246x.2000.00251.x.

O'Brien, G.S., and C.J. Bean (2009). Volcano topography, structure and intrinsic attenuation: Their relative influences on a simulated 3D visco-elastic wavefield, *J. Volcanol. Geotherm. Res.,* 183(1-2), 122-136, doi:10.1016/j.jvolgeores.2009.03.004.

Ohminato, T., and B.A. Chouet (1997). A free-surface boundary condition for including 3D topography in the finite-difference method, *Bull. Seism. Soc. Am.,* 87(2), 494-515.

Ohminato, T., B.A. Chouet, P.B. Dawson, and S. Kedar (1998). Waveform inversion of very long period impulsive signals associated with magmatic injection beneath Kilauea Volcano, *J. Geophys. Res.,* 103(B10), 23,839-823,862, doi:10.1029/98JB01122.

Okada, H. (2003). The Microtremor Survey Method, Geophysical Monograph Series, No. 12, *Soc. of Explor. Geophys.,* Tulsa, Oklahoma, 135 pp.

Paulatto, M., T.A. Minshull, B. Baptie, S. Dean, J.O.S. Hammond, T. Henstock, C.L. Kenedi, E.J. Kiddle, P. Malin, C. Pierce, et al. (2010). Upper crustal structure of an active volcano from refraction/reflection tomography, Montserrat, Lesser Antilles, *Geophys. J. Int*. 180, no. 2, 685–696, doi: 10.1111/j.1365-246X.2009.04445.x.

Rawlinson N., S. Pozgay, and S. Fishwick (2010), Seismic tomography: A window into deep Earth, *Phys. Earth Planet. Int.*, 178 (3-4), 101-135, doi:10.1016/j.pepi.2009.10.002.

Richardson, J.P., and G.P. Waite (2013). Waveform inversion of shallow repetitive long period events at Villarrica Volcano, Chile, *J. Geophys. Res.,* 118, 4922–4936, doi:10.1002/jgrb.50354.

Rodriguez, L.A., I.M. Watson, W.I. Rose, Y.K. Branan, G.J.S. Bluth, G. Chigna, O. Matías, D. Escobar, S.A. Carn, and T.P. Fischer (2004). SO2 emissions to the atmosphere from active volcanoes in Guatemala and El Salvador, 1999-2002, *J. Volcanol. Geoth. Res.* 138, 325–344, doi: 10.1016/j.jvolgeores.2004.07.008.

Rose, W.I., J.L. Palma, R.E. Wolf, and R.O. Matías Gomez (2013). A 50 yr eruption of a basaltic composite cone: Pacaya, Guatemala, *Spec. Pap. Geol. Soc. Am.* 498, 1–21, doi: 10.1130/2013.2498(01).

Rost, S., and C. Thomas (2002). Array seismology: Methods and applications, *Rev. Geophys.* 40, no. 3, 1–27, doi: 10.1029/2000RG000100.

Saccorotti, G., J. Almendros, E. Carmona, J. Ibanez, and E. Del Pezzo (2001). Slowness anomalies from two dense seismic arrays at Deception Island volcano, Antarctica, *Bull. Seismol. Soc. Am.* 91, 561–571, doi: 10.1785/0120000073.

Saccorotti, G., B.A. Chouet, and P.B. Dawson (2003). Shallow-velocity models at the Kilauea volcano, Hawaii, determined from array analyses of tremor wavefields, *Geophys. J. Int.* 152, 633–648, doi: 10.1046/j.1365-246X.2003.01867.x.

Saccorotti, G., R. Maresca, and E. Del Pezzo (2001). Array analyses of seismic noise at Mt. Vesuvius volcano, Italy, *J. Volcanol. Geoth. Res.* 110, nos. 1/2, 79–100, doi: 10.1016/S0377-0273(01)00204-9.

Sambridge, M., K. Mosegaard (2002), Monte Carlo methods in geophysical inverse problems, *Rev. Geophys.,* 40 (3), 1009, doi:10.1029/2000RG000089.

Schimmel, M., and H. Paulssen (1997). Noise reduction and detection of weak, coherent signals through phase-weighted stacks, *Geophys. J. Int.,* 130*,* 497-505, doi:10.1111/j.1365-246X.1997.tb05664.x.

Schaefer, L.N., T. Oommen, C. Corazzato, A. Tibaldi, R. Escobar-Wolf, and W.I. Rose (2013). An integrated field-numerical approach to assess slope stability hazards at volcanoes: The example of Pacaya, Guatemala, *Bull. Volcanol.* 75, 720, doi: 10.1007/s00445-013-0720-7.

Shapiro, N.M., M. Campillo, L. Stehly, and M.H. Ritzwoller (2005). High resolution surface wave tomography from ambient seismic noise, *Science* 307, 1615–1618, doi: 10.1126/science.1108339.

Shapiro, N.M. and M.H. Ritzwoller (2002), Monte-Carlo inversion for a global shear-velocity model of the crust and upper mantle. *Geophys. J. Int.,* 151, 88–105. doi:10.1046/j.1365-246X.2002.01742.x.

Shearer, P.M. (1994). Global seismic event detection using a matched filter on longperiod seismograms, *J. Geophys Res.,* 99(B7), 13713-13725.

Siebert, L., and T. Simkin (2002). Volcanoes of the world: An illustrated catalog of Holocene volcanoes and their eruptions, Global Volcanism Program Digital Inf. Ser. GVP-3, Smithsonian Institute, Washington, D.C., http://www.volcano.si.edu/world/ (last accessed September 2015).

Snieder, R., and E. Larose (2013). Extracting Earth's elastic wave response from noise measurements, *Annu. Rev. Earth Planet. Sci.* 41, 183–206, doi: 10.1146/annurev-earth-050212-123936.

Tape, W., and C. Tape (2012). A geometric setting for moment tensors, *Geophys. J. Int.,* 190, 476-498.

Thurber, C.H. (1983), Earthquake locations and three-dimensional crustal structure in the Coyote lake area, central California, *J. Geophys. Res.,* 88(B10), 8226-8236.

Thurber, C.H. (1986), Analysis methods for kinematic data from local erathquakes, *Rev. Geophys.,* 24, 793-805.

Thurber, C.H. (1993), Local earthquake tomography: velocities and Vp/Vs theory, in: Seismic Tomography: Theory and practice. Edited by H. M. Iyer and K. Hirahara, Chapman & Hall, London.

Thurber, C.H., X. Zeng, A.M. Thomas, and P. Audet (2014). Phase-Weighted Stacking Applied to Low-Frequency Earthquakes, *Bull. Seism. Soc. Am.*, 104(5), 2567-2572. doi: 10.1785/0120140077.

Tsai, V.C., and M.P. Moschetti (2010). An explicit relationship between time domain noise correlation and spatial autocorrelation (SPAC) results, *Geophys. J. Int*. 182, 454–460, doi: 10.1111/j.1365-246X.2010.04633.x.

Verdon J.P. (2011), Seis_pick, File Exchange MathWorks

Wagner, G.S., and T.J. Owens (1996). Signal detection using multi-channel seismic data, *Bull. Seismol. Soc. Am.* 86, 221–231.

Waite, G.P., B.A. Chouet, and P.B. Dawson (2008). Eruption dynamics at Mount St. Helens imaged from broadband seismic waveforms: Interaction of the shallow magmatic and hydrothermal systems, *J. Geophys. Res.,* 113(B2), B02305, doi:10.1029/2007jb005259.

Waite G.P., and S.C. Moran (2009), VP Structure of Mount St. Helens, Washington, USA, imaged with local earthquake tomography, *J. Volcanol. Geotherm. Res.,* 182 (1-2)*,* 113-122 doi:10.1016/j.jvolgeores.2009.02.009.

Waite, G.P., and F. Lanza (2016). Nonlinear inversion of tilt-affected very-long-period records 1 of explosive eruptions at Fuego volcano, *J. Geophys. Res.,* 121, doi:10.002/2016JB013287

Waite, G.P. R.B. Smith, and R.M. Allen (2006). Vp and Vs structure of the Yellowstone hot spot from teleseismic tomography: Evidence for an upper mantle plume, *J. Geophys. Res.* 111, B04303, doi:10.1029/2005JB003867

Wunderman, R.L., and W.I. Rose (1984). Amatitlán, an actively resurging caldera 10 km south of Guatemala City, *J. Geophys. Res.* 89, 8525–8539.

Xu, Z., S.Y. Schwartz, and T. Lay (1996). Seismic wave-field observations at a dense, small-aperture array located on a landslide in the Santa Cruz mountains, California*, Bull. Seismol. Soc. Am.* 86, 655–669.

Zucca, J.J., and J.R. Evans (1992). Active high-resolution compressional wave attenuation tomography at Newberry volcano, central Cascade Range, *J. Geophys. Res.* 97, no. B7, 11,047–11,055, doi: 10.1029/92JB00492.